論文 / 著書情報
Article / Book Information

題目(和文)	単分子接合における化学反応
Title(English)	Chemical reaction on single molecular junctions
著者(和文)	李 渝
Author(English)	Yu Li
出典(和文)	学位:博士(理学), 学位授与機関:東京工業大学, 報告番号:甲第10612号, 授与年月日:2017年9月20日, 学位の種別:課程博士, 審査員:木口 学,西野 智昭,河内 宣之,沖本 洋一,北島 昌史
Citation(English)	Degree:Doctor (Science), Conferring organization: Tokyo Institute of Technology, Report number:甲第10612号, Conferred date:2017/9/20, Degree Type:Course doctor, Examiner:,,,,
学位種別(和文)	博士論文
Type(English)	Doctoral Thesis

Thesis

Chemical reaction on single molecular junctions

Submitted to the Tokyo Institute of Technology

for the degree of Doctor of Science

=

Yu Li

Department of Chemistry
Graduate School of Science and Engineering
Tokyo Institute of Technology

June 2017

Contents

Chapter 1

General introduction

1.1 Molecular electronics

Microelectronics that relied on silicon, gallium arsenide and gallium nitride materials contribute to the economic development, consolidate national defense even in improvement of the daily life. There is still room for optimization in silicon-based microelectronics in principle. However, in the end of 1959, that so-called famous speech named ‘There’s plenty of room at the bottom’ gave by Richard P. Feynman proposed a brand new idea. Feynman supposed that a circuits in a seven atoms scale should be diverse from the macroscopic surface, from then, this idea became fascinating and marvelous to scientists [1]. With well understanding of the Moore’s law, researchers started to request of ultra-small scale devices [2]. Instead of the traditional top-down method, they turned to develop the bottom-up method to minimum the electronic devices from atomic scale. 10 more years past after the Feynman speech, in 1974, Aviram and Ratner made this small circuit conception more clearly, in the first time predicted the single molecular rectifier based on the theoretical calculation. Refered to classical p-n junctions in macroscopic solid-state rectifiers, they brought out a metal/molecule/metal structure with a rectifier molecule [3]. Latter, Cater’s vision of the molecular electronic devices called on scientists to reclaim this new field, endow this topic flourish in the early of the 1980’s [4].

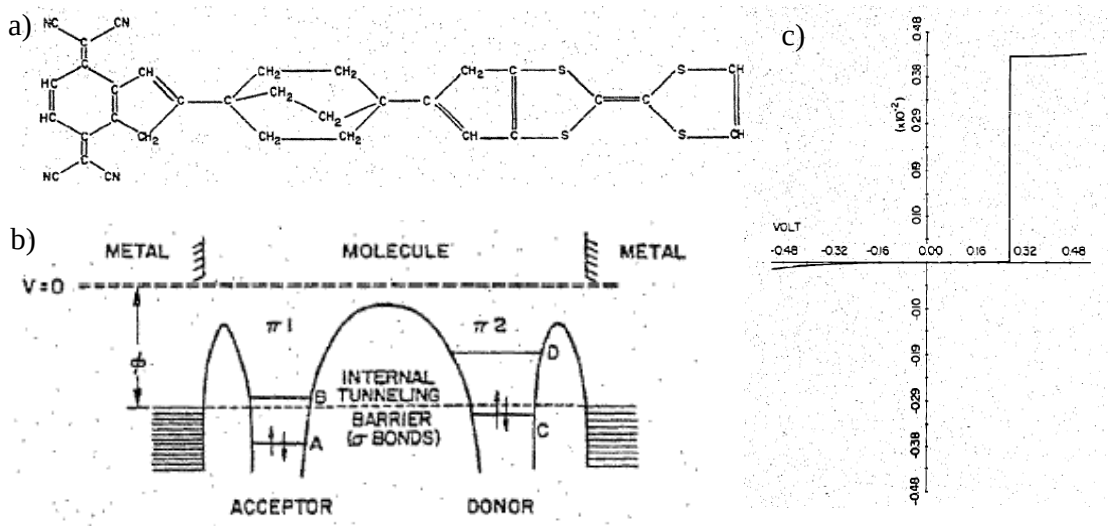

Figure 1.1.1 a) An example of a rectifier molecule b) Metal/molecule/metal structure designed by Aviram and Ratner 1974 c) Current-bias voltage characteristics of a molecular rectifier including direct electrode to electrode tunneling. Current in A/cm^2, bias voltage in volt [3].

With the tremendous development of nanoscience and nanotechnology for decades of years, molecular electronics in low dimension to date has been believed as the next generation electronic circuitry, which would be able to take charge of the restriction of the silicon-based electronics. The traditional microelectronics exploit the particle property of the electron wave-particle duality, the signal processing is according to the number of the electrons. With the minimization of the circuit integration, the problems like power consumption, electron transport speed or electric leakage could be foresaw. In contrast, the molecular devices work rely on the quantum properties not the quantity of the electrons. Thus, according to control the electron wave phase, the limited working electrons in molecular devices could avoid the electric leakage and power consumption caused by the massive of electrons transport in the circuits. Therefore, the expected function of molecular devices could be implemented with a 1000-10000 times better performance in response speed and power consumption compared to the traditional circuit [分子器件的研究进展].

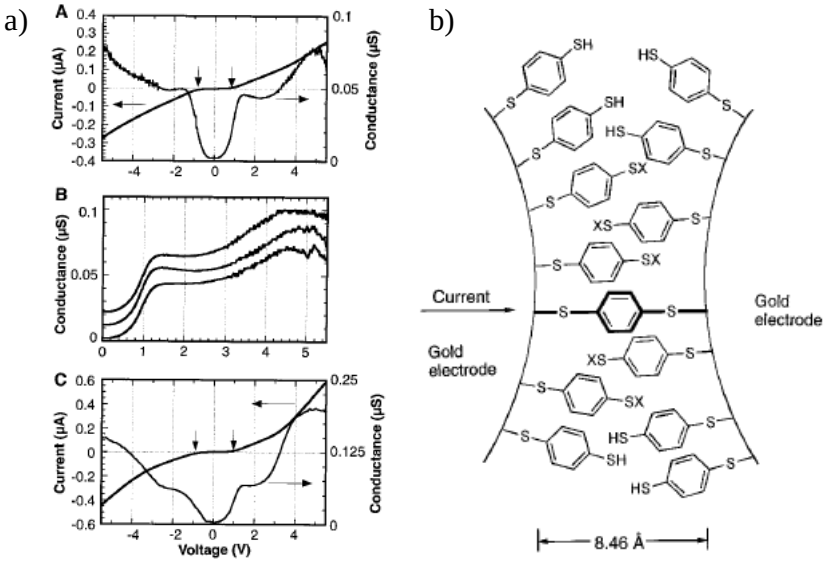

Figure 1.1.2 a) Typical *I-V* characteristics of the Au-1,4 benzenedithiol-Au system; b) A schematic of a benzene-1,4- dithiolate self-assembled monolayer (SAM) between proximal gold electrodes formed in an MCBJ [5].

Without the nano technology progress, the dream of molecular devices could not come true. From the 80s last century, the evolution of the Scanning Tunneling Microscope (STM) technique and relevant techniques executed the molecular electronics experimentally. After the first composition of the molecular electronics has been proposed 25 years later, Reed *et al*. and his colleague completed the Au-1,4 benzenedithiol (BDT)-Au single molecular junction (SMJ) with Mechanically Controllable Break Junction (MCBJ) technique (Fig.1.1.2). With the investigation of the *I-V* characteristics, their results suggest the conductance behavior of the investigated system has been confirmed to be ~ 22 megohm at

about 0.7 V [5].

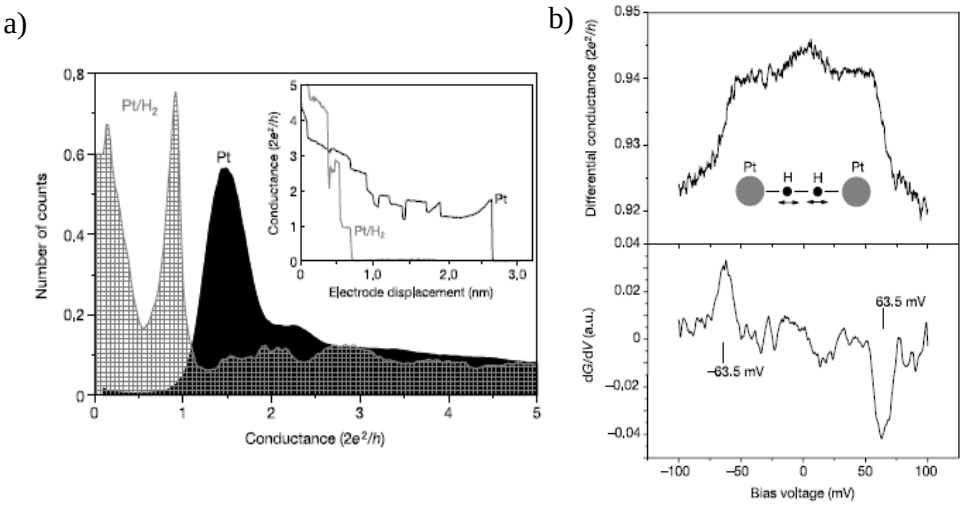

Figure 1.1.3 a) Typical conductance behavior Pt, and for Pt in a H_2 atmosphere, b) Differential conductance (top) and its derivative (bottom) for a Pt/H_2 contact taken at a conductance plateau close to 1 G_0 (conductance in quantum unit, $G_0 = 2e^2/h$) [6].

As long as the new techniques brought out continuously from the early of 21th century for the requirement of nano science nature. The formal concern in molecular devices increasing exponentially. In 2002, J. M. van Ruitenbeek group fabricated Pt-H_2-Pt single molecular junction also with MCBJ technique (Figure 1.1.3) [6]. They studied the conductance behavior and the vibration mode for the individual molecules using Point Contact Spectroscopy (PCS) in 4K, the Pt-H_2-Pt single molecular junction resulted in a nearly perfect transmission.

Just one year later, Xu *et al*. reported an Au- 4,4' bipyridine -Au single molecular junction fabricated by Scanning Tunneling Microscopy (STM) [7]. With the 4, 4' bipyridine molecules bridged between the two electrodes, the conductance behavior in quantization, were obtained in 1, 2, 3 times of 0.01 G_0 corresponding to the 1, 2, 3 bridges in the junction, stem from both the experimental and theoretical results.

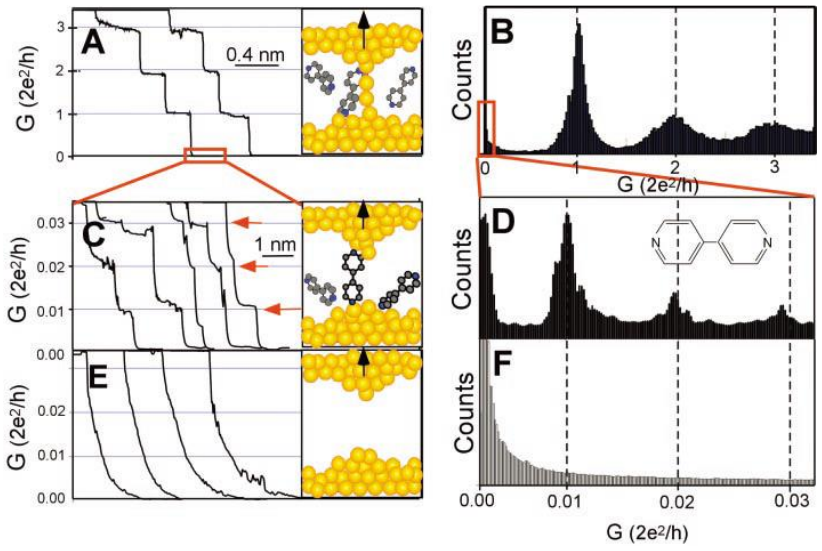

Figure 1.1.4 Typical conductance traces and histograms for the Au- 4,4'bipyridine-Au single molecular junction a,b) gold atomic contact; c,d) Au- 4,4'bipyridine-Au junction; e,f) when the contact break down [7].

1.2 Importance status and progress of molecular devices

Researchers of the molecular electronics are greedy, their ambition in this field range from the single wire, switch, rectifier, logic circuitry even the completed computer. In the late of 1980's, with the booming development of the state-of-the-art microprocessors use scanning probe microscopy, Nano-imprint lithography, Electron Beam (EB) processing technology, Near-field optical technique, Fluorescent probe technique, optical tweezers facilitates the substantive progress of the molecular electronics. With half century endeavor, to date, versatility of molecular electronics have been attested to be underlying to construct the logic circuit in low dimension level.

1.2.1 Molecular rectifier (diode)

As the first prediction of molecular devices in the 1970s', the concept of molecular rectifier comes from the solid state p-n junction in macroscopic view. One of the essential properties for the rectifier is unilateral conduction that has useful application in modern electronics. In specific, when the 'p' end containing excess holes applied with positive bias while the 'n' side containing excess electrons applied with negative bias, the rectifier works, electron go through the circuit. Whereas 'p' end with negative bias, 'n' end with positive bias, the resistance of the device increases leading to a limited current. In another word, the electron is able to transport only one direction with constant bias voltage. Thus, with the similar structure, the single molecule would display rectification. Say concretely, the molecule with electron rich end (n-type) and electron poor end (p-type) would show rectification.

Aviram and Ratner conceived the first molecular rectifier with Donor-σ-Accepter (D-σ-A) structure, where D is a strong electron donor (easily oxidized), A is a strong electron acceptor (easily reduced), and σ is a covalent bridge between them. Besides, they calculated the rectification and electron transport mechanics of this molecule [3]. With the AR mode was hypothesized, the massive scientists made contribute to development of the molecular rectifier. Unfortunately, the perfection of the AR proposal, which contains strong D part and strong A part caused the challenges for the synthesis of ideal the D-σ-A type molecule in reality. Even worse situation for the further experimental evidence. Additionally, in the latter study, Geddes *et al*. suggested that the Schottky barrier might be responsible for the rectification rather than the asymmetric conduction came from the molecule as in the AR proposal [8].

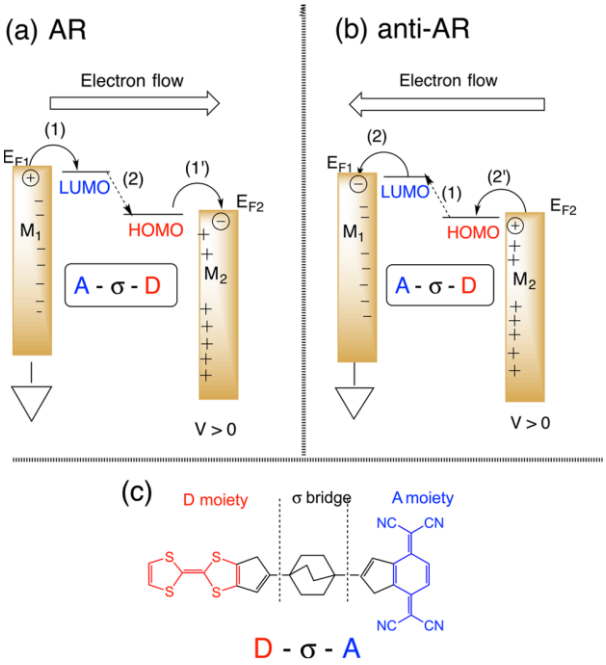

Figure 1.2.1 The AR mode showing a proposed D-σ-A molecule [9].

Mercifully, the researchers did not give up. Metzger group was concern for the D-π-A type $C_{16}H_{33}Q$-3CNQ Langmuir- Blodgett mono-, multilayer films [9]. Liu and his co-worker developed a multiwalled carbon nanotubes (MWCNTs) beaded with spherical crystalline Co_3O_4 nanoparticles system and obtain high certification around 70 (± 2.5 V) [10]. Hou group constructed a single $C_{59}N$ molecule to be a new type molecular rectifier [11].

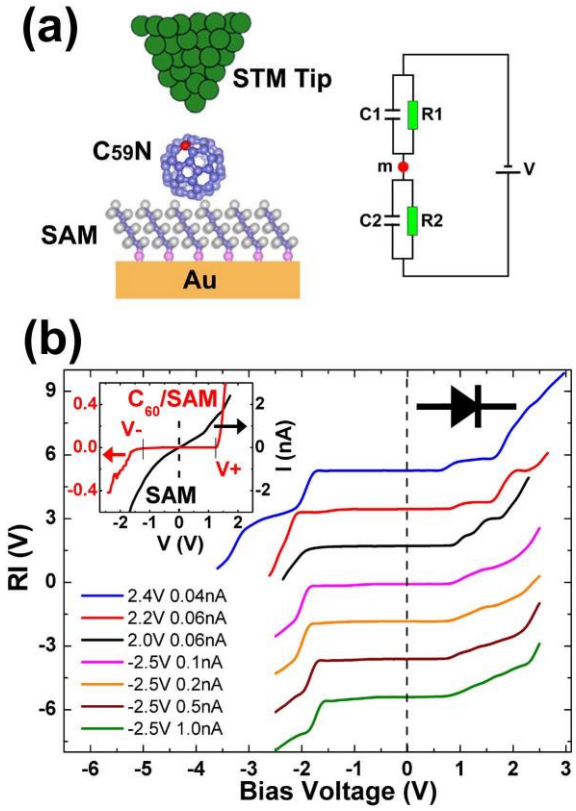

Figure. 1.2.2 Single $C_{59}N$ molecular rectifier and its rectification [11].

As developing for couple of decades, there are 3 distinct mainstream mechanism of the molecular rectifier [12]:

1) Schottky barriers interface dipoles, these molecules were called as “S” rectifiers.
2) Asymmetric configuration of the molecular chromophore within the metal-molecule-metal sandwich structure, called “A” rectifiers.
3) “U” rectifiers, which according to a process as true unimolecular rectification, in which the current exploits electron transfers between molecular orbitals, whose significant probability amplitudes are asymmetrically placed within the chromophore.

Even only the U rectifiers are what the scientist endeavor to achieve for half of century, the application of all the molecular rectifiers is promising in the near future.

1.2.2 Molecular wire

Any molecular devices need to be integrated into the circuit, thence molecular wire is aiming at carrying digital and electronic information from one end to the other end of a microprocessor that might be a few nanometers away. Consequently, as the key unit for executing the construction of circuit, molecular wire calls for stable structure, high transmission for any information go through and enough length. Up to now, molecular wire has two separated families, as metal ones and organic ones.

In 1998, Ohnishi *et al*. succeeded to fabricated a single gold atomic wire by exploiting ultrahigh-vacuum STM (UHV-STM) to depart the tip and substrate (Fig.1.2.3) [13].

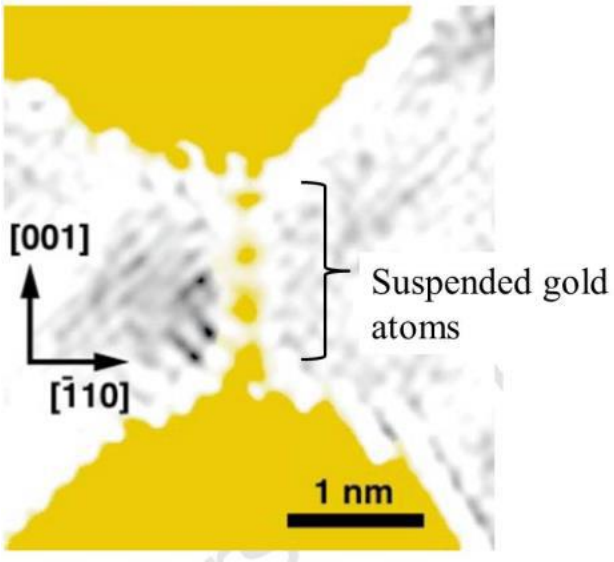

Figure 1.2.3 Electron microscope image of a linear strand of gold atoms (four coloured dots) forming a bridge between two gold films (colored areas) [13].

Another and main kind of molecular wire is organic wire, like π-stack, biomolecules, nanocarbon systems are even focused for decades.

The conjugate system means the electrons transport through the delocalized π conjugated system, which has high level performance for electron delivery. For instance, conjugated oligomeric chains, oligothiophenes, oligomeric, pyrrole, polyacetylenes, porphinrin and so

forth [14]. Tour group contributed to the synthesis of the molecular wire significantly. They developed an iterative disproportionation / convergence method could make the length of the molecule stretch as the 2^n times, where n is the degree of the iterative. The molecules were synthesized by Tour's method called 'Tour wire' [15].

For avoiding the strong aggregation of the molecular wires in solution and solid phase, the functionalized insulated molecular wire by polymerization of an insulated π-conjugated monomer has been synthesis [16-17].

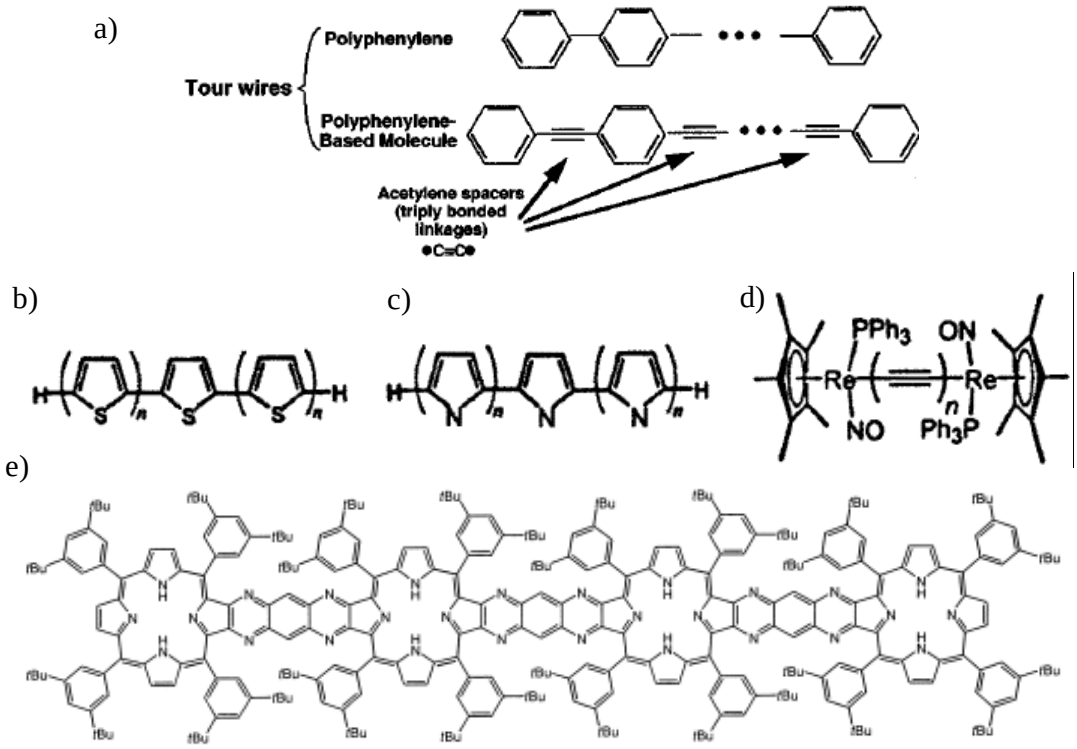

Figure 1.2.4 Schematic of molecular wire. a) OPE, oligo(phenylne ethynylenes)s) b) polythiophene, c) polypyrrole, e) porphyrinring [14].

DNA molecule has double-helix structure, as the main genetic information carrier has been discussion in multidisciplinary arena, as biology, genetics, pharmacy and physiology. In fact, in brain of human being the nucleic acid molecules play a role of information deliverer. Its stability, biocompatibility, electron transport property, imply it could be potential molecular wire in the near future. The molecular electronics begin to realize this application of the DNA molecule [18]. However, the electron transport mechanics for nuclei acid molecules is still not clear by far and the conductance behavior is also concern.

The advantage of the nanocarbons' electronic property also attract scientists' attention. Regards carbon nanotube has almost perfect structure in atomic level, represent another essential molecular wire [19].

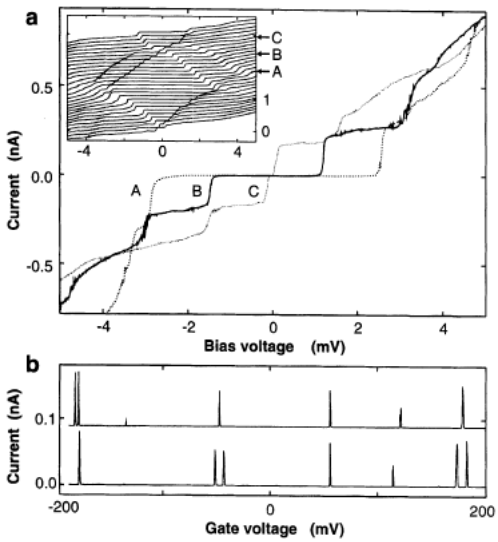

Figure 1.2.5 Current-Voltage curves of the nanotube [19].

1.2.3 Molecular switch and memory

As the basic control units in the circuit, the switch and memory are essential. Both of the switch and memory work as two different stable states for reversible conversable system. According to the external stimulations, such as electric field, current pulse, heat, illumination etc. act on the molecules, the conformation and chemical bond of the molecules break, generate, vibrate or rotate. These morphologic or chemical change give rise to the resistance high (0) or low (1) corresponding to the circuit turnoff or on. This process is considered as the information transmission. Howbeit, when the stimulation stops, the device changes from 1 to 0 is switch while memory does from 0 to 1.

Important reaction applied in the molecular switches. Whalley *et al.* examined the device conductance when constituent molecules, diarylethenes, switch between states of conjugation [20]. Recently, the Guo group exploit a single diarylethenes sandwiched covalently between graphene electrodes to construct a stable molecular switches with unprecedented levels of a fully reversible accuracy (on/off ratio of ~100), stability (over a year) and reproducibility (more than 100 cycles for photoswitching and more than 10^5 cycles for stochastic switching). Their results represents exquisite control over matter at nanometer length scales and is a worthy intellectual pursuit in its own right with broad, long-term benefits [21].

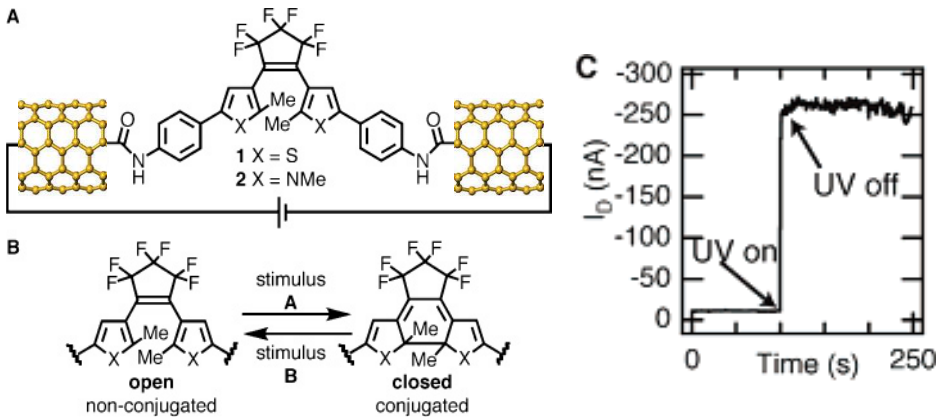

Figure 1.2.6 The switch molecule bridged on the single wall carbon nanotubes (SWNT) electrodes [20].

The oxidation-reduction reaction as another important reaction here for the two-state molecular devices has also drawn so many attentions. Gittins *et al*. used an organic molecules containing redox center, which can be changed reversibly by the oxidation-reduction reaction. With $bipy^{2+}$ oxidation state, there is no current go through the circuit, which means off. With the prosper bias voltage, the radical $Bipy^{+}$ let the current increase [22].

Another kind of two-state molecules, catenane and rotaxane have been reported as molecular switch and memory. Heath group proposed a [2]catenane-based solid state electronically reconfigurable switch [23]. They fabricated a bistable [2]catenene and sandwiched between an n-type polycrystalline Si electrodes and a Ti/Al top electrode. The device exhibits hysteretic *I-V* characteristics, can be open at +2V closed at -2V and could be recycled many times. The different position of the rings represents 0 or 1 state. They succeeded to fabricate 16-bite, 64-bite memory circuit in the further work, even executed a molecular electronic memory patterned at 10^{11} bit per square centimeter [24].

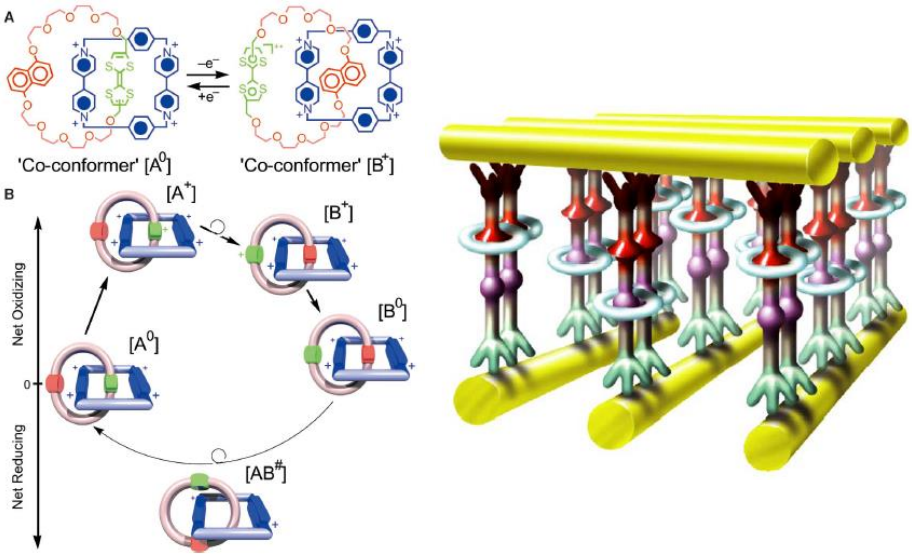

Figure 1.2.7 The principle of molecular switch made by catenane molecules (left), rotaxne molecules and cross wire technique (right) [23, 25].

In 2006, Riel *et al.* reported Au/ bipyridyl-dinitro oligophenylene-ethynylene dithiol molecule (BPDN-DT)/Au single molecular memory performed by MCBJ as a new mechanism memory. The BPND-NT contact strongly with the gold electrodes by –SH group [26]. This system could work at 100K, do the write, read, and erase voltage pulse pattern applied, resulting in switching "off" and "on" state. The ratio of the current of "off" state and "on" state was observed 7-70 times and can keep working in 30 seconds.

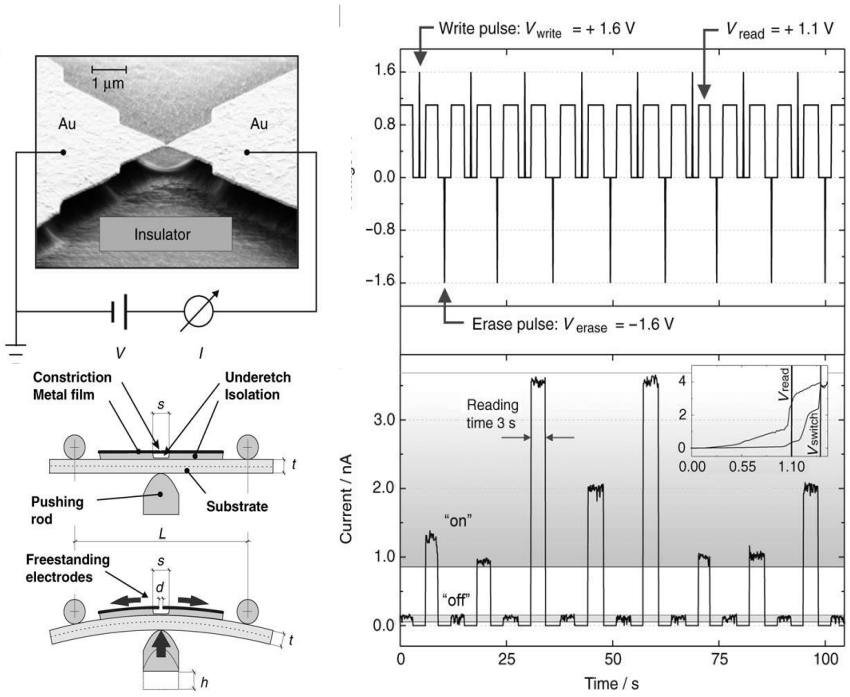

Figure 1.2.8 The principle of MCBJ (left), Memory operation of the BPDN-DT system (right): voltage pulse pattern applied, resulting switching between "off" and "on" state [26].

1.2.4 Molecular FET (Field Effect Transistor)

Field-Effect Transistor (FET) possess the advantages of switch and gain in the circuit that uses electric field to control the electrical behavior. Diversities of implementations of FET exist. Generally, FET display very high input impedance at low frequencies. The conductivity between the drain and source electrodes is controlled by an electric field, which is generated by the voltage difference between the body and the gate of the device. Transistor have continuously reduced in size, therefore, the quantum effect become increasingly importantly for device operation. Unlike the FET in solid state, Single Electron Transistor (SET) rely on Coulomb blockade effect and single electron tunneling effect.

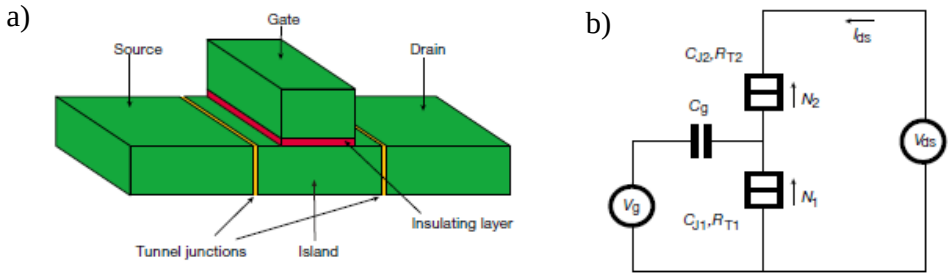

Figure. 1.2.9 Schematic of a) single-electron tunneling transistor (SET), b) circuit diagram of the SET [27].

The SET consists of two tunnel junctions placed in circuit (Fig. 1.2.9b). An 'island' is therefore formed between both of the junctions. The gate electrodes couples with electrostatically to the island. Total capacitance of the island C_Σ, which the sum of the

capacitances including gate's and junctions' $C_\Sigma = C_g+C_{J1}+C_{J2}$. If the island is sufficiently small, the charge energy of one extra electron in the island is $E_C = e^2/(2C_\Sigma)$, which caused by the coulomb rejection energy from the former electron go into or leave the system to the later electron. Thus, for the Coulomb blockade effect, here are two conditions. One is the E_c will be larger than the thermal fluctuations energy, namely, $E_C \gg k_BT$, where the T is temperature and k_B is the Boltzmann constant. Additionally, the resistance of the junction must be large compared with the quantum resistance $R_T \gg h/e^2$=25.8 kΩ [27].

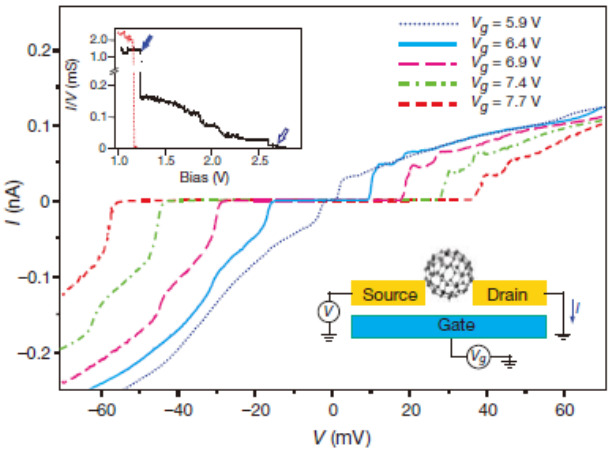

Figure 1.2.10 Schematic current–voltage (*I*–*V*) curves obtained from a single-C_{60} transistor at T = 1.5 K. Five typical *I*–*V* curves taken at different gate voltages (*Vg*) are shown [28].

The nanocarbons was the first consideration for the SET device. Park *et al*. reported the fabrication of an individual C_{60} molecule single molecular transistor utilizing Au electrodes (Fig.1.13). Their results demonstrated that the current changes as the function of the applied gate voltage. Also, the steps were observed in the *I*-*V* curves performed the quantum transport property of the carrier [28].

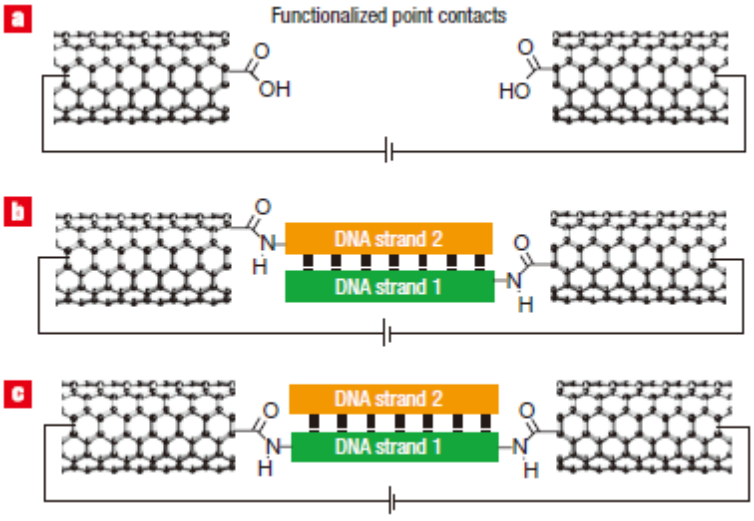

Figure 1.2.11 A method to cut and functionalize individual SWNTs with DNA strands [29].

As a reactive electrodes, a lithography-defined oxidative cutting process for fabricating SWNT point contacts has been reported [30]. This method make an amide bond achieved by

peptide chemistry, which is strong that could avoid the stochastic switching of thiols to neighbouring gold atoms observed in conventional gold electrodes making the amide bond more stable. As a result, the amide linkage is stable and selective for the special nano junctions. For instance, Guo *et al.* described a general method to integrate DNA strands between SWCNT electrodes and their electrical properties [29]. As mentioned above, the single molecular transistor exploit as biosensor is promising. He *et al*. measured directly the single molecule DNA hybridization dynamics with the carbon based transistor (Fig.1.2.12) [31].

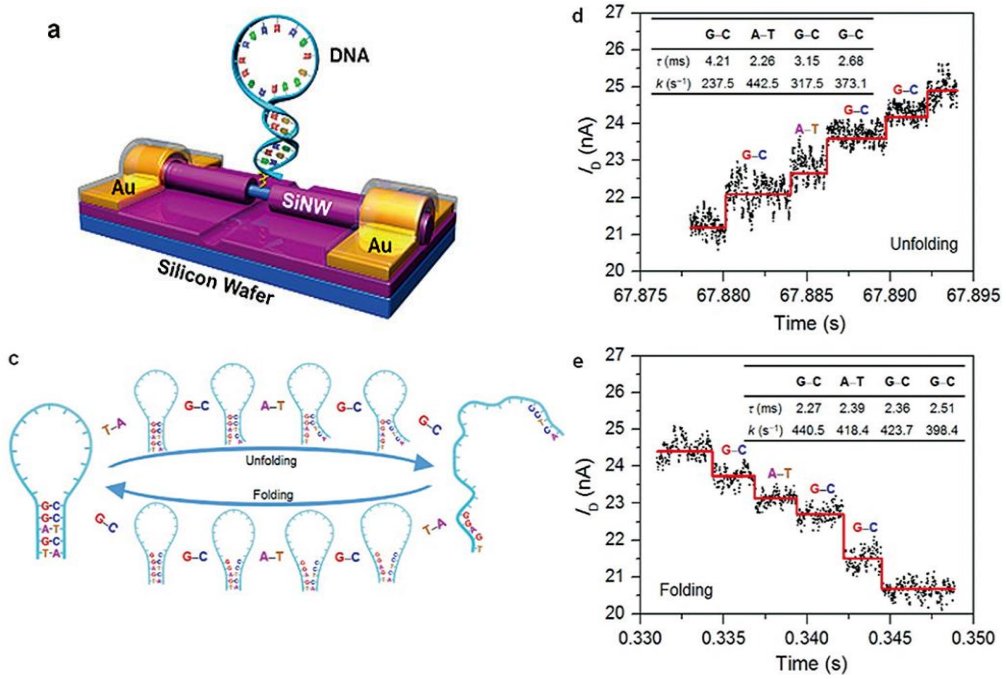

Figure 1.2.12 Schematic of a) Diagram of single-hairpin DNA-decorated SiNW biosensors. c) The kinetic zipper model for the unfolding and folding processes of a hairpin DNA with five base pairs in stem. d,e)Representative five-step increasing and decreasing data of Device 3. The inserts show the possible microstates of each plateau (G-C, A-T, G-C, and G-C) and corresponding kinetic parameters (lifetime t and rate k) [31].

Gated MCBJ is another choice of the SET. Xiang *et al*. developed a three-terminal junction combining both the stability single-molecule junction via MCBJ technique and the ability to shift the energy levels of the molecule by gating (Fig 1.2.13) [32]. The displacement between source and drain electrodes was precisely tuned by the piezo configuration while the gate electrodes coupled to shift the molecular energy levels. They demonstrated that the variation of the effective gate coupling can be attributed to a peak broaden without impact on the conductance shift obviously.

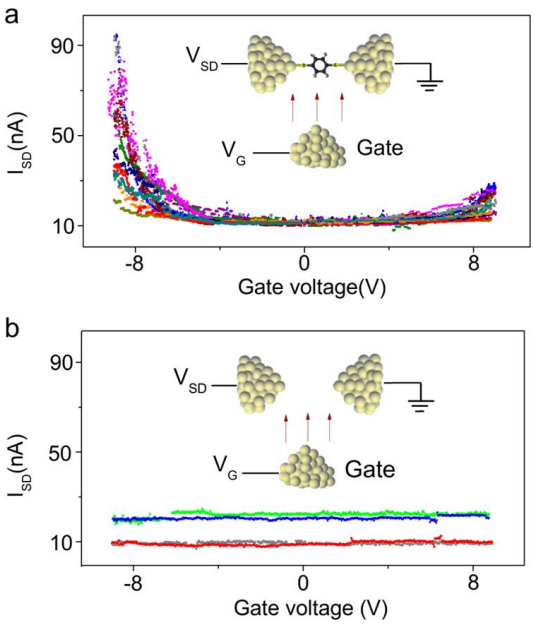

Figure 1.2.13 Source-drain current (I_{SD}) versus gate voltage (V_G) curves for the Au-BDT-Au molecular and molecule free three-terminal [32].

The molecular electronics developed for couple of decades, succeeded progressively both in theoretical and experiments. These achievements encourage more and more scientists to devolve in this promising field. However, the hardness is manifested at the same time. It will a long way to go until the molecular motors and circuits make benefit for our daily life.

1.3 Electron transport properties in nano contacts [33]

1.3.1 Theory of electron transport in nano scale conductor

In macroscopic, the electrical conduct following the Ohm's law, which is described that the current is proportional to the applied voltage. Set the conductance as *G*, for a transverse area *S* and length *L*, here is the Ohm's law:

$$G = \sigma \frac{S}{L} \qquad \text{Eq.1}$$

where the σ is the conductivity of the sample with a material specific property. The conductivities differ from material in macroscopic. The conductance is an importance quantity in any size of the electronics. In mescoscopic view, varieties of transport mechanisms work for different scale scattering regimes. Basically, the electron transport properties of one sample we interested can be proposed in related size, set the length scale of the sample as *L*. For evaluation of *L*, two critical indexes can be our references, the phase-coherence length and elastic mean free path. Set the fundamental length scale, the phase-coherence length, as $L\varphi$, which represent the distance about the phase of the electron wave function is persevered. The mesoscopic system, in specific, described in the scale of $L < L\varphi$. Additionally, the elastic mean free path, which measures the

displacement roughly between elastic collisions with static impurities, set as *l*. When $l \ll L$, the system operating in a diffusive regime, as Fig.1.3.2a exhibits with random movement in a step size *l* among the impurities. While $l > L$ shown in Fig.1.3.2b, the system work in a ballistic regime, momentum of electron could be assumed to be constant and limited within the sample boundaries.

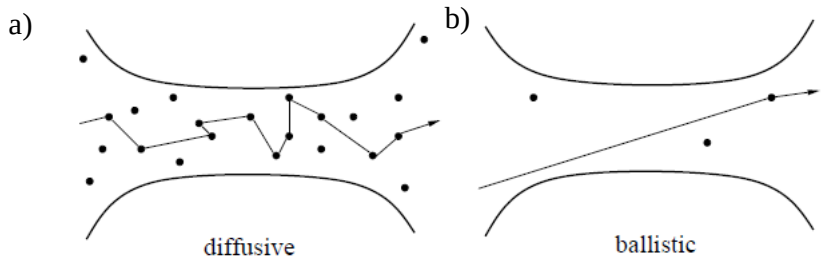

Figure. 1.3.1 Schematic image of a) diffusive and b) ballistic electron transport [34].

However, with the decrement of the size, when it comes to the atomic scale, the quantum confinement effect have impact on the electrical conduction, where the Ohm's law is not applicable any more. A main challenge for the theory is to derive conductance presented in macroscopic to an atomic scale. 1950's, Landauer developed the famous Landauer formula, which has never departed [33c]. The central idea of Landauer's approach is that assume a transport processes with inelastic interactions can be ignored, the problem become a scattered one. In another word, the transport issue like electrical conductance related to the transmission probability for an electron crossing the system. Therefore, we shall discuss the transmission probability in simple quantum theory first.

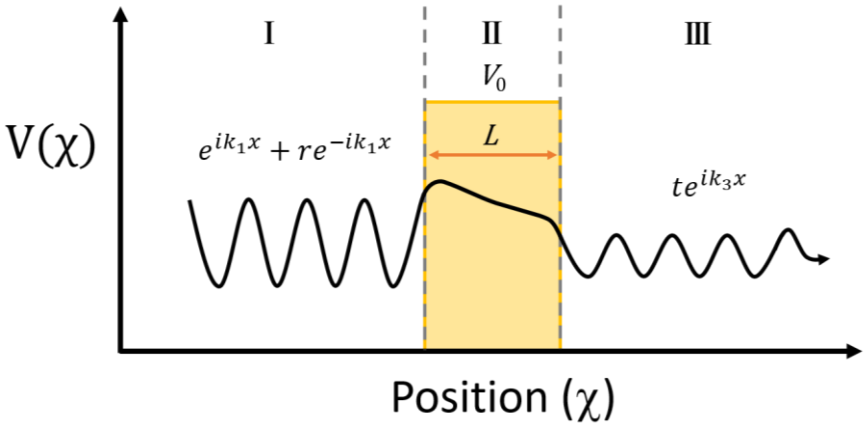

Figure 1.3.2 Schematic of electron tunneling through a rectangular barrier.

Generally, the electron tunnels through a molecular junction with two electrodes separated by molecule (s) is considered as one-dimension model with rectangular barrier, shown in Fig.1.3.2. Here, assume a free electron with energy *E* separated is likely to go through the rectangular barrier with energy Φ, which can be understood as the height, and thickness *d*. The time-independent Schrödinger in this scenario can be expressed as

$$\left[-\frac{\hbar^2}{2m}\frac{\partial^2}{\partial x} + V_0\right]\psi = E\,\psi \qquad \text{Eq.2}$$

Where *m* and *E* are the mass and the energy of incident electron, *V(x)* represents the barrier

potential. The wave functions in the related parts, say part I, II, III respectively, can be written as

$$\Phi_I(\chi) = e^{ik_1 x} + re^{-ik_1 x} \quad \text{Eq.3}$$

$$\Phi_{II}(\chi) = \alpha e^{k_2 x} + \beta e^{-k_2 x} \quad \text{Eq.4}$$

$$\Phi_{III}(\chi) = te^{ik_3 x} \quad \text{Eq.5}$$

Let us first assume the election energy smaller than the barrier potential, where

$$k_1 = k_3 = \frac{\sqrt{2mE}}{\hbar} \quad \text{and} \quad k_2 = \frac{\sqrt{2m(V_0 - E)}}{\hbar} \quad \text{Eq.6}$$

With the boundaries conditions of both sides as

$$1 + \mathrm{r} = \alpha + \beta; \;\; ik_1 - ik_1 r = \alpha k_2 - \beta k_2$$
$$\alpha e^{k_2 x} + \beta e^{-k_2 x} = te^{ik_3 x}; \;\; \alpha k_2 e^{k_2 x} - \beta e^{-k_2 x} = itk_3 e^{ik_3 x} \quad \text{Eq.7}$$

The relative probability of an incident electron transmitting the barrier, calls transmission coefficient can be expressed as

$$T = \frac{|t|^2}{|1|^2} = \frac{1}{1 + (\frac{k_1^2 + k_2^2}{2k_1 k_2})^2 \sinh^2(k_2 x)} = \frac{4E(V_0 - E)}{4E(V_0 - E) + {V_0}^2 \sinh^2(k_2 x)} \quad \text{Eq.8}$$

With a potential $\Phi \ll E$, transmission coefficient T can be easily deduced as

$$T = \frac{1}{1 + (\frac{k_1^2 + k_2^2}{2k_1 k_2})^2 \sinh^2(k_2 x)} = \frac{4E(E - V_0)}{4E(E - V_0) + {V_0}^2 \sinh^2(k_2 x)} \quad \text{Eq.9}$$

1.3.2 Landauer-Büttiker formula

In the practical experiments, it is actually much more complex system. Thus, the model presented in the previous section is not insufficient any more. In fact, the more rigorous model, where the important concept of multiple conduction channel will be arose in this section.

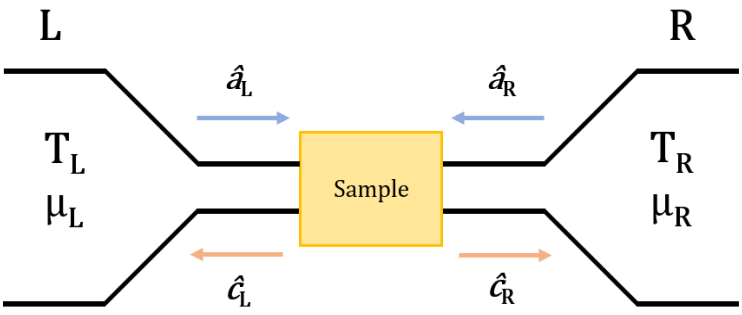

Figure 1.3.3 Schematic of a two-terminal scattering problem for the case of one transverse channel.

In this section, the model we shall consider as shown in Fig.1.3.2. A briefly introduction, suppose a sample in mesoscopic connected to "Left" and "Right" electrodes, here simplified as L and R. Consider the two electrodes as reservoirs, besides, both of them are

so large that can be described with temperature and chemical potential indexes $T_{L,R}$ and $\mu_{L,R}$. Here, the electron scattering is negligible. The reservoirs, which are the carriers source, are determined by the Fermi-Dirac distribution function, described as

$$f_\alpha(E) = \frac{1}{\exp\left[\frac{E-\mu_\alpha}{k_B T_\alpha}\right]+1} \quad \alpha = L, R \qquad \text{Eq.10}$$

where k_B is the Boltzmann constant. Assume that the electron transverse and longitudinal motions are separately. The longitudinal direction is so open that can be presented by the continuous wave vector k_l. Transverse motion is quantized and described by the discrete index n, which stands for the quantum number for the quantum channels. Additionally, the incoming and outgoing situation on the sample for each electrode are also suggested to be separated.

For expressing the outgoing states, we introduce the creation and annihilation operators as $\hat{a}_{\alpha n}(E)$, $\hat{a}^\dagger_{\alpha n}(E)$. For incoming state, we employ the operators as $\hat{c}_{\alpha n}(E)$, $\hat{c}^\dagger_{\alpha n}(E)$. The $\hat{a}_{\alpha n}(E)$ and $\hat{c}_{\alpha n}(E)$ operators were related by the scattering matrix $\boldsymbol{S}$,

$$\begin{pmatrix} \hat{c}_{L1}(E) \\ \cdots \\ \hat{c}_{RN_R}(E) \end{pmatrix} = \boldsymbol{S} \begin{pmatrix} \hat{a}_{L1}(E) \\ \cdots \\ \hat{a}_{RN_R}(E) \end{pmatrix} \qquad \text{Eq.11}$$

Similarly connect the creation operators $\hat{a}^\dagger_{\alpha n}(E)$ and $\hat{c}^\dagger_{\alpha n}(E)$ via the Hermitian conjugated matrix $S^\dagger$.

The matrix $\boldsymbol{S}$ has dimensions $(N_L+N_R) \times (N_L+N_R)$ in total, can be rewritten utilizing the transmitting (t) and reflecting state (r) as

$$\boldsymbol{S} = \begin{pmatrix} r & t' \\ t & r' \end{pmatrix} \qquad \text{Eq.12}$$

Here, the electron reflection back both reservoirs was presented via the quantum number. The dimensions in the square diagonal blocks $\boldsymbol{r}$ with size $N_L \times N_L$ while $\boldsymbol{r'}$ with $N_R \times N_R$. Moreover, in the off-diagonal rectangular blocks, the electron transmission through the sample can be described as $\boldsymbol{t}$ with size $N_R \times N_L$ while $\boldsymbol{t'}$ with $N_R \times N_L$. The properties of the matrix S are generalization to multimode cases, for instance, the flux conservation and time reversal symmetry implied the unitary and symmetric properties.

Besides, the current operator in the left lead can be expressed as via using the field operator $\hat{\boldsymbol{\Psi}}$ and $\hat{\boldsymbol{\Psi}}^\dagger$, as

$$\hat{\boldsymbol{I}}_L(z,t) = \frac{\hbar e}{2im} \int dr_\perp \left[\hat{\boldsymbol{\Psi}}^\dagger_L(\boldsymbol{r},t) \frac{\partial}{\partial z} \hat{\boldsymbol{\Psi}}_L(\boldsymbol{r},t) - \left(\frac{\partial}{\partial z}\right) \hat{\boldsymbol{\Psi}}^\dagger_L(\boldsymbol{r},t) \hat{\boldsymbol{\Psi}}_L(\boldsymbol{r},t) \right] \qquad \text{Eq.13}$$

$$\hat{\boldsymbol{\Psi}}_{\boldsymbol{L}}(\boldsymbol{r},t) = \int dE e^{-iEt/\hbar} \sum_{n=1}^{N_L(E)} \frac{\chi_{Ln}(\mathbf{r}_\perp)}{(2\pi\hbar v_{Ln}(E))^{1/2}} [\hat{a}_{Ln} e^{ik_{Ln}z} + \hat{c}_{Ln} e^{-ik_{Ln}z}] \qquad \text{Eq.14}$$

$$\hat{\boldsymbol{\Psi}}^\dagger_L(\boldsymbol{r},t) = \int dE e^{iEt/\hbar} \sum_{n=1}^{N_L(E)} \frac{\chi^*_{Ln}(\mathbf{r}_\perp)}{(2\pi\hbar v_{Ln}(E))^{1/2}} [\hat{a}^\dagger_{Ln} e^{-ik_{Ln}z} + \hat{c}^\dagger_{Ln} e^{ik_{Ln}z}] \qquad \text{Eq.15}$$

Where the $\mathbf{r}_\perp$ and z is the coordinates for transverse and along the leads (L to R), χ_{Ln} are the transverse wave functions. As an approximation, we can neglect the energy dependence of the quantities due to the negligible near the Fermi energy. Thus, the current can be rewritten as

$$\hat{\boldsymbol{I}}_L(t) = \frac{e}{2\pi\hbar} \sum_n \int dE dE' e^{i(E-E')t/\hbar} \left[\hat{a}^\dagger_{Ln}(E') \hat{a}_{Ln}(E) - \hat{c}^\dagger_{Ln}(E') \hat{c}_{Ln}(E) \right] \qquad \text{Eq.16}$$

Using the matrix $\boldsymbol{S}$ in Eq. 11 rewrite the Eq.16 in terms of the â and â† operators

$$\hat{\boldsymbol{I}}_L(t) = \frac{e}{h}\sum_{\alpha\beta}\sum_{mn}\int dEdE' e^{\frac{i(E-E')t}{\hbar}}\hat{a}^{\dagger}_{\alpha m}(E)A^{mn}_{\alpha\beta}(L;E,E')\hat{a}_{\beta n}(E') \qquad \text{Eq.17}$$

$$A^{mn}_{\alpha\beta}(L;E,E') = \delta_{mn}\delta_{\alpha L}\delta_{\beta L} - \sum_k S^{\dagger}_{L\alpha;mk}(E)S_{L\beta;kn}(E') \qquad \text{Eq.18}$$

Note that index α and β stand for the electrodes R, L respectively. $S_{L\alpha;mk}(E)$ represent the element of the scattering matrix related $\hat{c}_{Lm}(E)$ to $\hat{a}_{\alpha k}(E)$. The average from Eq.17 can be derived for a system at thermal equilibrium. The mean square of the annihilation operator is

$$< \hat{a}^{\dagger}_{\alpha m}(E)\hat{a}_{\beta n}(E') >= \delta_{\alpha\beta}\delta_{mn}\delta(E-E')f_{\alpha}(E) \qquad \text{Eq.19}$$

Combination with Eq.17 and Eq.19 with consideration of the unitarity the matrix $\boldsymbol{S}$, the current can be expressed as

$$I \equiv < I_L >= \frac{e}{h}\int_{-\infty}^{\infty} dETr[\boldsymbol{t}^{\dagger}(E)\boldsymbol{t}(E)][f_L(E) - f_R(E)] \qquad \text{Eq.20}$$

In the off-diagonal block regime, the matrix t, t_{mn}=$S_{RL;mn}$. At the zero temperature and limited voltage the electrical conductance G can be expressed as

$$G = \frac{e^2}{h}\mathrm{Tr}[\boldsymbol{t}^{\dagger}(E_F)\boldsymbol{t}(E_F)] \qquad \text{Eq.21}$$

The $\boldsymbol{t}^{\dagger}\boldsymbol{t}$ can be diagonalized, the transmission coefficients derived from the real set of eigenvalues, the value are available between 0 to 1. As eighnchannels or conduction channels are referred by the eigenfunctions. Instead of the Eq.20, we obtain the natural basis as

$$I = \frac{e}{h}\sum_n \int_{-\infty}^{\infty} dE\mathrm{T}_n(E)[f_L(E) - f_R(E)] \qquad \text{Eq.22}$$

With the spin degeneracy, the Landauer-Büttiker equation can be written as

$$G = \frac{2e^2}{h}\sum T_n \qquad \text{Eq.23}$$

The T_n is the transmission of the n channel, the conductance only rely on the transmission probability. $2e^2/h$ is the quantum unit, which can be expressed as G_0 with a value about 77 μS or 12.9kΩ.

1.3.3 Molecular devices electrical transport [35]

As we mentioned above, the experimental reality is a comprehensive issue. In specific, when the molecule go into the nano gap, the coupling of the molecule to the leads have impact on the transmission coefficient (T) associated with the each molecular orbitals and energy level. The coupling will attribute to a level broadening with amplitude t_1, t_2.

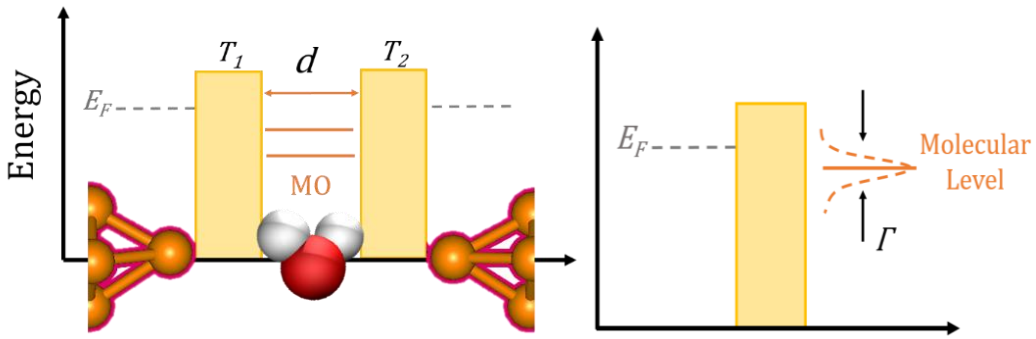

Figure 1.3.4 Schematic of image of resonant tunneling model with double barrier and image of the molecular junction (left) and schematic illustration of the energy coupling (right).

As shown in the Fig 1.3.4 left, instead of the ideal and simple model described by Landuaer formula, when the molecule is trapped in the nano gap, a double barrier system will form. To obtain the total transmission in the metal/molecule/metal structure, the transmission can be related to both of the double barrier, which has a total transmission amplitude *t*. This total transmission amplitude can be expressed as

$$t = \frac{t_1 t_2 e^{ikd}}{1 - r_1 r_2 e^{2kd}} \qquad i = 1,2 \qquad \text{Eq.24}$$

Where t_i is transmission, r_i is reflectance amplitude of the barriers, d is the distance between barriers and k is the wave number of the incident electron. The total transmission T can be rewritten as

$$T = \frac{T_1 T_2}{1 - 2\sqrt{R_1 R_2}\cos\theta + R_1 R_2} \qquad \text{Eq.25}$$

Set the total phase θ is the integer times of 2π. T has the maximum value

$$T_{max} = \frac{T_1 T_2}{(1 - R_1^{\frac{1}{2}} R_2^{\frac{1}{2}})^2} \qquad \text{Eq.26}$$

The maximum value corresponds to the resonance levels between the barriers. Electrons can transmit the double barriers with the maximum probability when the electron wave vector in the resonance level. However, the maximum value will not reach often. Thus, let us consider the other situation as $\theta = 2kd$. Set the wavenumber k_0 satisfies the condition of $2kd = 2n\pi$.

Here, if T_1, $T_2 < 1$ and the difference between k and k_0 can be ignored, T can be approximated to

$$\mathrm{T} \cong \frac{4\Gamma_L \Gamma_R}{(E - \varepsilon_0)^2 + (\Gamma_L + \Gamma_R)^2} \qquad \text{Eq.27}$$

Where $\varepsilon_0 = \hbar^2 k_0^2 / 2m$, $\hbar^2 k^2 / 2m$, $\Gamma_L = \hbar^2 k_0^2 T_1 / 4dm$, $\Gamma_R = \hbar^2 k_0^2 T_2 / 4dm$. The total transmission obey the Lorentzian distribution. $\Gamma = \Gamma_L + \Gamma_R$ displays the width of the resonant peak. The Eq.27 is Breit-Wigner formula. Finally, let us consider the electron transport in the single molecular junction. Suppose one molecular level (HOMO or LUMO) resonant with the electrodes Fermi levels. The transmission function can be expressed by Lorentzian

$$\tau(E, V) = \frac{4\Gamma_L \Gamma_R}{[E - \varepsilon_0(V)]^2 + (\Gamma_L + \Gamma_R)^2} \qquad \text{Eq.28}$$

Here, V is the applied bias voltage between the electrodes, $\varepsilon_0(V)$ is the energy of the

conduction orbital in the presence of the applied bias voltage V; Γ represents the coupling with metal-molecule and molecule-metal.

Besides, the electrons transport through the nano junction in several conduction mechanism. The transport mechanism depend mainly on the electrical contact properties [33b]. The other critical mechanism are listed in the Table 1.

Table 1. Type and Mechanisms of Conduction [36]

Conduction mechanism	Current density (J)	Temperature depedence	Voltage dependence
direct tunneling (low bias)	$J \approx V \exp(-)\frac{2d}{\hbar}\sqrt{2m\Phi}$	none	$J \approx V$
Fowler–Nordheim tunneling	$J \approx V^2 \exp\left(-\frac{4d\sqrt{2m}\,\Phi^{3/2}}{3q\hbar V}\right)$	none	$\ln\left(\frac{J}{V^2}\right) \approx \frac{1}{V}$
thermionic emission	$J \approx T^2 \exp\left(-\frac{\Phi - q\sqrt{qV/4\pi\varepsilon d}}{kT}\right)$	$\ln\left(\frac{J}{T^2}\right) \approx \frac{1}{T}$	$\ln(J) \approx V^{1/2}$
hopping conduction	$J \approx Vd \exp\left(-\frac{\Phi}{kT}\right)$	$\ln\left(\frac{J}{V}\right) \approx \frac{1}{T}$	$J \approx V$
space-charge-limited conduction	$J \approx V^2/d^3$	none	$J \approx V^n$

1.4 Fabrication and characteristics techniques

1.4.1 Fabrication of atomic size contact

To execute the molecular device, at first, it should integrate a molecule into the circuit. Thereby, the metal/molecule/metal is the basic structure of the molecular electronics. Here, one conception should be clarified that “single molecule” is not only the real one molecule, in a narrow sense, but also means few molecules. In this section, the most commonly utilizing methods will be described, which have been developed for last years since the first proposal of the molecular devices.

Generally, metal/molecule/metal junction has two categories of the investigate methods: one concentrates on the average behavior of the monolayer or multilayers of molecules; the other is in consideration of the single molecule electrical transport property. The former method has been observed since the 1960s. All the efforts on metal-molecule-metal junctions, actually, metal-layer(s) of molecule-metal junctions promoted the development of the molecular devices in clarification of the electron transport mechanism, fabrication and characterization of the molecular devices, including molecular rectifier, switches, negative differential resistance effect and so forth. However, the target is still single molecular junction, thus, the results utilizing metal-layer(s) of molecule-metal junctions has some limitation: a) not all the molecules interested could form the monolayer, let’s say, the molecules could be studied are limited; b) the molecule layer(s) has defects basically, this defect will interfere the results; c) in the molecular layer(s), the molecules are arranged so closely that interaction among the molecules could not be ignored. As a consequence, the metal-layer(s) of molecule-metal junctions did not satisfy the quest in the molecular electronics. Meanwhile, manifold variations of the techniques has been developed for atomic scale contacts and are permanently improved further. Here, we will end this section with a few brief remarks about the most widely applied fabrication methods and possible artifacts.

1.4.1.1 Mechanical Controllable Break Junction (MCBJ)

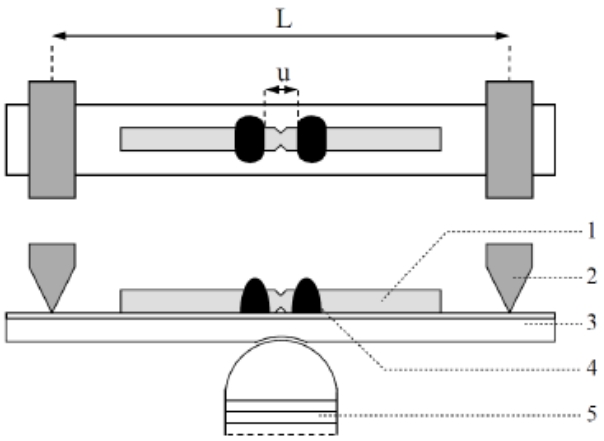

Figure 1.4.1 Schematic top and working principle of a MCBJ with 1) the notched wire, 2) two fixed counter supports, 3) bending beam, 4) drops of epoxy adhesive and 5) the stacked piezo element [34].

The mechanically controllable break junction (MCBJ) technique for studying atomic scale junctions was developed by Muller *et al*. [37]. The design concept is simple and basically consists of a metal wire (Fig.1.4.1-1) with a notched in the center, with fixed at the both end (Fig.1.4.1-4)). Stretch the wire using a piezo element (Fig.1.4.1-5) controlled by applied voltage, changing with its height to push the flexible substrate (Fig.1.4.1-3), which was fixed at the both sides by fixed counter supports (Fig.1.4.1-2). With voltage to the piezo element, its height varies and bend the substrate to stretch the wire until it break. This process can be repeat in an ultra-high vacuum (UHV) condition.

In the MCBJ, the setup itself acts as a reduction gear for the motion of the piezo element (δx) with respect to the relative displacement of the two electrodes (δy). For the ideal case of homogeneous strain in the bending beam, the displacement ratio (r) between δy and δx is given by

$$r = \frac{\delta y}{\delta x} = \frac{6tu}{l^2} \qquad \text{Eq.29}$$

where t, u and l are thickness of the bending beam, the distance between the epoxy droplets and the distance between the two counter supports, respectively. The displacement ratio was 5×10^{-3} for the present setup, with l=20mm, t=1mm, u=0.3 mm. The significance of this ratio could be understood considering the sample of a mechanically feasible displacement δx = 0.1μm for which δy is about 0.5 Å. This is about $1/5^{th}$ of the atomic diameter of an Au atom (0.255 nm). Hence, the spatial resolution of the MCBJ control is much smaller than the inter-atomic displacement, this property could be further improved using a piezoelectric element to push the bendable substrate. A spatial resolution well below 1 *pm* could be obtained in this way [38].

The MCBJ classified into two types based on the different preparation of the flexible substrate: notched wire break junctions and lithographic break junction (Fig.1.4.2).

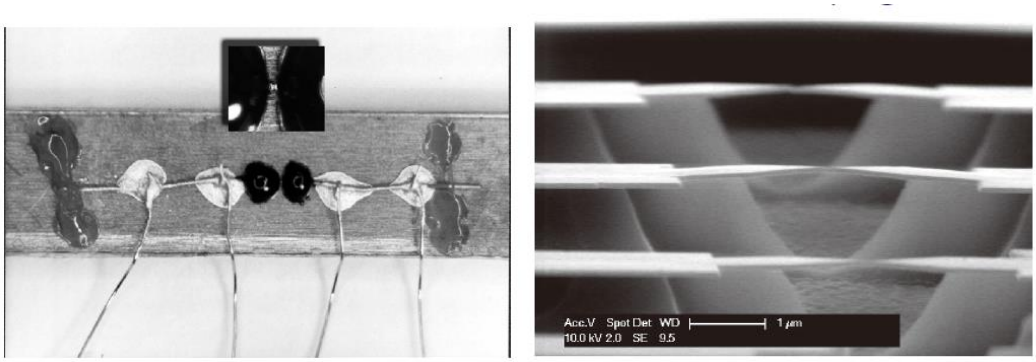

Figure 1.4.2 Photograph of a notched wire break junction (left), SEM image of lithographically fabricated break junctions, in this case three are formed on the same substrate (right) [34, 39].

Notched wire break junction is quite commonly utilized because it takes few procedures to prepare. Basically, it uses a metal wire with a notched carved in the center. Usually the notch is made by means of a surgical knife. At the notch the diameter of the wire reduced 25-50% of its original size. The wire fixed upon a polyimide tape covered phosphorous bronze substrate with epoxy adhesive. A top layer of polyimide tape acts as the insulator between the sample and the phosphorous bronze substrate. The substrate was mounted in a three-point bending configuration in a custom-made vacuum pot. The metal wire was broken at the notch by bending of the substrate. A single atomic contact could be formed just prior to the breaking of the wire. Once the junction broke, the piezodrivers is used to fine-tune the displacement between the two freshly cleaved surfaces.

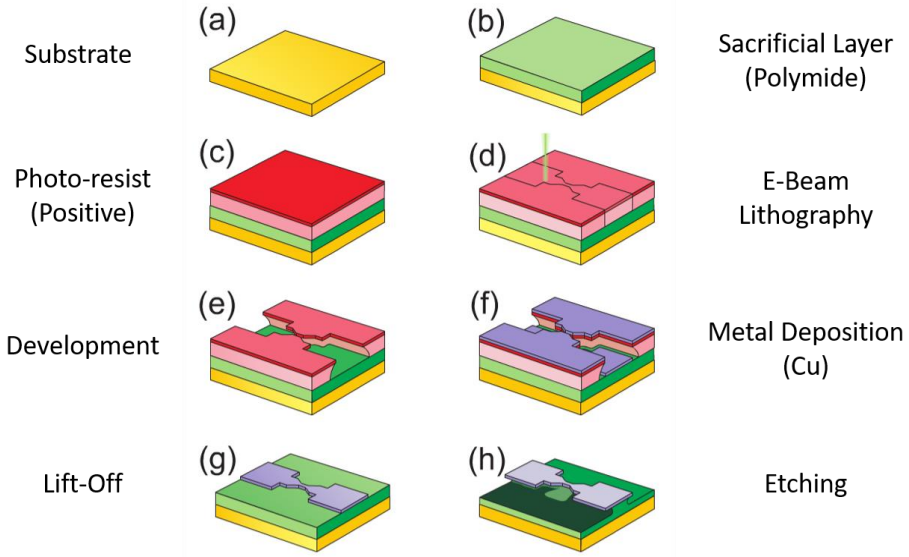

Figure 1.4.3 Photograph of a notched wire break junction (left), SEM image of lithographically fabricated break junctions, in this case three are formed on the same substrate (right) [33b].

The other type, lithographic break junction is made by Electron Beam Lithographic (EBL) processes. A typical EBL system consists of: 1) an electron gun or electron source that supplies the electrons. Usually, an electron gun is mounted at the top of an UHV chamber in order to maintain a collision free transport electron; 2) an electron column that 'shapes', deflect and focuses the electron beam; 3) a mechanical stage that positions the wafer under

the electron beam; 4) a wafer handling system that automatically feeds wafers to the system and unloads them after processing; and 5) a computer system that is used to control the various machine subsystems and transfer pattern information to the beam deflection coils. The processes describe briefly as the sample wire is formed by thermally evaporating a high purity metal film directly on a polished bendable substrate that is planarized by spin-coating of a polymer layer, often polyimide. The notch in the junction is formed exploited electron beam lithography, a freely suspended bridge is fabricated by a step of isotropic ion etching, which attacks the polyimide under the metal film. The lithographic junction is first broken and controlled by means of a mechanical gear and an electromotor drive (Fig.1.4.3) [33b, 39].

Both of the two types of MCBJ has its own benefit and disadvantages. The notched wire break junction has less stability but preparation easier. Reversely, the lithographic type fabrication process consumes more time but posses better stability. For measurement, the notched type is better for the discussion for conductance behavior while the lithographic type is better for the more specific spectroscopy. Since the instability of the MCBJ system, the MCBJ operate in ultra-high vacuum (UHV) environment. Hence, the MCBJ setup is a promising system to investigate the modeling system for the simple molecules, such as H_2, O_2, CO, N_2 etc. [40].

1.4.1.2 Scanning Tunneling Microscope (STM)

As a versatile tool allows investigating the topography and electronic property of low dimension surface with atomic resolution, the Scanning tunneling microscope (STM) is also ideal technique for exploration of the atomic-sized contacts. The basic idea behind STM is quite simple, as illustrated in Fig.1.4.4. In briefly, in its normal topographic mode, a sharp tip is scanned over the sample surface by controlling the current flows between the tip and surface due to the tunneling effect when applying a constant bias voltage. The tunneling current made separation between the tip and surface, only few the foremost atoms of the tip will interact with the sample surface, which is possible to achieve atomic resolution. The signal recorded by the program gives a topographic visual information, says image, of the sample surface. Typical operating currents are able to separate the tip and sample by nearly an order of magnitude for every 1Å [41]. Piezodrivers give a subnanometer accuracy to the relative position of the tip and sample. Conventionally the lateral scan directions are termed *x*- and *y*- directions and the vertical direction is the *z*- direction.

It is possible to fabricate clean metallic contacts in non-UHV conditions by utilizing STM. After conventional cleaning of tip and sample prior to mounting in the STM. By repeatedly crashing the tip on the spot of the sample the contacting surfaces of tip and sample are cleaned in situ where the contact is to be formed, shown in Fig. 1.4.5. This procedure pushes the impurities aside making clean metallic contact work.

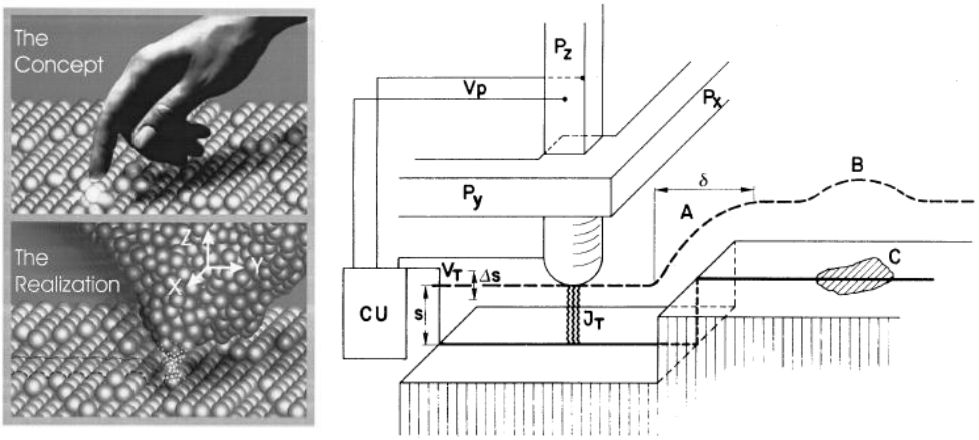

Figure 1.4.4 Conception (left) and Principle (right) of operation of the scanning tunneling microscope (schematic, not to scale). The control unit (CU) applies the necessary voltage V_p to the piezodrive P_z to maintain constant tunnel current J_T at bias voltage V_T. The piezodrives P_x and P_y scan the metal tip over the surface [41].

In an STM measurement on metallic contact, the bias voltage is kept constant and the results are typically presented as a plot of the conductance (current) versus z-piezovoltage (time). For investigating nano-scale contacts, mechanical stability of the STM setup is an important factor. Careful design makes possible to achieve noise vibration amplitudes of the order of a few picometers at low temperatures.

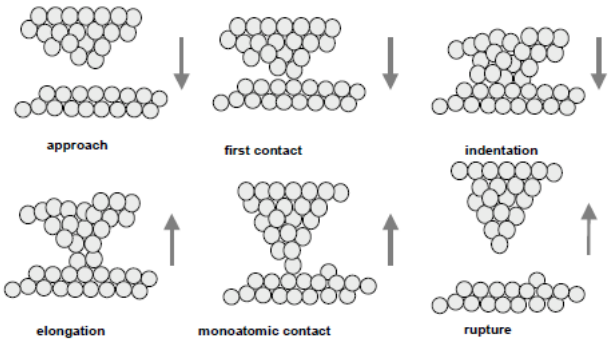

Figure 1.4.5 The dynamics representation of the contact fabrication using an STM [34].

Another adequate feature of STM is imaging. Unlike the MCBJ setup, the STM system could be ‘seen’. The most reasonable definition would be that a STM topograph is a contour of constant surface charge density. The STM works relying on the quantum tunneling effect, which refers to the quantum mechanical phenomenon where a particle tunnels through a barrier that it classically could not surmount. If the barrier is not infinite high, the particle tunnels the barrier possibly. STM yield precisely a contour of constant charge density, with the direct calculation for the transmission coefficient for an electron incident on the vacuum barrier between the tip and surface. Soon after the invention of STM, Binnig *et al*. reported the first atomic-resolution images (Fig.1.4.6) [43]. Even their topography was not clear on the atomic scale on that time, this method still a breakthrough for the modern nanotechnology.

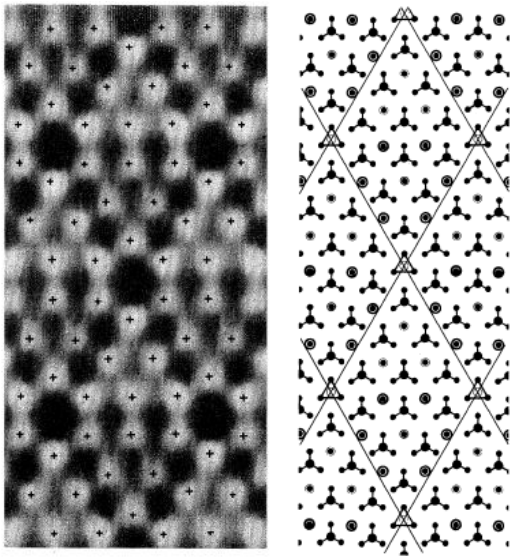

Figure 1.4.6 The first STM image and its modified adatom model [42].

The materials of tip and metal surface could be chosen in a wide range. The main drawbacks are its limited stability with respect to the change of external parameters such as the temperature or magnetic fields and the short lifetime of the contacts in general caused by the sensitivity of the STM to vibrations. Fortunately, the tip and substrate could be modified easily to enhance the stability and also endow the tip and substrate selectivity [44].

1.4.1.3 Atomic Force Microscope (AFM)

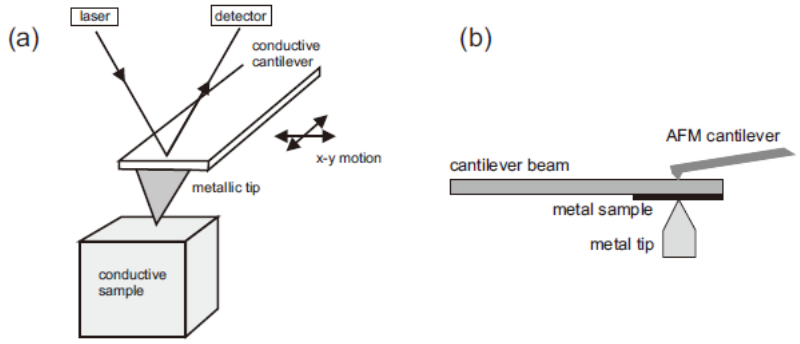

Figure 1.4.7 Fabrication and characterization of atomic contacts with an atomic force microscope (AFM). (a) The conductive AFM uses a conductive cantilever and metallic tip for recording the electrical signal. The deflection of the cantilever beam is detected optically and used for recording the topographic information of sample [45]. (b) In the combined AFM-STM the sample is clamped to a cantilever. The metallic contact is formed between the sample and the metal tip. The metal tip is part of an STM and records the electrical signal. The deflection of the cantilever is recorded with a separate AFM. This signal is used for measuring the force acting on the cantilever when the atomic contact rearranges [46].

Another scanning probe technique which complements STM in many aspects is the Atomic Force Microscope (AFM). Instead of the tunnel current AFM takes advantage of the distance dependence of the force between a fine tip and a surface. Depending on the chemical nature of both the tip and the surface, the force consists of several contributions and its displacement dependence might be complex and even nonmonotonic. AFM works

based on the principle of the measurement for force by recording the deflection of a cantilever that carries the tip. The deflection can be detected by optical means or by the detuning of an oscillator circuit due to the deflection. In surface science, the AFM has become a very versatile tool which works in various environments and temperature ranges. Compared to the STM the advantage of AFM is its possibility of working on insulating substrates. AFM works by force characterization, furthermore, the so-called AFM whose tips covered with metallic surface could record force and current information simultaneously.

MCBJ, STM, AFM as the most commonly used in the surface science, especially for the nano sized contact studies. Besides, more fabrication methods, such as transmission electron microscope, electromigration technique, electrochemical methods, fixed electrodes, nanopore method is under development, and never going to stop [33b, 47].

1.4.2 Characterization techniques for molecular electronics

The low dimensional technique, no matter electrical analyzer MCBJ, STM or force analyzer AFM, can attain a distance resolution of sub-angstrom level with high stabilities. Thus, with the versatile techniques, it being very simple to investigate the properties of individual atomic level contacts. In order to understand the conduction and other properties through the molecular junction, which is the main goal of the monograph, it is needed to characterize the atomic contact first. At present, there are five primary categories techniques to characterize the molecular junctions: microscopy, electrochemistry, electrical, optical and optoelectronic. Each method posses its unique advantages. The microscopic methods including STM, AFM etc., which have been discussed in previous section, the electrochemical technique is so classic that falling beyond our interest. Here, we shall mainly address the most commonly employing electrical and optical methods, including conductance characterization, Current-Voltage characterization (*I*-*V*), Inelastic Electron Tunneling Spectroscopy (IETS), Surface Enhanced Raman Spectroscopy (SERS).

1.4.2.1 Conductance characterization

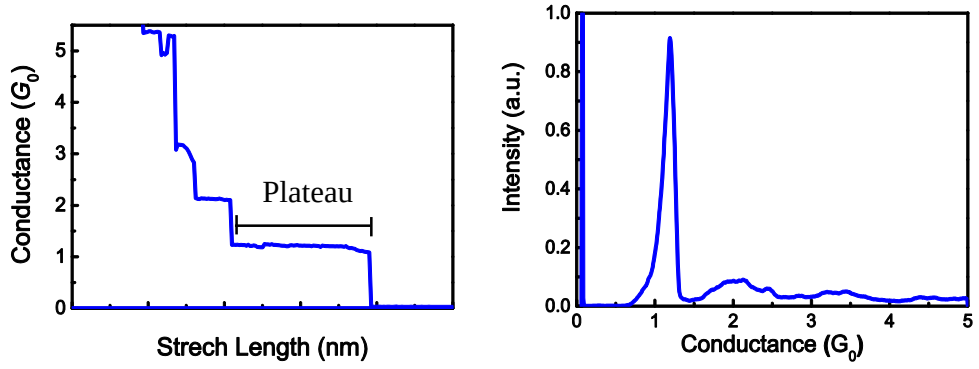

Figure 1.4.8 Typical conductance trace (left) and conductance histogram (right) of the Au atomic contact with bias voltage of 100 mV utilizing MCBJ setup.

Before introduce any molecules into the junction, first of all, we shall address the basic question: what is the conduction behavior of a metallic atomic contact? As mentioned in previous section, the metallic atomic contact can be fabricated by means of methods. Whatever the method will be used, it is evident that during the breaking processes, the conduction will change in some principle. With basic physical common sense, we could expect a gradual decrease in the conductance upon the distance increasing. This is correct when the atoms in the bulk regime but when these atoms was stretched in atomic level what will happen? Fig.1.4.8 shows the typical conductance traces (left) and conductance histogram (right) of Au atomic contacts. It is remarkable to see that the conductance indeed reduces in a step fashion upon stretching the contact. The conductance decreases by sudden jumps, separated by "plateau". The conductance of the Au metallic atomic contact are remarkably close to multiples of the conductance quantum as 1 G_0 ($G_0 = 2e^2/h$), 2 G_0, 3 G_0. This behavior resembles the conductance quantization in atomic contacts. However, most of the metallic atomic contact cannot be identified with integer multiples of the quantum conductance. And the structure and height of the conductance traces could vary by more than a factor of 2, where both smaller and larger steps are reported [33b].

Another remarkable feature to be noted here is that the conductance plateau shown in Fig. 1.4.8 left is long before the conductance vanishes even break. This long plateau can be understood in terms of the formation of the atomic wire, while the other metals did not be observed [48]. The conductance traces change not only from realization to realization, but also clearly different for distinct metals, here some samples shown in Fig. 1.4.9. In the case of Au contact, the conductance traces seems smooth. For the bare Al contacts, many plateaus have an anomalous slope, which resembles the conductance increases when pulling the contact, while the Pd contact conductance decrease slightly with stretch. These results imply when the contacts are elongated, different arrangements can be achieved. Additionally, the shape of the conductance traces also depend on the technique for fabrication of the nano contacts.

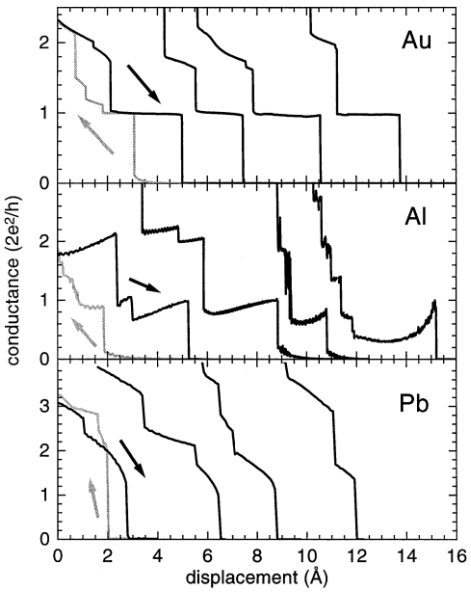

Figure 1.4.9 Evolution of conductance versus tip-sample relative displacement for several representative nanocontacts in STM at low temperatures [49].

The conductance traces give individual information of each pulling process an differ from sample to sample as we discussed. However, the feature are certainly reproducible. In order to investigate objectively the intrinsic conductance of the nano junction, a gathering of conductance traces can give information, namely, conductance histogram. Conductance histograms were constructed from over thousand even ten thousand of conductance traces obtained during the breaking process. The information can be obtained are largely dominated by the presence of the peaks location and height. As the Fig.1.4.8 right displays the Au atomic contact dominated 1 G_0, while additional peaks close 2, 3 and 4 G_0 are also observed. Typical conductance histograms of distinct metallic atomic contacts shows in Fig. 1.4.10. One thing need to be noted that the conductance histogram are generally sensitive to experimental conditions [33b].

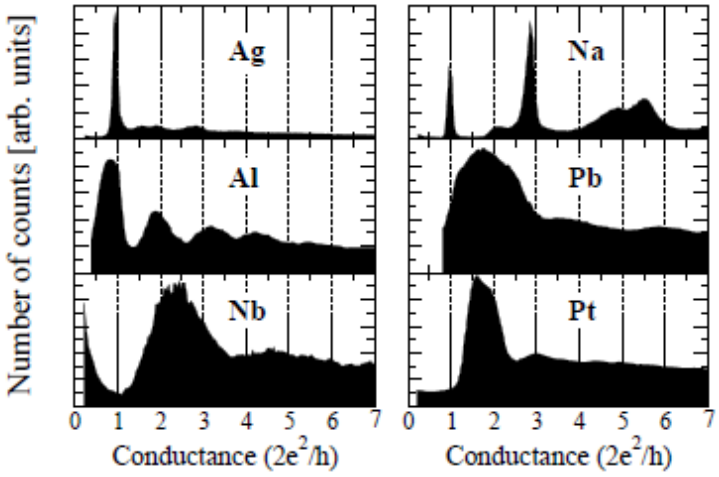

Figure 1.4.10 Conductance histograms of several metals obtained using MCBJ technique [33b].

1.4.2.2 Current-Voltage characterization (*I-V* curves)

In a metallic contact, the investigation of electron transport property of the metal/molecule/metal is essential. The metal/molecule/metal system is considerably much more complicated than the metallic atomic contact due to the uncertain molecule electronic structure, reaction in the interface and the molecule internal degree of freedom. Thus, only conductance behavior consideration is not sufficient any more. The current-voltage response (*I-V* curves) can obtain more electronic structure of junction.

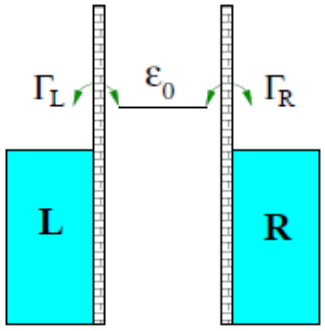

Figure 1.4.11 Level scheme of a molecular junction, the transport is dominated by a single level, ε_0. where ε_0 and $\Gamma_{L(R)}$ are the energy of the conduction orbital and the electronic coupling between the molecule and the metal electrode, respectively [33b] .

Basically, different molecular orbitals can participate in the electron transport simultaneously. However, many situations where only one level (HOMO or LUMO) locates close to the Fermi level of the metal electrode. Therefore, the transport is dominated in a certain voltage range. Within the single channel transport model, as Fig. 1.4.11 shows. As discussed in the section 1.3.3, the current through the molecular junction can be expressed by the transmission as

$$I(V) = \frac{2e}{h}\int_{-\infty}^{\infty} dE\ \tau(E,V)[f_L(E) - f_R(E)] \qquad \text{Eq.30}$$

where e, h, V, $\tau(E,V)$, $f_{L,R}(E)$ are the elementary electric charge, Planck's constant, bias voltage, transmission coefficient, and the Fermi distribution function of left and right electrodes, respectively. The factor 2 is due to the spin symmetry of the problem.

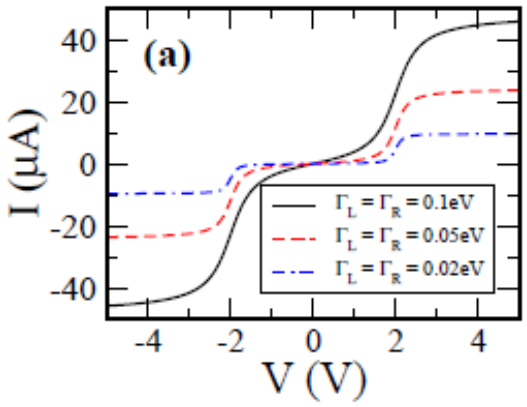

Figure 1.4.12 Current vs. bias voltage in the resonant tunneling model for a level position ε_0 = 1 eV (measured with respect to the Fermi energy of the electrodes) and at room temperature (k_BT = 0.025 eV). The different curves correspond to different values of the scattering rates that are assumed to be equal for both interfaces [33b].

To more specific electronic structure, we could analysis the shape, especially the symmetry of the *I-V* curves. Assume the moment that voltage drops symmetrically in both sides interfaces and therefore $\varepsilon_0(V) = \varepsilon_0$. This situation could be expected when the coupling in both side are equal ($\Gamma_L = \Gamma_R$). When electronic temperature, T, is set to 0 K, the Eq. 30 can be analytically described as

$$I(V) = \frac{8e}{h}\alpha(1-\alpha)\Gamma\left\{\arctan\left(\frac{\alpha eV-\varepsilon_0}{\Gamma}\right) + \arctan\left(\frac{(1-\alpha)eV+\varepsilon_0}{\Gamma}\right)\right\} \qquad \text{Eq.31}$$

where $\Gamma = \Gamma_L + \Gamma_R$ and $\alpha = \Gamma_L / \Gamma$. By fitting the experimental results with Eq. 31, asymmetric factor α, energy of the conduction orbital ε_0, and the electronic coupling ($\Gamma_L + \Gamma_R$) could be obtained. The Fig.1.4.12 shows a schematic of how the *I-V* curves looks like [33b]. Here, the current is symmetric shape. In contrast, Fig. 1.4.13 performs an asymmetrical *I-V* curves. The symmetry of the *I-V* curves played a prominent role in the molecular devices. As we presented before, the first conception of molecular electronics was molecular rectifier, which has asymmetrical *I-V* curves, namely, rectification.

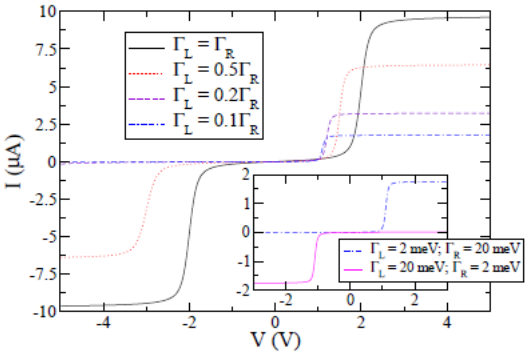

Figure 1.4.13 *I-V* characteristics in the resonant tunneling model for an asymmetric situation for ε_0 = 1 eV, Γ_R = 20 meV and at room temperature (k_BT = 25 meV). The different curves correspond to different values of the left scattering rate. The inset shows very asymmetric situations where the scattering rates have been interchanged. Notice that the *I-V* curves exhibit a clear rectification behavior [33b].

1.4.2.3 Inelastic Electron Tunneling Spectroscopy (IETS)

The characterization methods discussed in previous section concentrated on the electrical properties of the molecular devices. Nevertheless, the electrical properties derived from the average of the electrons behavior in the junction. It is difficult to classify what happened in the small gap by electrical properties characterization. However, in the about one of tenth of electron energy level, the vibration energy give us more specific information associated with the interaction between the transporting electrons and the molecular vibrations, making a primary characterization technique to identify the chemical species and supply the fingerprint information on the molecular electronics. By means of Inelastic Electron Tunneling Spectroscopy (IETS), the active vibration modes of a molecule, as well as the vibrational energies, can be aware of. Moreover, the ultrahigh sensitivity of IETS lead to an understanding of the molecular adsorption site, orientation, and changes in boning upon reaction [50]. Additionally, IETS is not subject to the selection rules as infrared or Raman spectroscopy. These advantages make IETS a powerful tool in the molecular devices [51].

Figure 1.4.14 displays the expected IETS behavior as the applied voltage V increased. When a negative bias is applied to the left electrode, the Fermi level is lifted. An electron in the junction with an occupied state on the left electrode tunnels into the junction to an empty orbital on the right side with a conserved energy as known as an elastic tunneling process [52]. However, when bias voltage applied is large enough, say $e\mathrm{V} \geq h\nu$, then the electron is possible to loss a quantum of energy $h\nu$ to molecule with a frequency ν, which possess a vibration mode localized inside this barrier. This process opens an inelastic tunneling channel for the eletron, and its overall tunneling probability is increased. The *I-V* signal shows a kink that is function of the applied bias. Typically, only a small fraction of electrons inelastically tunnel through the junction because of the small cross-section for such an excitation, thus, the current only manifests a small change. Since the difficulty of distinguish the small kink steps, it is more conventional to exploit the differential conductance (*dI/dV vs* V) even d^2I/dV^2 plots, where each phonon mode is activated can be clearly to clarify.

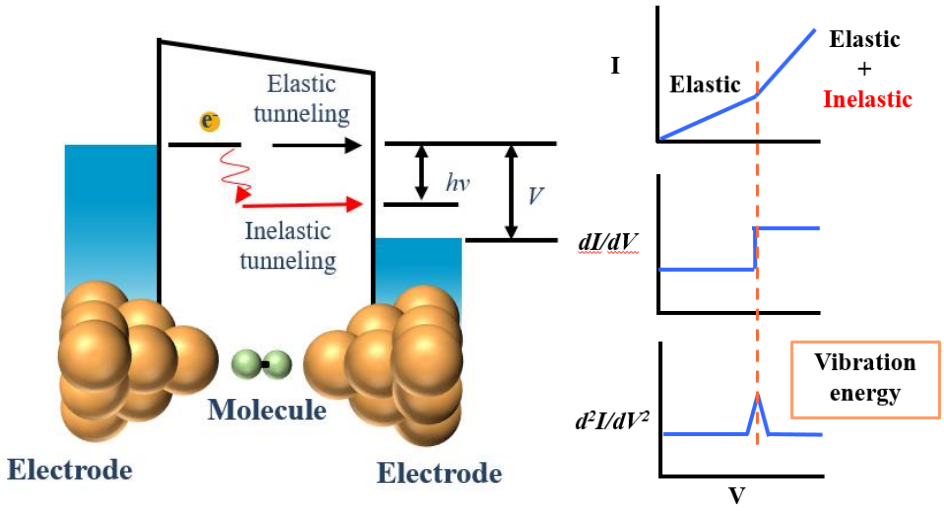

Figure 1.4.14 Expected inelastic electron tunneling spectroscopy (IETS) behavior as the applied voltage increases via a vibrational resonance. For a bias energy (eV) larger than the vibrational energy ($h\nu$), the transporting electron can deposit $h\nu$ onto the molecule to excite the molecular vibration mode. An additional transmission channel then is open, resulting in a current increase. The change caused by opening the vibrational resonance channel at eV = $h\nu$ becomes a step in the differential conductance (dI/dV) plot and a peak in the d^2I/dV^2 plot. A plot of d^2I/dV^2 versus V is typically referred to as the IETS spectrum.

The IETS signal is obtained by a mathematical differential approach that computes the numerical derivatives of the directly measured *I-V* curves [36, 53]. In principle, IETS signal is proportional to the second derivative of the current-voltage response, can be directly measured by an AC modulation method employing a lock-in amplifier.

In this strategy, a small AC voltage with a certain frequency ω is superimposed on the main DC bias so that the current *I(V)* can be written as

$$I(V) = I(V_0 + \mathrm{V}_{ac}\cos(\omega t)) \qquad \text{Eq.32}$$

With the Taylor series expansion about $\mathrm{V_{dc}}$, the Eq. 32 can be rewritten as

$$I(V) = \mathrm{I}V_0 + \frac{dI}{dV}\Big|V_{ac}\cos(\omega t) + \frac{1}{2}\frac{d^2I}{dV^2}\Big|_{V_0}[V_{ac}\cos(\omega t)]^2 + \cdots \qquad \text{Eq.33}$$

Rewritten Eq. 33 with a trigonometric double angle formula as

$$I(V) = \mathrm{I}V_0 + \frac{dI}{dV}\Big|V_{ac}\cos(\omega t) + \frac{1}{4}\frac{d^2I}{dV^2}\Big|_{V_0}\left[{V_{ac}}^2\cos(2\omega t)\right] + \cdots \qquad \text{Eq.34}$$

Thus, by measuring the *I-V* characteristics of the system at a fixed frequency ω as the DC bias sweep slowly, an IETS signal, which is the differential conductance could be achieved. To date, the AC modulation technique using a lock-in amplifier is conventional method for the IETS measurement [50].

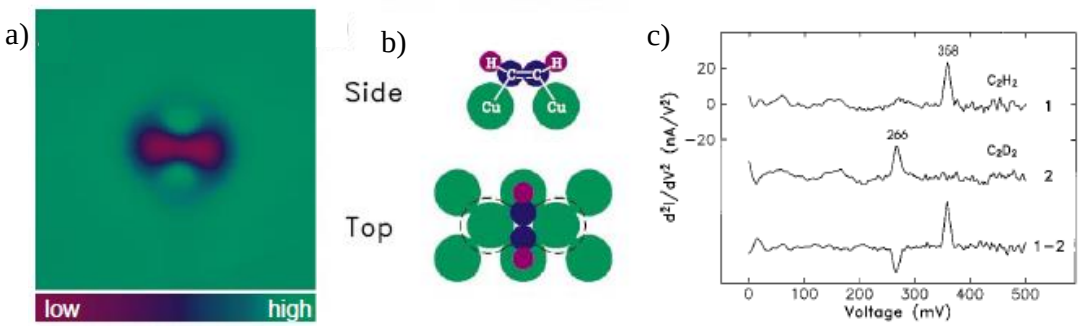

Figure 1.4.15 a) STM image of a C_2H_2 molecule on the Cu(100) surface at 8 K; b) Schematic drawing showing side and top views of the molecule's orientation and suggested adsorption site; c) Background difference d^2I/dV^2 spectra for C_2H_2 (1) and C_2D_2 (2), taken with the same STM tip, show peaks at 358 mV and 266 mV, respectively [50].

The IETS possess ultra-high sensitivity, is capable of mapping the phonon activation within the molecule adsorbed on a solid surface to perform a type of phonon imaging. Stipe *et al.* reported that the vibrational microscopy from the spatial imaging of the inelastic tunneling channels even could be employed to distinguish the C_2H_2 and C_2D_2 isotopes molecules on the Cu(100) surface [50].

1.4.2.4 Surface Enhanced Raman Spectroscopy (SERS)

In molecular devices, the optical characterization methods has not yet been used as a standard tool are reasonable: a) in a conventional vertical meta/molecule/metal configuration, the light is still hard to penetrate the metal electrode to probe the molecular layer; b) even the light go through the metal/molecule/metal junction, however, the structure is as small as a single molecular level, implying a limited signal-to-noise ratio. However, the IETS discussed in the previous section calls for the UHV conditions. From the application view, vibration spectroscopy at room temperature as well as *in-situ* characterization are desirable. As an optical analysis method, the Surface Enhanced Raman Spectroscopy (SERS) technique fill the blank of the powerful optical tool for the molecular devices, since it has been developed. This technique involves shining a monochromatic light source on a sample and analysis the scattered light. The majority of the scattered light with the same frequency as the incident source, which is known as Rayleigh or elastic scattering. A very small proportion of the scattered light shifted up or down in energy from the excitation laser due to the interactions between the incident electromagnetic waves and vibrational energy levels of the molecules in the sample. The difference in the energies leads to a shift in the emitted photon's frequency away from the incident light wavelength. By plotting the intensity of this shifts versus frequency results in a Raman spectrum of the sample. In another words, the energy shifts and the corresponding wavenumber shift offer messages on the vibrational mode.

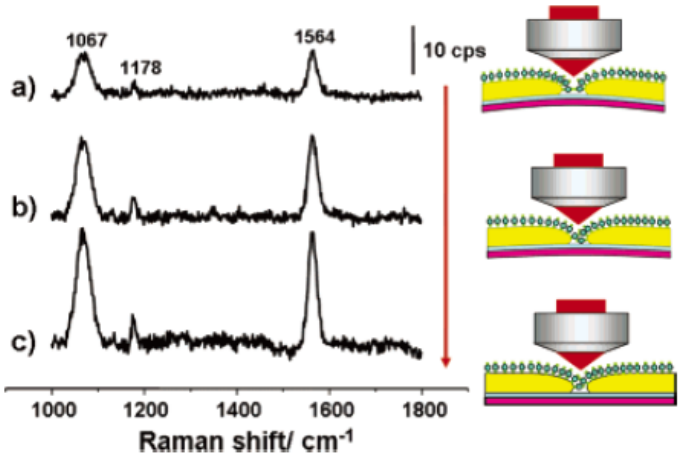

Figure 1.4.16 SERS of 1, 4-benzenedithiol (BDT) in the nanogap with the process of bending the metallic electrodes pair. The gap width is reduced, from (a) 8 Å, (b) 6 Å, (c) 4 Å. Laser: 632.8 nm [54].

Currently, in accordance with the command for identifying an unknown molecule in the single-molecular level, the Surface Enhanced Raman Spectroscopy (SERS) technique, in which an enormously enhanced Raman signal is detected when molecules adsorbed onto the coarse metal surface. In general, the enhanced signal of SERS are mainly came from the electromagnetic and chemical reactions. Tian *te al*. measured the SERS of 1,4-benzenedithoil in the nanogap with a combined SERS-MCBJ method firstly [54]. As the Fig. 1.4.16 performed, with the decrement of the displacement of the electrodes, the SERS signal increased exponentially. Kiguchi group investigated the dynamics of the single molecular device with MCBJ-SERS technique, as shown in Fig.1.4.17 [55].

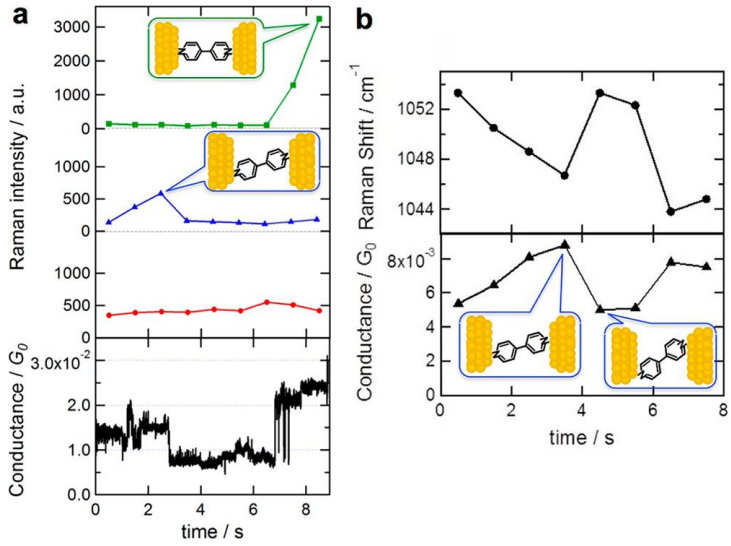

Figure 1.4.17 a) Time course of the Raman intensity of the a mode (red), b_1 mode (blue), and b_2 mode (green) together with the conductance of the molecular junction. b) Time course of the energy of the b_1 mode of the ring breathing around 1050 cm^{-1} and the conductance of the single molecule junction. Schematics of the relevant molecular orientation are shown as insets [55].

With development for decades, the characterization methods are much more than we

presented here. Beyond all the methods discussed in this section, there still some technique, such as shot noise, Transition Voltage Spectroscopy (TVS), thermoelectricity and so forth. Harvesting of the techniques helps for a better understanding of the molecular devices, and making contribute to application of the nano-sized electronics in the near future.

1.4.3 Experimental setup

1.4.3.1 MCBJ setup

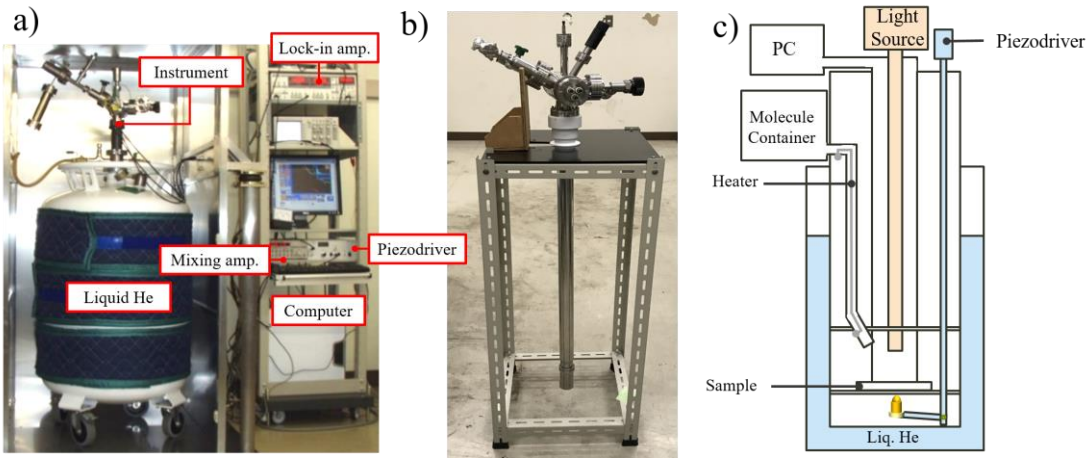

Figure 1.4.18 Illustrates of a) MCBJ measurement system in low temperature condition; b) image of the instrument; c) conception of instrument detail inside.

The experiments in this thesis were investigated in the ultra-high vacuum (UHV) condition with mechanically controllable break junction (MCBJs) technique at 10K, shown in Fig.1.4.18.

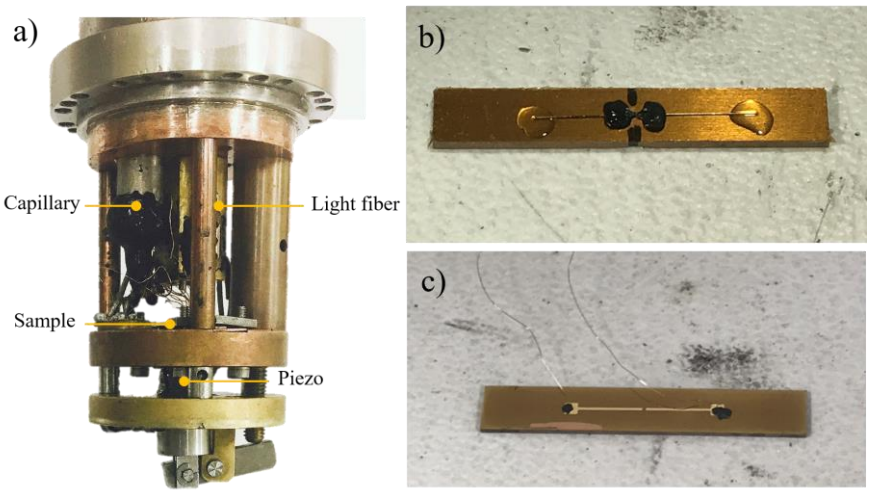

Figure 1.4.19 a) The image of the sample chamber; typical MCBJ samples used in this thesis b) notched type c) lithographic type.

In this thesis two types of substrates were utilized displayed in Fig. 1.4.19, which were notched type and lithography type. Both of the samples fabricated following the processes chapter 1.4.1.1. Briefly, the notched sample was prepared as following: a notched metal

wire (0.10 mm in diameter) was fixed on top of an electrically insulated phosphor bronze substrate with polyimide tape. On the other hand, the lithography substrate was prepared with a series of electron beam lithography (EBL) technique, shortly comment in section 1.4.1.1. Briefly, the phosphor bronze covered by an insulating polyimide layer, the metal electrodes fabricated by physical evaporate deposition (PVD) method.

The substrate was mounted in a three-point bending configuration in a custom-made vacuum pot. The metal wire was broken at the notched by bending of the substrate with piezo element. A single atomic contact could be formed just prior to the breaking of the wire. The target gases waere introduced onto the metal contacts through a capillary. Then, dc two-point voltage-biased conductance measurements were performed during the breaking process under an applied bias voltage of 100 mV. The differential conductance was measured using a standard lock-in technique with ac modulation at 1 mV and 7.777 kHz.

1.4.4 Critical effects on the electron transport in nano-size conductor

The molecular electronics to date has been progressed significantly either fabrication or characterization methods. However, the difference from realization to realization is still an issue. Thus, to clarify the effects on the nano-size electronics will help us to distinguish the reliability. In this section, we shall present some critical effects on the transport processes.

Structure effects

First of all, the structure of the molecules is the most critical one. The chemical structure, molecular length, orientation and so forth.

Table 3 Molecular structures and corresponding number [56]

Molecule number	Structure
1	
2	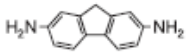
3	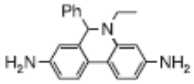
4	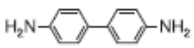
5	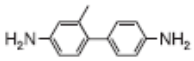
6	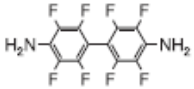
7	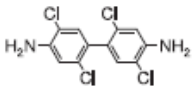
8	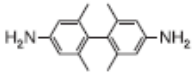
9	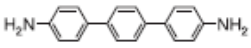

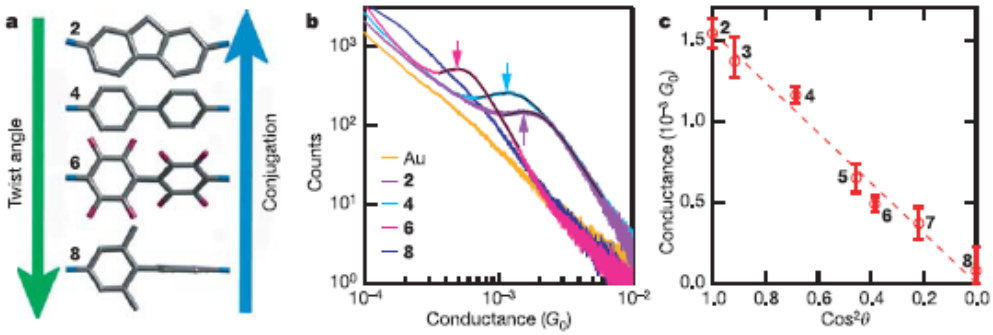

Figure 1.4.20 a) Structures of a subset of the biphenyl series studied, shown in order of increasing twist angle or decreasing conjugation. b) Conductance histograms obtained from measurements using molecule c, Position of the peaks for all the molecules studied plotted against $\cos^2\theta$, where θ, the calculated twist angle for each molecule [56].

Venkataraman *et al.* studied systemically 9 molecules, which contain similar structure with main body as a couple of benzene ring coupling with C-C σ bond (see as Table 3) and the end with –NH group to interact with the electrodes [56]. Their results demonstrated that the modifications have impact on the twist angle in the benzene-benzene body, in specific, the conductance minished as the function of twist angle increasing. It is considered as the benzene-benzene body twist, the π-conjugate felt a negative impact leading to a conductance shrink. The conductance behavior *vs* $\cos^2\theta$ exhibited a linearity, it was agree with the theoretical prediction.

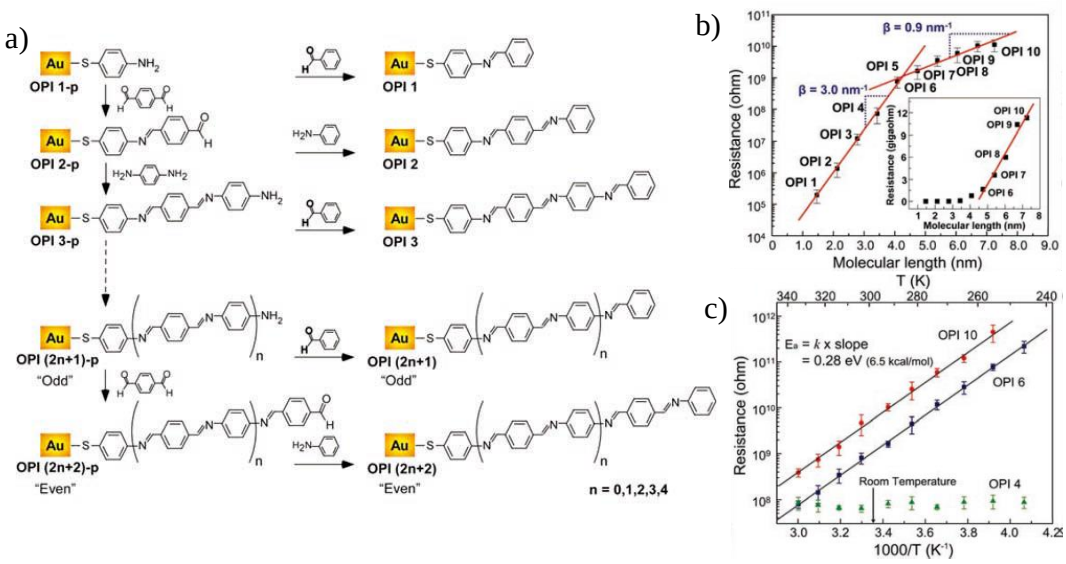

Figure 1.4.21 a) Measurements of the molecular wire resistance with CP-AFM. b) Molecular structure and synthetic route to OPI-p and OPI monolayers on the gold substrates. c) Semilog plots of *R* versus *L* for the gold/wire/gold junctions [57].

Another topic is the molecular length. Frisbie group provided a direct evidence in the relationship between the molecule length and the conductance [57]. As the Fig. 1.4.19 performed, they fabricated oligophenyleneimine (OPI) molecular junction with AFM technique. It demonstrated that near 4 nm in length even changed the transport mechanism from tunneling to hopping, as evidenced in the *I-V* curves by the striking change in temperature, length and electric field dependence [57].

Interactions in the interface

The interface means metal-molecular interface in this section. The interface problem including the anchoring group, adsorption site etc., which will change the interaction between the metal electrodes and molecules. Chen *et al*. compared –COOH, –SH, $–N_2H$ groups as anchoring group connected with the $–(CH_2)_n–$ and Au electrodes utilizing STM technique [58]. As shown in Fig. 1.4.20 shows the conductance varies in the order of Au-S > Au-NH_2 > Au-COOH. This results depended to different electronic coupling efficiencies provided by the different anchoring. They also gave the evidence for this experimental reality by *I-V* characterization. The binging strength changes in the order of Au-S > Au-NH_2 > Au-COOH make the conductance behavior reasonable [58].

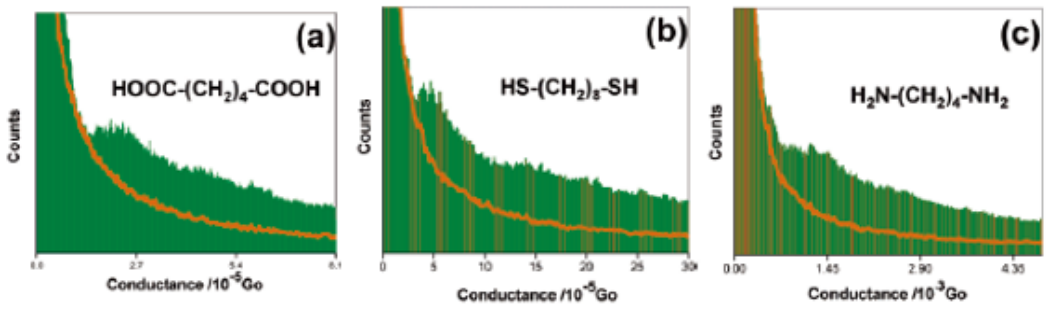

Figure 1.4.22 a) The histogram of dicarboxylic-acid butane shows a peak located at 2.7 x 10^{-4} G_0. b) The histogram of octanedithiol shows a peak located at 5.0 x 10^{-5} G_0. c) The histogram of diamine butane shows a peak at 1.45 x 10^{-3} G_0. The orange lines are the histograms of control experiments performed in the same solutions but containing no sample molecules [58].

Recently, Kaneko *et al*. reported a specific configuration results relied on MCBJ-SERS of the single molecule BDT junctions (Fig.1.4.21) [59]. Their *I-V* curves and SERS results were observed three most probable transport mode for BDT selectively interacted with Au in high (H), medium (M), and low (L) respectively. They gave the experimental evidence to demonstrate that even the same anchoring group adsorbed in different sites affected conduction behavior. With theoretical calculation they suggested the three most probable configurations, with absorption sites in bridge, hollow and top, attributed to high, middle and low three separated conduction states of the Au-BDT-Au molecular junction.

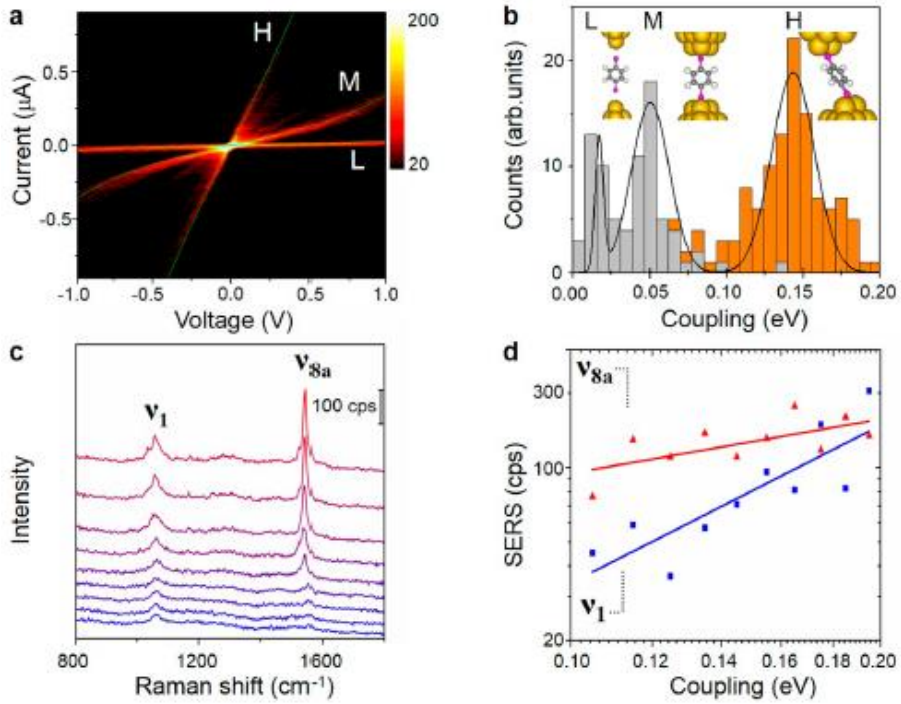

Figure 1.4.23 a) Bidimensional *I-V* histogram summarizing the *I-V* response of 203 single-molecule BDT junctions. The three most probable responses were fitted to a single-level tunneling transport model (green solid line). Coupling values (Γ) of 0.14, 0.052, and 0.014 eV were obtained for the high (H), medium (M), and low (L) profiles, respectively. b) Statistical distribution of Γ obtained from the individual fitting of 203 single molecule *I-V* responses and Gaussian fitting (black). Three most probable values are observed at 0.14 (H), 0.052 (M), and 0.014 eV (L), arising from bridge, hollow, and top molecular adsorption sites, respectively. Orange counts, centered on H, correspond to ν_8a-active samples featuring over 10 CPS. c) Single-molecule SERS spectra of BDT showing the intensity enhancement as a function of Γ. From bottom to top, Γ = 0.010, 0.019, 0.044, 0.073, 0.097, 0.12, 0.13, 0.13, and 0.17 *e*V. d) Correlation between the average intensity of the SERS signal as a function of Γ on a log−log plot. The plot includes averaged data from 96 ν_1-and ν_8-active samples. The solid line corresponds to the linear least-squares fitting [59].

Environmental effect

It is very easy to realize, once the molecular junction formed, it will be affected by not only the metallic, molecular internal elements but also the external stimulations, such as the solvent components, pH, impurities etc. Xiao *et al*. investigated the single-peptide molecular junction. They modified the peptide molecules with –SH group at the end, which has been reported has a strong interaction with Au electrodes [60]. They found the molecular conductance decreased as pH growing. It could be interpreted that according to the pH change the $–N_2H$, –COOH group of the peptide protonated or deprotonated, thus, the electrical structure and electron density in the junction.

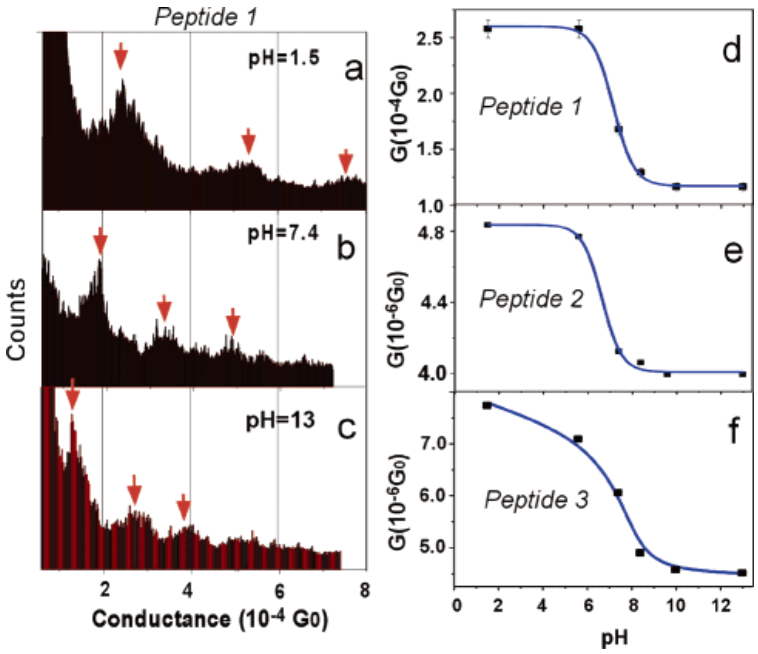

Figure 1.4.24 (a-c) Conductance histograms of Peptide 1 obtained at various solution pH. Conductance vs pH for Peptides 1 (d), 2 (e), and 3 (f). The solid lines are guide for the eye [60].

Except the effects were listed here, the other like hydrogen bond formation [61], electrostatic potential distribution [62], local heat conduction [63], etc. effects have been presented.

In a brief conclusion, the critical effects on the nano-size conductors, consequently, change the metal-molecule-metal nature of electrical structure, transmission inside the junctions. However, the higher accuracy mechanical technique and characterization methods will devote for the more reliable results and the application of the molecular devices.

Reference

1. Feynman, R. P., There's plenty of room at the bottom. *Engineering and science* **1960,** *23* (5), 22-36.
2. Moore, G. E., Cramming more components onto integrated circuits. *Proc. IEEE* **1998,** *86* (1), 82-85.
3. Aviram, A.; Ratner, M. A., Molecular rectifiers. *Chem. Phys. Lett.* **1974,** *29* (2), 277-283.
4. Chen, J.; Reed, M.; Dirk, S.; Price, D.; Rawlett, A.; Tour, J.; Grubisha, D.; Bennett, D., Molecular electronic devices. In *Molecular Electronics: Bio-sensors and Bio-computers*, Springer: 2003; pp 59-195.
5. Reed, M. A.; Zhou, C.; Muller, C.; Burgin, T.; Tour, J., Conductance of a molecular junction. *Science* **1997,** *278* (5336), 252-254.
6. Smit, R.; Noat, Y.; Untiedt, C.; Lang, N.; van Hemert, M. v.; Van Ruitenbeek, J., Measurement of the conductance of a hydrogen molecule. *Nature* **2002,** *419* (6910), 906-909.

7. Xu, B.; Tao, N. J., Measurement of single-molecule resistance by repeated formation of molecular junctions. *Science* **2003,** *301* (5637), 1221-1223.
8. Geddes, N.; Sambles, J.; Jarvis, D.; Parker, W.; Sandman, D., The electrical properties of metal-sandwiched Langmuir–Blodgett multilayers and monolayers of a redox-active organic molecular compound. *J. Appl. Phys.* **1992,** *71* (2), 756-768.
9. Metzger, R. M., Unimolecular electronics. *Chem. Rev.* **2015,** *115* (11), 5056-5115.
10. Fu, L.; Liu, Z.; Liu, Y.; Han, B.; Hu, P.; Cao, L.; Zhu, D., Beaded cobalt oxide nanoparticles along carbon nanotubes: towards more highly integrated electronic devices. *Adv. Mater.***2005,** *17* (2), 217-221.
11. Zhao, J.; Zeng, C.; Cheng, X.; Wang, K.; Wang, G.; Yang, J.; Hou, J. G.; Zhu, Q., Single C59N molecule as a molecular rectifier. *Phys Rev Lett* **2005,** *95* (4), 045502.
12. Metzger, R. M., Unimolecular electronics. *Chem. Rev.* **2015,** *115* (11), 5056-115.
13. Ohnishi, H.; Kondo, Y.; Takayanagi, K., Quantized conductance through individual rows of suspended gold atoms. *Nature* **1998,** *395* (6704), 780-783.
14. (a) Ellenbogen, J. C.; Love, J. C., Architectures for molecular electronic computers. I. Logic structures and an adder designed from molecular electronic diodes. *Proc. IEEE* **2000,** *88* (3), 386-426; (b) Carroll, R. L.; Gorman, C. B., The genesis of molecular electronics. *Angew. Chem. Int. Ed.* **2002,** *41* (23), 4378-4400.
15. Tour, J. M., Molecular electronics. Synthesis and testing of components. *Acc. Chem. Res.* **2000,** *33* (11), 791-804.
16. Terao, J.; Homma, K.; Konoshima, Y.; Imoto, R.; Masai, H.; Matsuda, W.; Seki, S.; Fujihara, T.; Tsuji, Y., Synthesis of functionalized insulated molecular wires by polymerization of an insulated π-conjugated monomer. *Chem. Commun.* **2014,** *50* (6), 658-660.
17. Terao, J.; Wadahama, A.; Matono, A.; Tada, T.; Watanabe, S.; Seki, S.; Fujihara, T.; Tsuji, Y., Design principle for increasing charge mobility of π-conjugated polymers using regularly localized molecular orbitals. *Nat. Commun.***2013,** *4*, 1691.
18. (a) Aich, P.; Labiuk, S. L.; Tari, L. W.; Delbaere, L. J.; Roesler, W. J.; Falk, K. J.; Steer, R. P.; Lee, J. S., M-DNA: a complex between divalent metal ions and DNA which behaves as a molecular wire. *J. Mol. Biol.***1999,** *294* (2), 477-485; (b) Qian, J.; Liu, L.; Xu, B.; Tian, W., A theoretical study on the charge transport properties of DNA. *Organic Electronics* **2017,** *42*, 244-255.
19. Tans, S. J.; Devoret, M. H.; Dai, H.; Thess, A.; Smalley, R. E.; Geerligs, L.; Dekker, C., Individual single-wall carbon nanotubes as quantum wires. *Nature* **1997,** *386* (6624), 474-477.
20. Whalley, A. C.; Steigerwald, M. L.; Guo, X.; Nuckolls, C., Reversible switching in molecular electronic devices. *J. Am. Chem. Soc.* **2007,** *129* (42), 12590-12591.
21. Jia, C.; Migliore, A.; Xin, N.; Huang, S.; Wang, J.; Yang, Q.; Wang, S.; Chen, H.; Wang, D.; Feng, B., Covalently bonded single-molecule junctions with stable and reversible photoswitched conductivity. *Science* **2016,** *352* (6292), 1443-1445.
22. Gittins, D. I.; Bethell, D.; Schiffrin, D. J.; Nichols, R. J., A nanometre-scale electronic switch consisting of a metal cluster and redox-addressable groups. *Nature* **2000,** *408* (6808), 67-69.
23. Collier, C. P.; Mattersteig, G.; Wong, E. W.; Luo, Y.; Beverly, K.; Sampaio, J.; Raymo, F. M.; Stoddart, J. F.; Heath, J. R., A [2] catenane-based solid state electronically reconfigurable switch. *Science* **2000,** *289* (5482), 1172-1175.

24. Green, J. E.; Choi, J. W.; Boukai, A.; Bunimovich, Y.; Johnston-Halperin, E.; DeIonno, E.; Luo, Y.; Sheriff, B. A.; Xu, K.; Shin, Y. S.; Tseng, H. R.; Stoddart, J. F.; Heath, J. R., A 160-kilobit molecular electronic memory patterned at 10(11) bits per square centimetre. *Nature* **2007,** *445* (7126), 414-7.
25. LOS ANGELES, C., Assembling Nanocircuits From the Bottom Up.
26. Lörtscher, E.; Ciszek, J. W.; Tour, J.; Riel, H., Reversible and Controllable Switching of a Single-Molecule Junction. *Small* **2006,** *2* (8-9), 973-977.
27. Devoret, M. H.; Schoelkopf, R. J., Amplifying quantum signals with the single-electron transistor. *Nature* **2000,** *406* (6799), 1039-1046.
28. Park, H.; Park, J.; Lim, A. K.; Anderson, E. H.; Alivisatos, A. P.; McEuen, P. L., Nanomechanical oscillations in a single-C60 transistor. *Nature* **2000,** *407* (6800), 57-60.
29. Guo, X.; Gorodetsky, A. A.; Hone, J.; Barton, J. K.; Nuckolls, C., Conductivity of a single DNA duplex bridging a carbon nanotube gap. *Nat. Nanotechol.* **2008,** *3* (3), 163-167.
30. Guo, X.; Small, J. P.; Klare, J. E.; Wang, Y.; Purewal, M. S.; Tam, I. W.; Hong, B. H.; Caldwell, R.; Huang, L.; O'brien, S., Covalently bridging gaps in single-walled carbon nanotubes with conducting molecules. *Science* **2006,** *311* (5759), 356-359.
31. He, G.; Li, J.; Ci, H.; Qi, C.; Guo, X., Direct Measurement of Single-Molecule DNA Hybridization Dynamics with Single-Base Resolution. *Angew. Chem. Int. Ed.* **2016,** *55* (31), 9036-9040.
32. Xiang, D.; Jeong, H.; Kim, D.; Lee, T.; Cheng, Y.; Wang, Q.; Mayer, D., Three-terminal single-molecule junctions formed by mechanically controllable break junctions with side gating. *Nano Lett.* **2013,** *13* (6), 2809-2813.
33. (a) Büttiker, M., Scattering theory of current and intensity noise correlations in conductors and wave guides. *Phys. Rev. B* **1992,** *46* (19), 12485; (b) Scheer, E., *Molecular electronics: an introduction to theory and experiment*. World Scientific: 2010; Vol. 1; (c) Landauer, R., Spatial variation of currents and fields due to localized scatterers in metallic conduction. *IBM Journal of Research and Development* **1957,** *1* (3), 223-231.
34. Agraıt, N.; Yeyati, A. L.; Van Ruitenbeek, J. M., Quantum properties of atomic-sized conductors. *Phys. Rep.* **2003,** *377* (2), 81-279.
35. Kittel, C., *Introduction to solid state physics*. Wiley: **2005**.
36. Xiang, D.; Wang, X.; Jia, C.; Lee, T.; Guo, X., Molecular-scale electronics: from concept to function. *Chem. Rev* **2016,** *116* (7), 4318-4440.
37. Krans, J.; Muller, C.; Yanson, I.; Govaert, T. C.; Hesper, R.; Van Ruitenbeek, J., One-atom point contacts. *Phys. Rev. B* **1993,** *48* (19), 14721.
38. Untiedt, C.; Yanson, A.; Grande, R.; Rubio-Bollinger, G.; Agraït, N.; Vieira, S.; Van Ruitenbeek, J., Calibration of the length of a chain of single gold atoms. *Phys. Rev. B* **2002,** *66* (8), 085418.
39. Martin, C. A.; Ding, D.; van der Zant, H. S.; van Ruitenbeek, J. M., Lithographic mechanical break junctions for single-molecule measurements in vacuum: possibilities and limitations. *New J. Phys.***2008,** *10* (6), 065008.
40. (a) Nakazumi, T.; Kiguchi, M., Formation of Co atomic wire in hydrogen atmosphere. *J. Phys. Chem. Lett.* **2010,** *1* (6), 923-926; (b) Kiguchi, M.; Hashimoto, K.; Ono, Y.; Taketsugu, T.; Murakoshi, K., Formation of a Pd atomic chain in a hydrogen atmosphere. *Phys. Rev. B* **2010,** *81* (19), 195401; (c) Thijssen, W.; Marjenburgh, D.; Bremmer, R.; Van Ruitenbeek, J.,

Oxygen-enhanced atomic chain formation. *Phys. Rev. Lett.* **2006,** *96* (2), 026806; (d) Nascimento, A.; San-Miguel, M. A.; Da Silva, E., Unveiling the origin of oxygen atomic impurities in Au nanowires. *Phys. Rev. B* **2014,** *89* (8), 085417; (e) Kiguchi, M.; Konishi, T.; Murakoshi, K., Hydrogen-assisted stabilization of Ni nanowires in solution. *Appl. Phys. Lett.***2005,** *87* (4), 043104; (f) Kiguchi, M.; Murakoshi, K., Fabrication of stable Pd nanowire assisted by hydrogen in solution. *Appl. Phys. Lett.***2006,** *88* (25), 253112.

41. Binnig, G.; Rohrer, H.; Gerber, C.; Weibel, E., Surface studies by scanning tunneling microscopy. *Phys. Rev. Lett.* **1982,** *49* (1), 57.

42. Binnig, G.; Rohrer, H., In touch with atoms. *Rev. Mod. Phys.***1999,** *71* (2), S324.

43. Binnig, G.; Rohrer, H.; Gerber, C.; Weibel, E., 7 × 7 Reconstruction on Si(111) Resolved in Real Space. *Phys. Rev. Lett.* **1983,** *50* (2), 120-123.

44. (a) Nishino, T.; Shiigi, H.; Kiguchi, M.; Nagaoka, T., Specific single-molecule detection of glucose in a supramolecularly designed tunnel junction. *Chem. Commun.* **2017,** *53* (37), 5212-5215; (b) Fujii, S.; Kanae, S.; Iwane, M.; Nishino, T.; Osuga, T.; Murase, T.; Fujita, M.; Kiguchi, M., Effect of Ag Ion Insertion on Electron Transport through Au Ion Wires. *Chem. Lett.* **2016,** *45* (7), 764-766; (c) Bui, P. T.; Nishino, T.; Shiigi, H.; Nagaoka, T., One-by-one single-molecule detection of mutated nucleobases by monitoring tunneling current using a DNA tip. *Chem. Commun.* **2015,** *51* (9), 1666-1669.

45. Trenkler, T.; Hantschel, T.; Stephenson, R.; De Wolf, P.; Vandervorst, W.; Hellemans, L.; Malavé, A.; Büchel, D.; Oesterschulze, E.; Kulisch, W., Evaluating probes for "electrical" atomic force microscopy. *Journal of Vacuum Science & Technology B: Microelectronics and Nanometer Structures Processing, Measurement, and Phenomena* **2000,** *18* (1), 418-427.

46. Rubio, G.; Agrait, N.; Vieira, S., Atomic-sized metallic contacts: mechanical properties and electronic transport. *Phys. Rev. Lett.* **1996,** *76* (13), 2302.

47. Chae, D.-H.; Berry, J. F.; Jung, S.; Cotton, F. A.; Murillo, C. A.; Yao, Z., Vibrational excitations in single trimetal-molecule transistors. *Nano Lett.* **2006,** *6* (2), 165-168.

48. Yanson, A.; Bollinger, G. R.; Van den Brom, H.; Agrait, N.; Van Ruitenbeek, J., Formation and manipulation of a metallic wire of single gold atoms. *Nature* **1998,** *395* (6704), 783-785.

49. Cuevas, J.; Yeyati, A. L.; Mart ń-Rodero, A.; Bollinger, G. R.; Untiedt, C.; Agra ť, N., Evolution of conducting channels in metallic atomic contacts under elastic deformation. *Phys. Rev. Lett.* **1998,** *81* (14), 2990.

50. Stipe, B.; Rezaei, M.; Ho, W., Single-molecule vibrational spectroscopy and microscopy. *Science* **1998,** *280* (5370), 1732-1735.

51. Deng, M.; Ye, G.; Cai, S.; Sun, G.; Jiang, J., Probing flexible conformations in molecular junctions by inelastic electron tunneling spectroscopy. *AIP Advances* **2015,** *5* (1), 017144.

52. Song, H.; Reed, M. A.; Lee, T., Single molecule electronic devices. *Adv. Mater.* **2011,** *23* (14), 1583-1608.

53. Tsutsui, M.; Taniguchi, M., Vibrational spectroscopy of single-molecule junctions by direct current measurements. *J. Appl. Phys.* **2013,** *113* (8), 084301.

54. Tian, J.-H.; Liu, B.; Li, X.; Yang, Z.-L.; Ren, B.; Wu, S.-T.; Tao, N.; Tian, Z.-Q., Study of molecular junctions with a combined surface-enhanced Raman and mechanically controllable break junction method. *J. Am. Chem. Soc.* **2006,** *128* (46), 14748-14749.

55. Konishi, T.; Kiguchi, M.; Takase, M.; Nagasawa, F.; Nabika, H.; Ikeda, K.; Uosaki, K.; Ueno, K.; Misawa, H.; Murakoshi, K., Single molecule dynamics at a mechanically

controllable break junction in solution at room temperature. *J. Am. Chem. Soc.* **2012,** *135* (3), 1009-1014.
56. Venkataraman, L.; Klare, J. E.; Nuckolls, C.; Hybertsen, M. S.; Steigerwald, M. L., Dependence of single-molecule junction conductance on molecular conformation. *Nature* **2006,** *442* (7105), 904-907.
57. Choi, S. H.; Kim, B.; Frisbie, C. D., Electrical resistance of long conjugated molecular wires. *Science* **2008,** *320* (5882), 1482-1486.
58. Chen, F.; Li, X.; Hihath, J.; Huang, Z.; Tao, N., Effect of anchoring groups on single-molecule conductance: comparative study of thiol-, amine-, and carboxylic-acid-terminated molecules. *J. Am. Chem. Soc.* **2006,** *128* (49), 15874-15881.
59. Kaneko, S.; Murai, D.; Marques-Gonzalez, S.; Nakamura, H.; Komoto, Y.; Fujii, S.; Nishino, T.; Ikeda, K.; Tsukagoshi, K.; Kiguchi, M., Site-Selection in Single-Molecule Junction for Highly Reproducible Molecular Electronics. *J Am Chem Soc* **2016,** *138* (4), 1294-300.
60. Xiao, X.; Xu, B.; Tao, N., Conductance titration of single-peptide molecules. *J. Am. Chem. Soc.* **2004,** *126* (17), 5370-5371.
61. Chang, S.; He, J.; Kibel, A.; Lee, M.; Sankey, O.; Zhang, P.; Lindsay, S., Tunnelling readout of hydrogen-bonding-based recognition. *Nat. Nanotechol.* **2009,** *4* (5), 297-301.
62. Nitzan, A.; Galperin, M.; Ingold, G.-L.; Grabert, H., On the electrostatic potential profile in biased molecular wires. *J. Chem. Phys.***2002,** *117* (23), 10837-10841.
63. (a) Segal, D.; Nitzan, A., Heating in current carrying molecular junctions. *J. Chem. Phys.* **2002,** *117* (8), 3915-3927; (b) Komoto, Y.; Isshiki, Y.; Fujii, S.; Nishino, T.; Kiguchi, M., Evaluation of the Electronic Structure of Single-Molecule Junctions Based on Current–Voltage and Thermopower Measurements: Application to C60 Single-Molecule Junction. *Chemistry–An Asian Journal* **2017,** *12* (4), 440-445.

Chapter 2

Photochemistry involving metal nanoparticles

2.1 Photochemical reactions with metal material

The interplay of light with matter has long been, and will continue to be, fascinating to the scientific community. Besides, metals can be utilized as catalysts for a wide range of chemical reactions. Two advantages make contributions to the photochemistry on the metal surface. One is expected as the new reaction channels might become possible by electronic excitation, which are conventionally forbidden by thermal activation. On the other hand, the interactions of molecules with solid metal surface open a new and unique pathways of the photoexcitation and reaction in inhomogeneous reactions. Thus, the past few decades have been risen interests of photon-driven process with the metal materials participation, for instance, the adsorption of the adsorbents on the metal surfaces, the bond formation or break at the interface. Since the first time, Fujishima and Honda found the experimental evidences to approve the n-type TiO_2 electrodes can decompose the water employing UV irradiation in early of 1970s' [1]. Generations of scientists started to contribute to the photochemistry, aiming to deal with the energy, pollute etc. issues emerged in the expansion process of the human being to the environment.

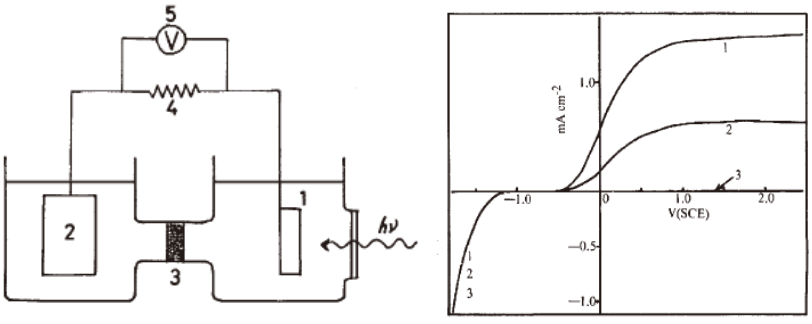

Figure 2.1.1 Schematic of the electrochemical cell in which the TiO2 electrodes is connected with platinum electrode (left). Current-voltage curves for n-type TiO2 semiconductor (right) [1].

Literally, the critical factors for the photochemical reaction are main separated in two. One is the light source and the other is the matter you want to choose. In terms of the light source, the important orientation is saving energy, and every researcher try their best to satisfy this goal. When it comes to light itself, it is described as an electromagnetic plane wave with magnetic field vectors perpendicular and orthogonal electric to the propagation direction in classic electrodynamics. Three sides are usually concern of light source, the energy $\varepsilon = h\nu$, where h is Plank's constant and frequency v=c/λ; the intensity

$$I_t/I_0 = \exp(-\alpha_0 CL) \qquad \text{Eq. 35}$$

where the I_0 and I_t are the intensities before and after transmitting through medium, C is

the concentration of absorbing matters in moles/volume, L is the sample thickness passed by the light. α_0 is the optical coefficient in area/mol. The last factor is polarization. Ultraviolet (UV) photons (a few eV) are commonly picked up not only because that the intense source are available in the laboratorial environment but diversities of molecular systems have electronic transitions particularly the lowest energy ones, in this region. To date, two kinds of UV light sources are commonly employed in the surface photochemical studies, continuous wave (CW) light source providing low-power wide tunable UV light and pulsed lasers [2].

The other important factor to photochemical reaction on the metal system goes to the metal surface. A diversity of researches have been undertaken of the photochemistry on the metal surface in the near decades past. At the pretty beginning, the photochemical reactions were able to be constructed on the metallic bulk surface.

Thus, with appropriate light importing, the photochemical reaction on the metal surface is possible to emerge. For the early stage photochemical studies, two general mechanisms involved in photochemical reactions: phonon-driven and charge-carrier-driven have been discussed for decades [3] , shown in Fig. 2.1.2.

Phonon-driven process

This process derives from the excitation of the phonon mode of nanoparticles, which coupled with the reaction coordinate. The coupling leads in the evolution for the adsorbate from the reactant to product on the ground-state potential energy surface (PES, Fig.2.1.2a). The phonon-driven process conventionally calls for relatively high temperature, besides, the products with ground-state free-energy landscape is also needed. Majorities of cases, with assumption of phonon temperatures of the nanoparticles and reactant are in an equilibrium, these reactions can be stimulated adequately by employing the classical transition state theory.

Charge-carrier-driven process

An external stimulus is usual used in the charge- carrier-driven process, to excite charge carriers (electron or hole) on the metal surface. Briefly, the energized charge carriers populate the electronic state transiently, centered on the adsorbate molecule to form transient ions. Furthermore, the adsorbate moves to a different PES and be forced. The forces induced the nuclear motion of adsorbate atoms, which can attribute to the activation of the chemical bond and transformations. The critical factor of this process is a coupling between excited electronic and vibrational state of the nanoparticle-adsorbate complex. Additionally, the charge carrier energy is converted into kinetic complex energy along the reaction coordinate. This mechanisim has its own name: desorption (reaction) induced by electronic transitions (DIET).

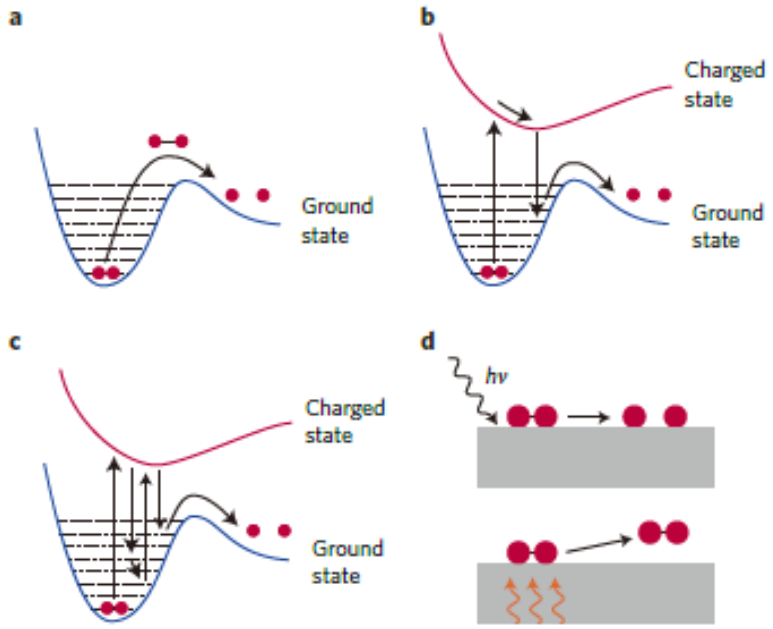

Figure 2.1.2 Mechanisms of phonon- and electron-driven reactions on metals [3].

However, with the deepening of the research, more than 20 years ago, the material scientists have already realized the metallic materials' showing size dependencies in their own physical and chemical properties [4-5]. Fortunately, with the development of the nanotechnology currently, the chemical reactions today can be considered in varieties of metal materials, including light-driven ones. The researches about the nanoparticles increase gradually (characteristic lengths of less than 50 nm) because they can active photochemical reactions on their surface with lower light intensities and can be triggered by both of the mechanism described previously [6-7]. Particularly, stemming from the development of the quantum theories, the nano-scale reactions exploit nano metarials, as usually refers to nanoparticles (NPs), e.g. nano balls, nano cubes, nanopores, nanoshells and so forth has been brought to the public view. The unique physical properties including geometries for lower fraction reflected light, strong localized surface plasmon resonance (LSPR) and high surface electronic density of the metal nanoparticles make them different from the bulk system. The nano-scaled world is fascinating and manifold, and still so many issue are waited for being solved. The geometric and electronic problem have been discussed abundantly in either macro- or microscopic. Thus, we shall present the nano scale metal surface only, the plasmon resonance, and its dedication in photochemical reaction.

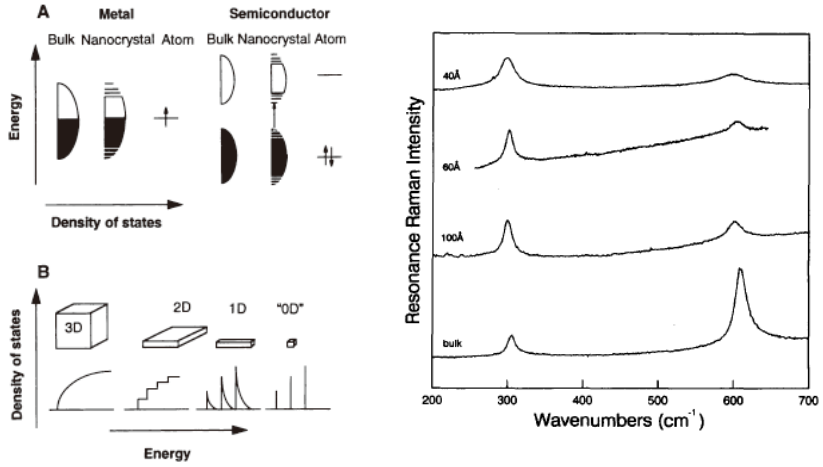

Figure 2.1.2 Schematic illustration of the density of state and bond structure in different sizes of metal and semiconductor clusters (left). Resonance Raman spectra of CdS clusters, scaled to illustrate the size dependence of the ratio of fundamental to overtones (right) [5].

2.2 Plasmon enhanced chemical reactions

2.2.1 Plasmon resonance

Surface plasmon are known as the coherent oscillations of conduction electrons located in the skin layer of metal, capable of concentrating light into subwavelength nano structures resulting in electromagnetic field enhancement factors exceed ~1000 [8]. The achievements in the surface plasmon today, should credit to the precise fabrication technique, advanced characterization technique and supporting, the current compute calculation method establishment. The surface resonance can be classified as propagating plasmon and localized surface plasmon (LSPRs), as shown in Fig.2.2.1 [9].

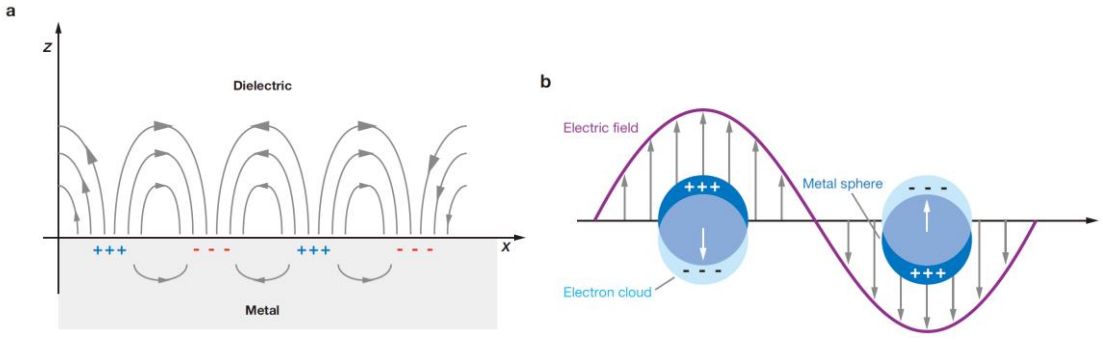

Figure 2.2.1 Schematic diagrams illustrating a) a surface plasmon polarition (or propagating plasmon), b) a localized surface plasmon [9].

While many field are well investigated, the development of new techniques and conception continues to open new terrain. With the sophisticated and manipulation of metallic nanostructures fabrication techniques, new applications benefited from the LSPRs

begin to have its moment. A more intuitive illustration for the localized surface plasmon resonance, a well-known case originating from LSPRs is the gorgeous color of the noble metal nanoparticles. Fig.2.2.2 present available metallic structures for plasmon excitation (except bulk) [10]. The LSPR properties depend on several indexes, including the shape, size, composition, structure and environment of the metal nanoctrystals [11-12]. In the case of the non-isolated, like NP pair, ditch and periodic structure etc. more complicated structures, the interaction between the nano structures also contribute to the surface plasmon resonance. Fuller summarized initial reports of the two sphere plasmon resonance systems [13]. In his perspective, the gap size, orientian etc have impact on the surface plasmon resonance.

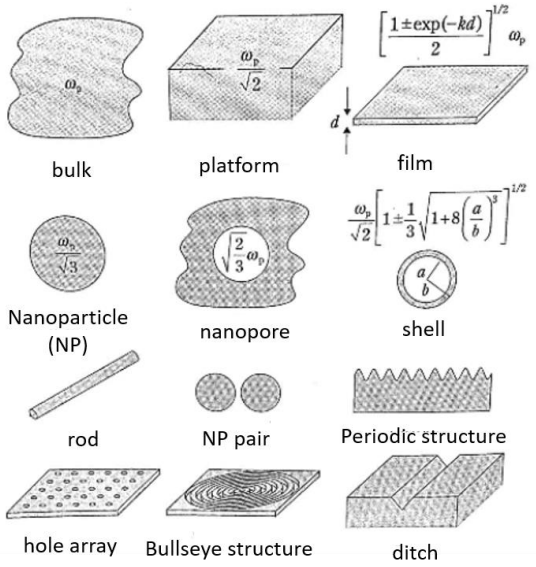

Figure 2.2.2 Available metallic structures for plasmon excitation (except bulk) [10].

2.2.2 Brief theory of LSPR

A full theoretical treatment of LSPRs is quite lengthy. In this section, we shall refer a compact treatment. Consider a spherical nanoparticle of radius *a*, which is irradiated by *z*-polarized incident light of wavelength λ. Here, assume that $a \ll \lambda$. As the Fig.2.2.1b display, the magnitude of the electrical field appears static around the NPs. The quasi-static approximation employed to solve the Maxwell's equation [14]. The solution gives the EM field outside the particles as

$$E_{out}(x,y,z) = E_0\hat{\boldsymbol{z}} - [\frac{\varepsilon_{in}-\varepsilon_{out}}{(\varepsilon_{in}+2\varepsilon_{out})}]a^3E_0[\frac{\hat{\boldsymbol{z}}}{r^3} - \frac{3z}{r^5}(x\hat{\boldsymbol{x}} + y\hat{\boldsymbol{y}} + z\hat{\boldsymbol{z}})] \qquad \text{Eq.36}$$

Here, ε_{in} and ε_{out} are the dielectric constant of the metal NPs and external environment, respectively. The dielectric of the metal NPs is strongly dependent on wavelength, thus, the first square brackets determines the dielectric resonance condition for the particle. When the $\varepsilon_{in} + 2\varepsilon_{out}$ equals to 0, the EM field is enhanced relatie to the incident field. In determining the EM field outside the metal material, the *a* and ε_{out} play key roles consistent with experimental realizations.

Furthermore, we derivate the extinction spectrum of the metal sphere as

$$E(\lambda) = \frac{24\pi^2 N a^3 \varepsilon_{out}^{3/2}}{\lambda \ln(10)} \left[\frac{\varepsilon_i(\lambda)}{\varepsilon_r(\lambda) + \chi \varepsilon_{out}^2 + \varepsilon_i(\lambda)^2}\right] \quad \text{Eq.37}$$

Here, ε_r and ε_i are the real and imaginary part of the metal dielectric function, respectively. Again, the wavelength is dependent on the metal dielectric function. The factor χ relies on the geometric consideration, 2 for the sphere while 20 for the particle with high aspect ratios. In this equation, the interest represented as *N* finite polarizable elements, any of which can interplay with the applied electric field [9]. With prosper approximation method, the treatment is able to give the extinction of particles of arbitrary shape and size, and good agreement with experiments [9].

2.2.3 Plasmon enhanced chemical reactions

Metal nanocrystals have been found to play critical roles in an amount of chemical reactions. The mechanisms of the plasmon enhanced chemical reaction are divided in three, plasmonic enhancenment of light adsorption (Fig.2.2.4a), plasmonic sensitization (Fig.2.2.4b) and pure-metal plasmonic phtocatalysis (Fig.2.2.4c).

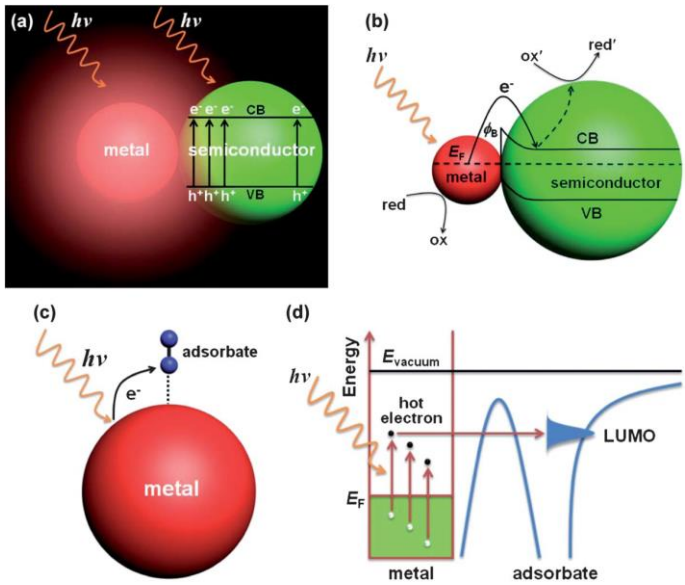

Figure 2.2.4 Schematic illustrating the three functional mechanisms of plasmons in chemical reactions. (a) Plasmonic enhancement of light absorption. (b) Plasmonic sensitization. (c and d) Pure-metal plasmonic photocatalysis. VB and CB represent the valence band and the conduction band of the semiconductor, respectively. E_F is the Fermi level at equilibrium. red and ox stand for the reduced and oxidized forms of the redox species, respectively. E_{vcuum} is the vacuum energy level [15].

The semiconductors are widely involving in the plasmonic enhanced reactions due to their adsorption spectrally overlapping with the plasmon resonance of metal nanostructures. They will participate the plasmonic enhancement of light adsorption and plasmonic

Plasmonic enhancement of light adsorption

The incident light irradiates the LSPRs in the electron-hole pair in the semiconductor and metal nanocraystals, simultaneously. Within the 10-50 nm space, the formation rate of

electron-hole pairs feel the LSPRs then can be enhanced [16]. The plasmonic nano metals plays a light energy processor, concentrated the incident photon energy in LSPRs and transferred to the adjacent optical species via near field interaction, resulted in a light absorption enhancement.

Plasmonic sensitization

As Fig.2.2.4b presents, the plasmonic sensitization occurs at the interface between a wide-band-gap semiconductor and an intimately integrated plasmonic nano metals. When the semiconductor contact with the noble metal, the conduction band will downward bend due to the thermal equilibration of the Fermi level. Thus, Schottky barrier forms and block the electron transfer from the metal to the semiconductor. However, with the LSPR, a proportion of energetic electron, which possesses higher energy than the barrier, generated to cross the barrier.

Pure-metal plasmonic photocatalysis

Without the semiconductor, the nano pure metals also provide possibilities as a catalysts for the chemical reactions. As Fig. 2.2.4c, d show, two mechanisms, plasmonic heating and hot electron transfer, resembling in the 2.1 section. The former one is through the photothermal conversion of plasmonic nano metals. As a consequence, the LSPRs decays through electron-phonon relaxation and subsequent thermalization of lattice phonons (Fig2.2.4c). The hot electron process is a photoinduced electron transfer process, which is similar to plasmonic sensitization. The hot electrons in this process generated by plasmon irradiation inject into the available molecular orbital, conventionally the LUMO, to form transition anions (Fig.2.2.4d).

Many experimental evidences are already reported induced by the LSPR. Thomann *et al*. demonstrated nano metallic plasmonic resonances and multilayer interference impacts can be engineered to strongly concentrate sunlight close to the electrode/liq. Interface, precisely where the relevant reactions occur [17]. In their system, semiconductor powers in various shapes and sizes re dispersed in a water cell. Upon excitation with photons with a larger energy than the band gap of the semiconductor, resulting in success of the water splitting irradiated by solar light.

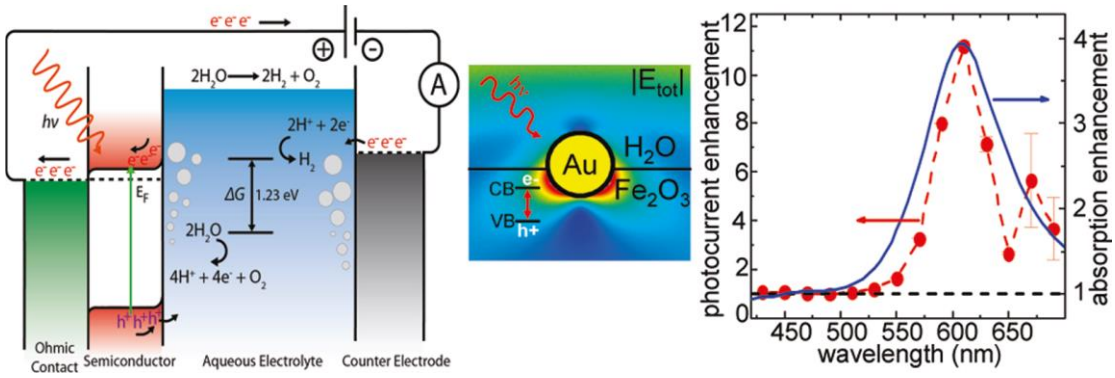

Figure 2.2.5 Schematic band diagram depicting the semiconductor absorber (left) in contact with the liquid, where the photo generated holes drive oxygen evolution [17].

A two photon adsorption reaction has been reported by Misawa group (Fig.2.2.6) [18].Their work reveals that TPA can be induced under exposure to an incoherent radiation

continuous-wave, involving a two-photon sensitivity of photopolymers has already been employed the near-field imaging of nanoparticles plasmon modes under laser irradiation.

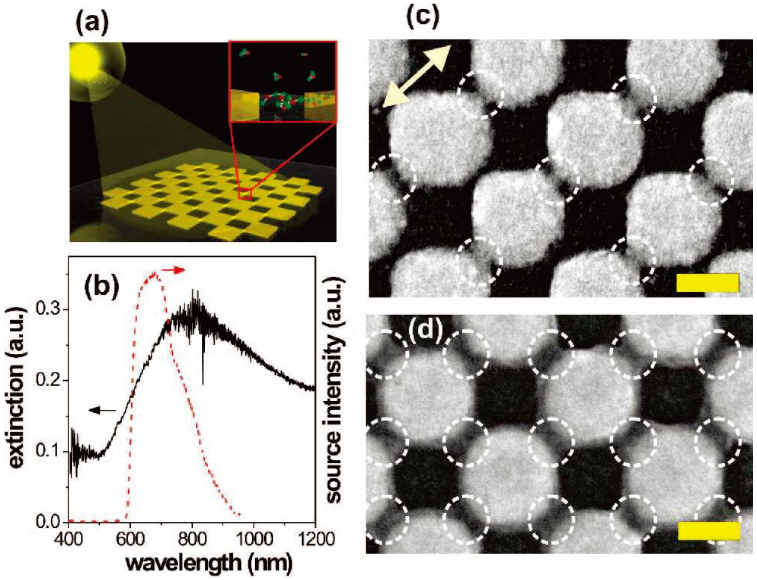

Figure 2.2.6 a) Schematic of the checkerboard pattern of nanoblocks separated by nanogaps; the nanoblocks are coated by a thin film of photoresist SU-8 and exposed to radiation from an incoherent source; the inset illustrates polymerization of SU-8 in the intense near-field existing in the nanogap. b) Optical extinction spectrum of the checkerboard pattern and the spectrum of the incoherent source. c) SEM image of the structure after 3 h exposure to the incoherent source polarized linearly along the direction indicated by the arrow. Panel d) is the same as c), after exposure by unpolarized source. The polymerized regions are emphasized by dashed circles. The scale bar length is 100 nm [18].

Even the molecular electronics, Selzer group have investigated the Au-2,7-diaminofluorene (DAF)-Au system with laser irradiation enhance reaction [19]. The Fig.2.2.7 present their experimental realization. The conductance traces reveal the enhancement of the conductance in the nano junction stemmed from the plasmon resonance. Due to their results employed a pulse laser irradiation, which offer a possibility to create rapid transient plasmons, opening a path to optical ultrafast gating of the molecular devices.

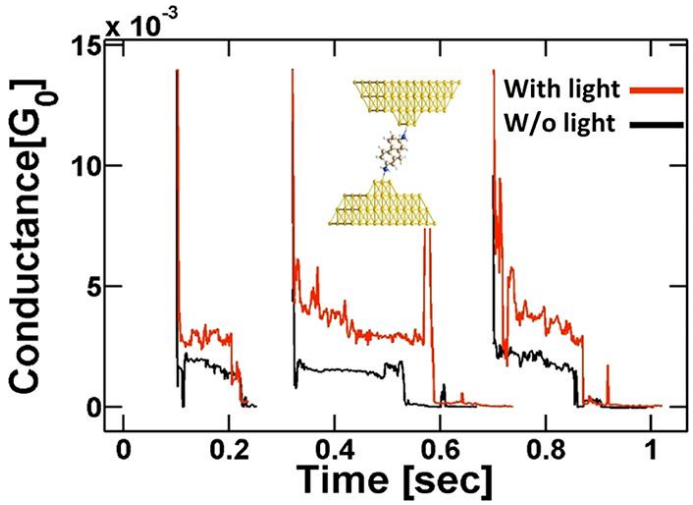

Figure 2.2.7 Schematic band diagram depicting the semiconductor absorber (left) in contact with the liquid, where the photo generated holes drive oxygen evolution [19].

2.3 Water participated photon driven reactions on the metal surface

Water covers about seven of tenth area the earth's surface. The abundant storage of water has given rise to the investigation for the applications of the water participating processes. On the other hand, conversion of the significant reserving solar energy into chemical energy is also considered as a subject of intense studies for many years. Thus, diversities of the photon-driven water relative reactions has big interests in many years.

Since Fujishima and Honda firstly reported the generation of H_2 and O_2 with TiO_2 illuminated with near ultraviolet light [1]. The TiO_2 system has been contributed to the water attendance reaction in multiples diversities photon-driven systems [15,20]. However, the reaction efficiency driven by TiO_2 only is limited. Varieties of co-catalysts have been developed. Metallic nano structure has been added into the list due to its surface plasmon resonance could enhance the efficiency of reaction. Ingram and Linic reported the visible light photocatalytic activity ascribed to the electron transfer from Ag nanoparticles to N-TiO_2 [21]. Their results demonstrated the Ag particles physically mixed with the N-doped TiO_2 can increase the evolution of the hydrogen and oxygen by ~10 fold of the Au presented system derived from the plasmonic sensitization mechanism of the Ag/N-TiO_2 system [22].

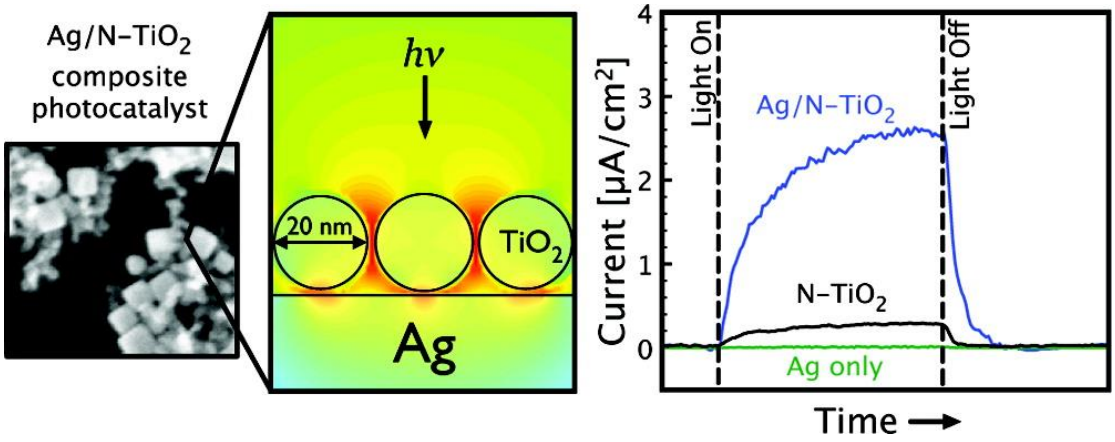

Figure 2.3.1 Schematic diagrams illustrating the Ag/N-TiO_2 system (left), photocurrent responses (per macroscopic electrode area) upon illumination with a broadband visible light source (400-900 nm) (right) [21].

The plasmon resonance could benefit for the reaction, plenty of efforts concentrated on the related structure. Mubeen *et al.* fabricated an autonomous, fault-tolerant and easy-toimplement photosysthetic device Au nanorod-based plasmonic solar water splitting system with a good stability, shown as Fig. 2.3.2 [23]. Their system worked within the hot-electron tunneling process, produced an over 1,000-fold enhancement in the

conductance on illumination by 600 nm light. Unfortunately, their system still rely on some complicated fabrication.

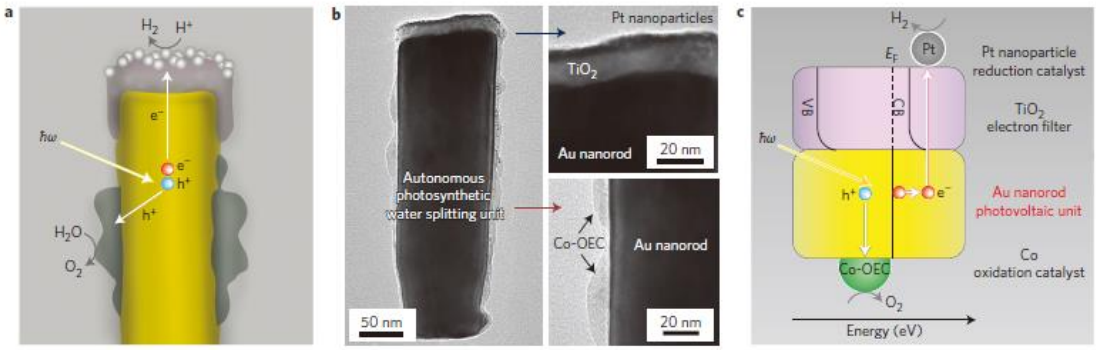

Figure 2.3.2 Structure and mechanism of operation of the autonomous plasmonic solar water splitter. a) Schematic of the cross-section of an individual photosynthetic unit showing the inner gold nanorod, the TiO_2 cap decorated with platinum nanoparticles, which functions as the hydrogen evolution catalyst, and the Co-OEC material deposited on the lower portion of the gold nanorod, b) Corresponding transmission electron micrograph (left) and magnified views of the platinum/TiO_2 cap (top right) and the Co-OEC (bottom right), c) Energy level diagram superimposed on a schematic of an individual unit of the plasmonic solar water splitter, showing the proposed processes occurring in its various parts and in energy space. CB, conduction band; VB, valence band; E_F, Fermi energy.

The semiconductor involving water reactors are efficient and stability, however, considered of fabrication difficulty and the economic cost with these systems. With the similar plasmonic mechanisms, the metal was also considered for the water relative reactions. The Cu surface was reported as a promising catalyst at elevated temperature [24]. Andersson *et al*. investigated a water dissociation reaction on Cu (110) at near ambient condition. Fig.2.3.3. displays, the increase temperature promoting the reaction.

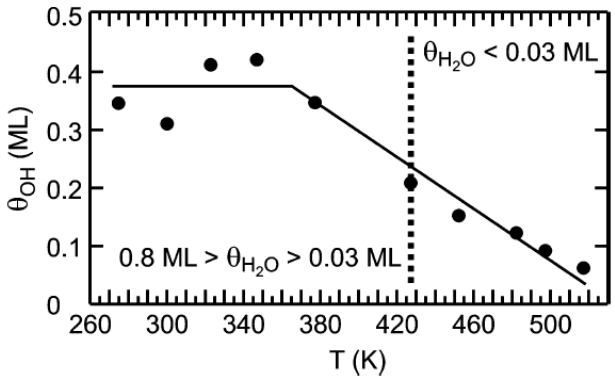

Figure 2.3.3 Total OH coverage (θ_{OH}) as a function of temperature on Cu- (110). The solid line is shown to emphasize the trend for the observed OH coverage changes. The vertical dashed line marks the highest temperature (428 K) at which molecular water can still be observed by XPS (g0.03 ML) [24].

Torimoto *et al*. constructed a hybrid composed of two core–shell nanostructures (CdS@SiO‖Au@SiO2), as shown in Fig. 2.3.4 [25]. Their study revealed the special role of LSPR induced electric field in enhancing photocatalysis.

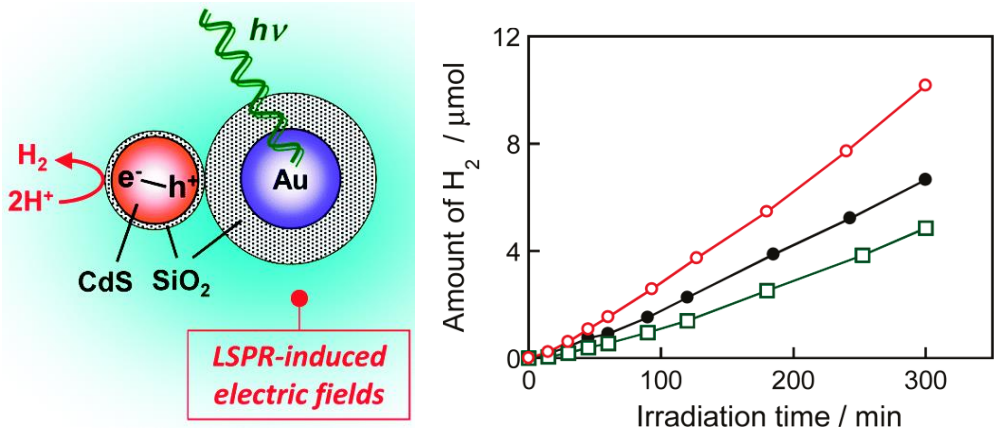

Figure 2.3.4 Schematic illustration of the immobilization of CdS@SiO_2 on Au@SiO_2 particles system (left), Time courses of hydrogen evolution by photocatalysts of CdS@SiO2 (solid circles) and CdS@SiO_2//Au@SiO_2 particles with SiO_2 layer thicknesses of 17 nm (open circles) and 2.8 nm (open squares) on Au cores. The experiments were performed by irradiation light from a 300-W Xe lamp ($\lambda > 350$ nm). [25].

The wide investigated systems for the water participant reactions are diversities. However, due to the power consumption of the electricity and heat and the fabrication cost of the complicated reactor systems, take advantage of the photon driven water relevant reactions in industrial application still long way to go.

2.4 Purpose of this study

The chemical reactions on surfaces have attracted wide attention (eg. Catalytic reaction, electrochemical reaction). One of the hot topics in surface chemical reaction is the photo-driven H_2O related reactions, which can produce hydrogen molecule with high energy. The photo-driven H_2O splitting reactions was first discussed on semiconductor surface. For enhance the efficiency, metal nano particles are utilized as photo antenna. In specifically, the localized surface plasmon (LSP) excitation in the metal nano particle produce hot electrons, which can inject the conduction band in semiconductor, leading to oxidation of water molecule. The LSPS in metal nano structure has attracted attention as a trigger of chemical reaction, because various interesting reaction such as hydrogen dissociation, two photon polymerization reaction proceeds via LSP excitation. Here, we focus on the water decomposition reaction on metal atomic junction. It is because LSP is effectively excited in metal atomic junction by irradiation of light. Second, the metal atomic junction is highly reactive material. For example, hydrogen dissociation reaction can proceed on the Au atomic junction, while this reaction does not proceed on flat Au surface. Thus, the photo-driven H_2O related reactions is more likely to proceed on metal atomic junction than the surface. Despite these interest, there are no studies of the photo-driven H_2O relevant reactions even photochemical reaction on metal atomic junction. In addition, the interaction of H_2O (reactant), H_2, O_2 (products) and metal atomic junction is not well understood. So, in this thesis, the photo-driven H_2O decompose reactions on metal atomic junction has been studied, through the fundamental studies of pure H_2, O_2, H_2O/Au, Ag, and Cu junction.

First of all, the stable and reliable system fabricated to obtain the electron transport properties and the structural information of the molecules relevant to the water decompose reaction. In the chapter 3, 4, 5, 6, I fabricated the metallic atomic contacts and single molecular junction with mechanical controllable break junction (MCBJ) technique. With comprehensively analysis of the conductance traces and histogram, inelastic electron tunneling spectrum (IETS), the electron transport properties of the reactant molecule H_2O, the product molecules H_2, O_2 single molecular junctions will be discussed. Besides, with the length histogram and current-voltage characterization (*I-V* curves) measurement, the structural information were performed. Consider the electric and geometric characteristics, the Cu/H_2O system was chosen for the further investigate.

Rely on prior works, the water resolve reaction has been investigation with Cu nanoelectrodes with irradiation, in chapter 7. The reaction would be evaluated based on the conductance and vibrational behavior in the nano junction. The IETS employed to give the experimental evidences to the reaction processes with comparing the vibrational mode variation of the nano contact system. The results presented in this thesis reveal that the water decomposition reaction can be excited in the Cu nano contacts. With analysis of the wavelength dependence the mechanism will be presented.

The *in-situ* reaction monitoring method utilizing the MCBJ and IETS would benefit for more molecular reactions information, the sensitivity of the IETS would be powerful evaluation method for diversities of systems. In addition, the Cu nano electrode has a similar surface plasmon behavior with Au, however, compare to the gold, copper is much cheaper and has potential for commercialization in the application. The most importance in present work, the water decomposition reaction executed in a molecular level, make contribution to the molecular devices versatility.

Reference

1. Fujishima, A., Electrochemical photolysis of water at a semiconductor electrode. *Nature* **1972,** *238*, 37-38.
2. Zhou, X.-L.; Zhu, X.-Y.; White, J., Photochemistry at adsorbate/metal interfaces. *Surf. Sci. Rep.* **1991,** *13* (3-6), 73-220.
3. Linic, S.; Aslam, U.; Boerigter, C.; Morabito, M., Photochemical transformations on plasmonic metal nanoparticles. *Nat. Mater.* **2015,** *14* (6), 567-576.
4. Alivisatos, A. P., Semiconductor clusters, nanocrystals, and quantum dots. *Science* **1996,** *271* (5251), 933.
5. Shiang, J.; Goldstein, A.; Alivisatos, A., Lattice reorganization in electronically excited semiconductor clusters. *J. Chem. Phys.***1990,** *92* (5), 3232-3233.
6. (a) Mukherjee, S.; Libisch, F.; Large, N.; Neumann, O.; Brown, L. V.; Cheng, J.; Lassiter, J. B.; Carter, E. A.; Nordlander, P.; Halas, N. J., Hot electrons do the impossible: plasmon-induced dissociation of H2 on Au. *Nano Lett* **2013,** *13* (1), 240-247; (b) Zheng, Z.; Tachikawa, T.; Majima, T., Single-particle study of Pt-modified Au nanorods for plasmon-enhanced hydrogen generation in visible to near-infrared region. *J. Am. Chem. Soc.*

2014, *136* (19), 6870-6873.
7. Christopher, P.; Xin, H.; Marimuthu, A.; Linic, S., Singular characteristics and unique chemical bond activation mechanisms of photocatalytic reactions on plasmonic nanostructures. *Nat. Mater.* **2012,** *11* (12), 1044-1050.
8. Schuck, P.; Fromm, D.; Sundaramurthy, A.; Kino, G.; Moerner, W., Improving the mismatch between light and nanoscale objects with gold bowtie nanoantennas. *Phys. Rev. Lett.* **2005,** *94* (1), 017402.
9. Willets, K. A.; Van Duyne, R. P., Localized surface plasmon resonance spectroscopy and sensing. *Annu Rev Phys Chem* **2007,** *58*, 267-97.
10. 岡本隆之; 梶川浩太郎, *プラズモニクス 基礎と応用*. *プラズモニクス 基礎と応用* **2010**.
11. Huang, X.; Neretina, S.; El-Sayed, M. A., Gold nanorods: from synthesis and properties to biological and biomedical applications. *Adv. Mater.***2009,** *21* (48), 4880-4910.
12. Sau, T. K.; Rogach, A. L., Nonspherical noble metal nanoparticles: colloid-chemical synthesis and morphology control. *Adv. Mater.***2010,** *22* (16), 1781-1804.
13. Fuller, K. A., Optical resonances and two-sphere systems. *Appl. Opt.* **1991,** *30* (33), 4716-4731.
14. Kelly, K. L.; Coronado, E.; Zhao, L. L.; Schatz, G. C., The optical properties of metal nanoparticles: the influence of size, shape, and dielectric environment. ACS Publications: **2003**.
15. Xiao, M.; Jiang, R.; Wang, F.; Fang, C.; Wang, J.; Yu, J. C., Plasmon-enhanced chemical reactions. *J. Mater. Chem. A* **2013,** *1* (19), 5790.
16. Ming, T.; Chen, H.; Jiang, R.; Li, Q.; Wang, J., Plasmon-controlled fluorescence: beyond the intensity enhancement. *J. Phys. Chem. Lett.* **2012,** *3* (2), 191-202.
17. Thomann, I.; Pinaud, B. A.; Chen, Z.; Clemens, B. M.; Jaramillo, T. F.; Brongersma, M. L., Plasmon enhanced solar-to-fuel energy conversion. *Nano Lett.* **2011,** *11* (8), 3440-3446.
18. Ueno, K.; Juodkazis, S.; Shibuya, T.; Yokota, Y.; Mizeikis, V.; Sasaki, K.; Misawa, H., Nanoparticle plasmon-assisted two-photon polymerization induced by incoherent excitation source. *J. Am. Chem. Soc.* **2008,** *130* (22), 6928-6929.
19. Vadai, M.; Nachman, N.; Ben-Zion, M.; Bürkle, M.; Pauly, F.; Cuevas, J. C.; Selzer, Y., Plasmon-Induced Conductance Enhancement in Single-Molecule Junctions. *J. Phys. Chem. Lett.* **2013,** *4* (17), 2811-2816.
20. Zoulias, E.; Varkaraki, E.; Lymberopoulos, N.; Christodoulou, C. N.; Karagiorgis, G. N., A review on water electrolysis. *TCJST* **2004,** *4* (2), 41-71.
21. Ingram, D. B.; Linic, S., Water splitting on composite plasmonic-metal/semiconductor photoelectrodes: evidence for selective plasmon-induced formation of charge carriers near the semiconductor surface. *J. Am. Chem. Soc.* **2011,** *133* (14), 5202-5205.
22. Gomes Silva, C. u.; Juárez, R.; Marino, T.; Molinari, R.; García, H., Influence of excitation wavelength (UV or visible light) on the photocatalytic activity of titania containing gold nanoparticles for the generation of hydrogen or oxygen from water. *J. Am. Chem. Soc.* **2010,** *133* (3), 595-602.
23. Mubeen, S.; Lee, J.; Singh, N.; Krämer, S.; Stucky, G. D.; Moskovits, M., An autonomous photosynthetic device in which all charge carriers derive from surface plasmons. *Nat. Nanotechol.* **2013,** *8* (4), 247-251.

24. Andersson, K.; Ketteler, G.; Bluhm, H.; Yamamoto, S.; Ogasawara, H.; Pettersson, L. G.; Salmeron, M.; Nilsson, A., Autocatalytic water dissociation on Cu (110) at near ambient conditions. *J. Am. Chem. Soc.* **2008,** *130* (9), 2793-2797.
25. Torimoto, T.; Horibe, H.; Kameyama, T.; Okazaki, K.-i.; Ikeda, S.; Matsumura, M.; Ishikawa, A.; Ishihara, H., Plasmon-enhanced photocatalytic activity of cadmium sulfide nanoparticle immobilized on silica-coated gold particles. *J. Phys. Chem. Lett.* **2011,** *2* (16), 2057-2062.

Chapter 3

Electrical conductance and structure of copper atomic junctions in the presence of water molecules

3.1 Introduction

Nanoscale electronic devices in which a single atom, atomic chain or molecule is suspended between metal electrodes have been extensively studied both experimentally and theoretically due to their fundamental interest and potential application in nanoelectronics [1]. The aim is to miniaturize electronic devices by using a single molecule as an active electronic component[2–4]. The electronic properties of these nanostructures depend strongly on the atomic species involved and the contact geometries. In order to study the nature of atomic and molecular contacts and to advance in our understanding of atomic scale quantum transport, there have been numerous studies regarding single-molecule junctions using mechanically controllable break junctions (MCBJs) and scanning tunnelling microscopy (STM). Transistor, diode, and switching behaviors have been reported in recent years for single-molecule junctions [5–9]. However, it is still challenging to determine the detailed atomic structures of the single-molecule junctions, including the metal–molecule contact configuration and the structure of the metal electrode near the contact [10-11]. These difficulties arise from the technical limitations regarding the characterization of single-molecule junctions using spectroscopic techniques.

Single-molecule junctions with simple and small molecules are the systems best suited for the investigation of the junction atomic structure, enabling the study of the relationship between the physical properties (e.g. conductance) and the atomic structures, because various advanced techniques can be applied to them. The Pt/H_2 junction has been the most extensively studied system of this kind [12–15]. It was revealed that a single hydrogen molecule forms a bridge between Pt electrodes with its molecular long axis parallel to the junction axis, and its conductance is 1 G_0 ($2e^2/h$). The length analysis revealed that the single Pt/H_2 junction can be stretched over 0.5 nm, forming an atomic chain. The formation of an atomic chain indicates that the single-molecule junction is highly stable in the presence of H_2 molecules. The stabilization of nano-junctions in the presence of molecules has also been reported for other systems, namely: Co, Ni, Pd/H_2 and Ag/O_2 junctions [16–21].

Single-molecule junctions of uncomplicated homonuclear diatomic molecules are becoming increasingly well understood. The next logic step is the study of small heteronuclear molecules. Here we focus on H_2O molecules. The H_2O molecule, while still

being a relatively small molecule, plays an important role in many fields, such as catalysis, corrosion, electrolysis, photosynthesis, and in hydrogen fuel cells. To the best of our knowledge, H_2O single-molecule junctions have been studied only for Pt electrodes [22]. Tal *et al*. reported the crossover between the enhancement and the reduction of the conductance due to the electron-vibration interaction by measuring the Pt/H_2O junction using point contact spectroscopy (PCS) and inelastic tunneling spectroscopy (IETS) at 4 K [22]. However, in their work the conductance histogram did not present a clear peak, and the atomic structure of the Pt/H_2O junction remains unclear. The fabrication of single-molecule junctions with a fixed conductance value is of outmost importance for developing reliable single-molecule electronic devices. One of the possible reasons for the absence of a well-defined Pt/H_2O junction is a strong molecule–metal interaction. Various atomic configurations are possible for single-molecule junctions with strong molecule–metal interaction, leading to various conductance values. We have already reported that a moderate molecule–metal interaction is necessary to obtain single-molecule junctions with reproducible conductance values [23].

In the present chapter, we investigated the less reactive Cu. While Cu/H_2O junctions have not been studied previously, the Cu/H_2O system is of great relevance due to the catalytic role of Cu in the water–gas-shift reaction, hydrolysis reaction, and other useful catalytic reactions [24]. The dissociation reaction and proton relay reaction were reported on Cu(110) surfaces studied using STM and first-principles calculations [25-26]. The dissociation reaction has been reported on Cu nano-particles and Cu single crystal surfaces at elevated temperature (>600 K) [27-29]. The H_2O dissociation does not proceed at low temperature [30].

Here we report experimental and theoretical studies of Cu/H_2O junctions. The experimental results obtained using MCBJ at 10K reveal the formation of Cu/H_2O junctions with a stable conductance value of around 0.1 G_0. The length analysis of the conductance-distance traces showed the formation of the atomic or molecular chain. Theoretical studies reveal that stretching of the Cu junction in the presence of H_2O results in the formation of a continuous Cu atomic chain bridging the junction with a H_2O molecule adsorbed to a bridging Cu atom. Prior to the formation of the chain the calculated conductance of the junction initially decreases gradually and then, as the chain begins to form, it drops abruptly to near 0.1 G_0. This behavior closely resembles that experimentally observed for the Cu/H_2O junction. We therefore propose that the observed 0.1 G_0 conductance feature is due to the formation of a Cu atomic chain with an adsorbed H_2O molecule that backscatters electrons travelling along the chain, reducing the observed conductance of the Cu/H_2O chain to 0.1 G_0.

3.2 Experimental

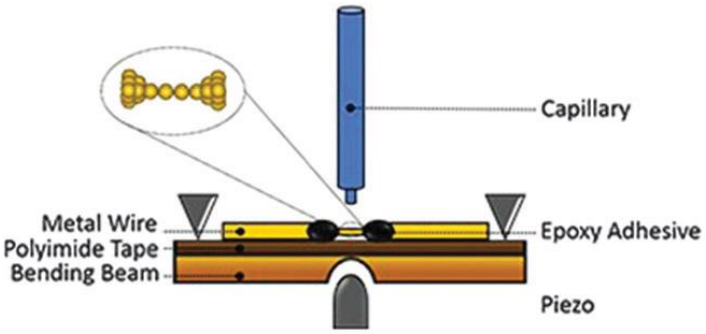

Figure 3.1 Schematic image of the MCBJ setup.

Experiments were performed using a MCBJ technique at about 10 K in an ultrahigh vacuum (UHV) as in our previously reported study (Fig.3.1) [16]. A notched Cu wire (0.10 mm in diameter) was glued on the top of a phosphor bronze substrate covered with a polyimide tape. The substrate was mounted in a three-point bending configuration inside a custom-made vacuum chamber. After the chamber was evacuated, it was cooled down in a dewar filled with liquid helium. The notched part of the Cu wire was repeatedly broken by bending the substrate using piezocontrolled elements. Ultra-pure H_2O was placed in a glass container and it was purified by repeated cycles of freezing, pumping, and thawing. The H_2O molecules were introduced into the junction through a heated capillary during the breaking process. The DC two-point voltage-biased conductance measurements were performed by applying a bias voltage of 100 mV. The experiments were performed on 8 independent samples with Cu electrodes.

3.3 Results and discussion

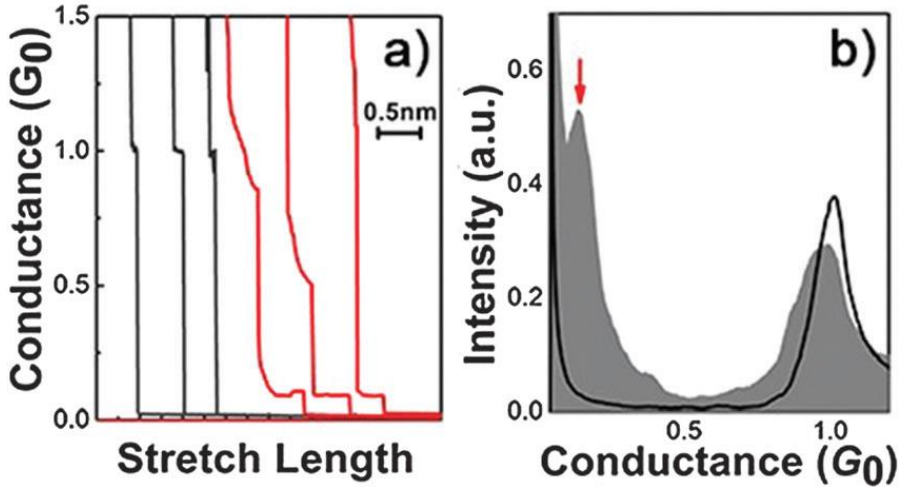

Figure 3.2 a) Typical conductance traces for Cu contacts before (black) and after (red) the introduction of H_2O. b) Conductance histograms for Cu contacts before (black solid line) and after the introduction of H_2O (grey). The number of conductance traces was 1024 (before introduction of water) and 1078 (after introduction of water). The histograms were normalized to the number of traces. The bin size is 0.004 G_0.

Fig. 3.2a shows typical conductance traces obtained during the junction breaking process before and after the introduction of H_2O. The stretch length is defined as the displacement between the glued stems of the Cu electrodes. Before the introduction of H_2O, conductance plateaus appeared at ca. 1 G_0, corresponding to the Cu atomic contact [3]. The length of the 1 G_0 plateau (~0.1 nm) was found to be shorter than the Cu–Cu interatomic distance (0.3 nm). This result confirms the previously reported inability of Cu to form atomic chains [31-32]. After the introduction of H_2O, additional conductance plateaus appeared at around 0.1 G_0. It is noted that this 0.1 G_0 plateau could be extended over 0.3 nm. Since the Cu–Cu distance is 0.26 nm for bulk Cu, the present results indicate the formation of the atomic or molecular chain. Fig. 3.2b shows the conductance histogram constructed from more than 1000 conductance traces. The conductance histograms were normalized to the number of conductance traces. Before the introduction of H_2O, a prominent peak appeared at 1 G_0, corresponding to a single Cu atomic contact. After the introduction of H_2O, an additional peak appeared at ca. 0.1 G_0. Since the conductance of the contact depends on its atomic configuration, the appearance of this new peak indicates the formation of an atomic-scale contact with a well-defined atomic configuration. In addition, the 1 G_0 peak shifted to slightly lower conductance values compared to that of clean Cu contacts.

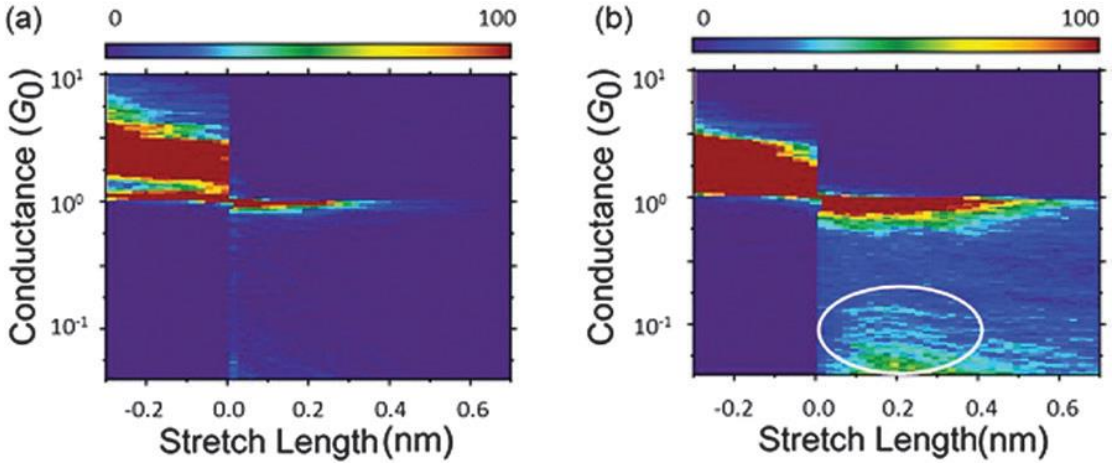

Figure 3.3 The 2D conductance histograms for Cu contacts before a) and after b) the introduction of H_2O. The histograms were constructed from 2020 (before introduction of H_2O) and 3179 traces (after introduction of H_2O).

Fig. 3.3 shows the two-dimensional conductance histograms constructed from more than two thousand conductance traces for Cu contacts before and after the introduction of H_2O. These histograms were constructed by taking the first data point with a value of conductance lower than 1.2 G_0 as a relative zero distance z = 0, for each individual trace. Large counts were observed at around 1 G_0 for both cases. After the introduction of H_2O, a surge in the number of counts was observed in the 0.1 G_0 region. The plateau in the 0.1 G_0

region extended to about 0.3 nm, which is consistent with the previously discussed conductance trace (Fig. 3.2a)).

In order to evaluate the stability of the observed atomic chain at 0.1 G_0, the length of the conductance plateau was investigated for more than 2000 conductance traces (Fig.3.4). The plateau length was defined as the distance between the points at which the conductance dropped below 0.4 G_0 and 0.04 G_0. Before the exposition to H_2O, the contacts broke within 0.2 nm, with an average plateau length of 0.05 ± 0.01 nm. After the introduction of H_2O, the contact was extended over 0.5 nm with an increased average plateau length of 0.27 ± 0.01 nm. These results quantitatively indicate the formation of the atomic or molecular chain.

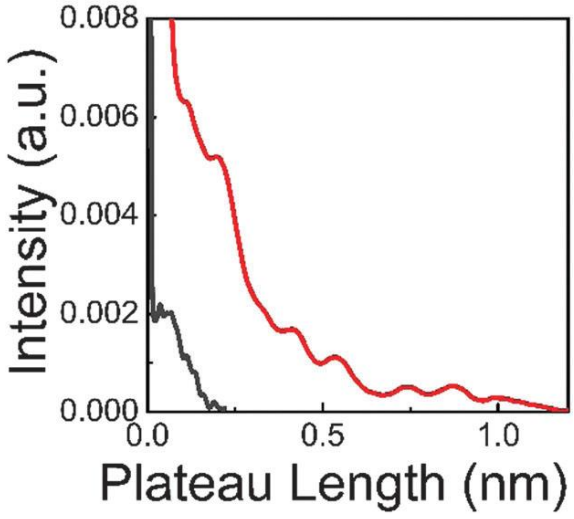

Figure 3.4 The plateau length histogram for the Cu junction in the low conductance regime (0.4–0.04 G_0) before (black) and after (red) the introduction of H_2O. The histograms were constructed from 2020 (before introduction of H_2O) and 3179 traces (after introduction of H_2O). The histograms were normalized to the number of traces. The bin size is 0.0012 nm.

Here, we comment on the possibility of the dissociation of the H_2O molecule on Cu atomic contacts. As previously discussed in the introduction part of this section, the dissociation of H_2O on the surface of Cu occurs at elevated temperatures. The reactivity of a metal increases with a decrease in the coordination number. However, we consider that H_2O does not dissociate under the present experimental conditions. Upon dissociation of H_2O on the surface of the Cu atomic contact, hydrogen and oxygen are present in the vicinity of the contact. The conductance response of the Cu atomic contact in the presence of hydrogen has been studied at low temperatures (10 K). The conductance histogram shows a peak at 0.3 G_0 [33]. While our experimental findings are explained very well by the mechanism described above, we cannot completely rule out the possibility of an alternate mechanism in which copper oxide resulting from a chemical reaction between copper and water plays a role.

3.4 Theoretical calculation

These experimental findings are explained below with the help of our *ab initio* calculations [34] of the low energy geometries of atomic junctions consisting of two

copper clusters in the presence of water molecules, a semi-empirical extended Hückel model of quantum chemistry [1, 35] for the electronic structure that includes electrostatic potentials obtained from density functional theory (DFT), and Landauer theory-based transport calculations [1].

Experimentally, a single metal atom or atomic chain is formed by stretching a metallic junction close to its rupture point [36–38]. In order to simulate the stretching of the Cu junctions in our experiments, we carried out *ab initio* calculations to study the evolution of the structure as the junction was elongated by increasing the distance between the outer ends of two Cu clusters that were initially in direct contact with each other. Optimization of the stretched structures, formed from this fully relaxed initial structure, was carried out by systematically moving the leftmost and the rightmost Cu atoms further apart, freezing them and relaxing the positions of all the other atoms. We repeated this to obtain junction geometries with different distances between the outermost Cu atoms. All of the relaxations were carried out using the GAUSSIAN'09 package and the minimum energy configurations of the systems were found at the PBE1PBE functional and Lanl2DZ pseudopotential and basis set level [34-35, 39].

Since the behavior of the electrical conductance, *G*, for atomic and molecular junctions under tensile stress can give a quantitative understanding of the system and clarify whether or not the junction breaks, we use the Landauer formula Eq.3.1

$$G(E_F) = G_0 \sum_{\alpha,\beta} |t_{\alpha\beta}(E_F)|^2 \frac{v_\alpha}{v_\beta} \qquad \text{Eq. 3.1}$$

to calculate the zero bias conductance at the Fermi energy, E_F. Here $t_{\alpha\beta}$ is the electron transmission amplitude through the junction, β is the electronic state of a carrier that is coming from the left lead, and α is the electronic state of a carrier that is transmitted to the right lead. v_α and v_β are the velocities of the carriers in the right and left leads at the Fermi level.

As in previous work [10-11, 38, 40-51], we couple the outer parts of the two copper clusters to a large number of semi-infinite quasi-one-dimensional ideal leads that represent the macroscopic electron source and drain in the transport measurements. The transmission amplitudes $t_{\alpha\beta}$ are found by solving the Lippmann-Schwinger equation

$$|\psi^i\rangle = |\phi_0^i\rangle + g_0(E_F) W |\psi^i\rangle \qquad \text{Eq. 3.2}$$

where $|\phi_0^i\rangle$ is an electron eigenstate of the i^{th} ideal semi-infinite one-dimensional left lead that is decoupled from the "extended molecule" that consists of the two copper clusters and the water molecule, $g_0(E_F)$ is the Green's function of the decoupled system of the ideal leads and the extended molecule, W is the coupling between the extended molecule and the ideal leads, and $|\psi^i\rangle$ is the scattering eigenstate of the complete coupled system associated with the incident electron state $|\phi_0^i\rangle$. The semi-empirical extended Hückel model [1] with the parameters of Ammeter *et al.* [35] which we have improved [43-45] by inclusion of atomic electrostatic potentials obtained from DFT calculations for each extended molecular structure was used to evaluate the Hamiltonian matrix elements and the atomic valence orbital overlaps that enter the Green's function in Eq. (3.2). Note that this methodology

involves no fitting to any experimental data relating to transport in molecular junctions, as has been discussed in Refs. 1, 41 and 42. It is known to yield low bias conductances in reasonably good agreement with experiments on gold atomic junctions and for a variety of molecules bridging gold electrodes [1, 10-11, 41-42, 52-55] as well as molecules with silicon and tungsten electrodes [43-45].

Some of the calculated geometries of our model Cu junction with an adsorbed H_2O molecule under tensile stress are shown in Fig. 3.5. In the present model, two 10 atom Cu clusters are initially bonded to each other with a H_2O molecule adsorbed to one of the clusters as the starting optimized geometry, as shown in Fig.3.5a. We find that stretching of the junction resulted in gradual deformation of its structure, punctuated by successive Cu–Cu bond breaking events. Representative calculated geometries at different stages of the stretching process are shown in Fig. 3.5b–e.

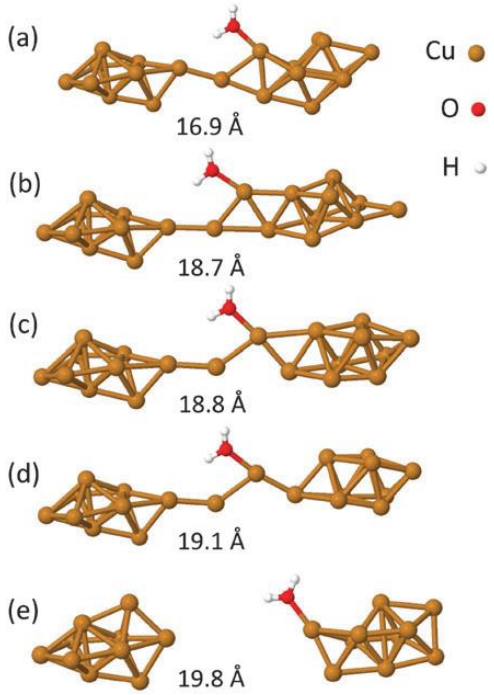

Figure 3.5 Relaxed structures of a Cu junction with an adsorbed H_2O molecule for various distances between the outermost atoms of the Cu clusters. As the junction is stretched starting from structure a), Cu–Cu bonds break in succession and a Cu atomic chain with an adsorbed H_2Omolecule forms, as in b)–d). Upon further stretching, the Cu chain breaks, as in e).

The behavior shown in Fig. 3.5 differs qualitatively from that of Pt junctions stretched in the presence of H_2 molecules [12-15] and of Au junctions stretched in the presence of alkanedithiolate (ADT) molecules [1]. Specifically after the metal point contact in a stretched Pt/H_2 or Au/ADT junction has ruptured, a molecule is often suspended between the two electrodes. In contrast, when the Cu/H_2O junction is stretched, our calculations (see Fig.3. 6) do not exhibit evidence of a H_2O molecule bridging the Cu electrodes after the Cu chain between the Cu clusters has ruptured. Instead, our results indicate that the observed decrease in conductance is due to the bonding between a H_2O molecule and the metallic atomic chain bridging the two Cu electrodes, as shown in Fig. 3.5d. When the Cu

atomic chain breaks, the H_2O molecule does not bridge the junction but bonds to only one of the Cu electrodes, as shown in Fig. 3.5e.

Based on the formalism outlined above, the calculated conductance for each relaxed structure versus the junction length *d* is plotted in Fig. 3. 6. When the molecular junction with an adsorbed H_2O molecule is stretched from *d* = 16.9 Å (Fig. 3.5a) to 18.7 Å (Fig. 3.5b, no bond breaking occurs in the Cu clusters and the electrical conductance during this elongation, marked by a) and b) in Fig. 3. 6, shows a gradual decline from 1 G_0 to 0.6 G_0. This is similar to the behavior observed experimentally in some cases for Cu junctions exposed to H_2O; see the two leftmost red curves in Fig.3.2a. At *d* = 18.8 Å (Fig. 3.5c) a Cu–Cu bond breaks between the Cu atom at the tip of the right Cu cluster and one of its neighbours. This results in the junction's conductance drop by ~0.36 G_0 from b) to c) in Fig.3.6. Very similar abrupt conductance drops were observed in our experiments as seen in the two leftmost red curves of Fig. 3.2a. The conductance decreases slightly upon further stretching and *G* approaches ~0.12 G_0 at the 19.05 Å distance in Fig. 3.6. At *d* = 19.1 Å, shown in Fig.3.5d and labelled (d) in Fig.3.6, one more Cu–Cu bond breaks, the Cu atomic chain with the adsorbed H_2O molecule is fully formed, and, counterintuitively, the conductance increases slightly. This conductance increase may be attributed to the reorientation of the Cu atomic chain (Fig. 3.5d) between the two Cu clusters with the H_2O molecule located at the centre of the chain.

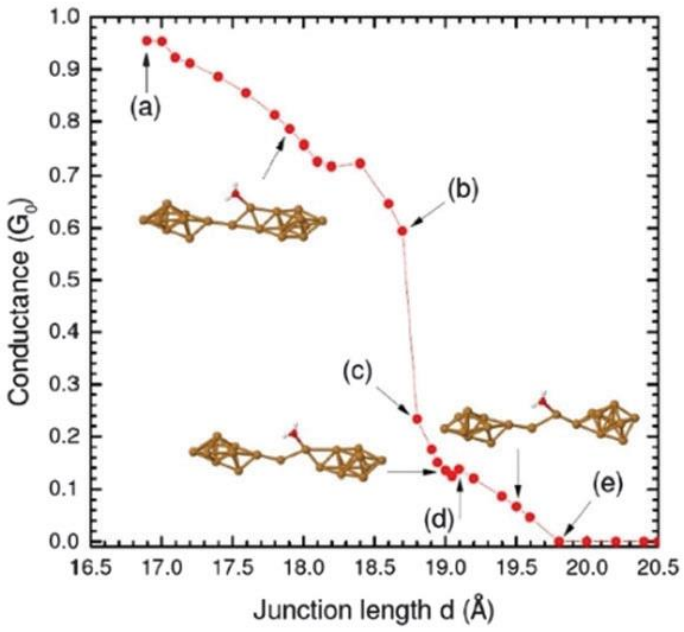

Figure 3.6 Calculated conductance values at zero temperature of a Cu molecular junction with a H_2O molecule for different junction lengths. Red circles marked a)–e) show the conductance values of the structures in Fig.3.5a)–e), respectively. The conductance values of intermediate structures obtained by stretching the junction starting from the geometry in Fig. 5a) until the junction breaks (and beyond) are also shown.

It is worth noting that although the conductance increase is small, this small conductance increase is in agreement with previous work on Au–propanedithiolate–Au molecular junctions [31] which showed the conductance increase of that molecular wire under tensile stress to be due to changing bond angles at the molecule–electrode interfaces and

structural changes in the Au electrodes. Similar small conductance increases at the ~0.1 G_0 plateau were observed in our experiments in some cases; see, for example, the leftmost red curve in Fig.3.2a.

Upon further stretching the junction from d = 19.1 to 19.6 Å, the conductance again decreases, while no Cu–Cu bond breaking occurs. This conductance reduction occurs due to the elongation of the junction and as a result a slight increase in the O–Cu–Cu bond angle is observed. Lengthening of Cu–Cu bonds which weakens the orbital overlap between the two neighbouring Cu atoms in the vicinity of the oxygen atom also contributes to the reduction of the conductance. At junction length d = 19.8 Å, the junction eventually breaks down resulting in the structure shown in Fig.3.5e. The adsorbed H_2O molecule is pulled back to its nearest Cu cluster and the conductance value becomes extremely small as labelled (e) in Fig. 3.6.

Based on the above description, a possible explanation of the Cu junction experiments in the presence and absence of H_2O is as follows: initially there is no H_2O attached directly to the atomic Cu junction and the conductance is 1 G_0. When a H_2O molecule attaches, forming a structure such as that in Fig. 3.5a or b, a gradual decline in the conductance from ~1 G_0 to a plateau at around ~0.7 G_0 occurs as shown in Fig.3. 6. The corresponding plateau in our experiment is located above ~0.5 G_0. Upon further stretching the structure changes (Fig. 3.5c) and there is an abrupt conductance drop to the plateau at 0.1 G_0. Thus both our experimental and theoretical results show a sequence of plateaus: first, at 1 G_0; second, at an intermediate conductance value; and third, at 0.1 G_0. In some cases, our experiments signal another possibility where the H_2O molecule attaches directly to the Cu junction in a structure similar to Fig.3. 5c or d, without going through the intermediate steps (Fig. 3.5a or b); therefore the conductance goes directly from 1 G_0 to values close to 0.1 G_0 as in the rightmost curve in Fig.3. 2a).

As well as the Cu junctions with an adsorbed H_2O molecule that we have discussed above, we have also studied other related junctions theoretically. For Cu clusters not linked by a Cu atom or Cu atomic chain but instead bridged by a H_2O molecule, hydroxyl group or oxygen atom chemically bonded to both Cu clusters, we found very small junction conductance values, up to a few times 0.001 G_0. We therefore conclude that such molecular junctions are not relevant to the present experiments where the observed conductance values prior to rupture of the junction were larger by 2 orders of magnitude.

Here, we propose a possible reason why only one preferred structure was formed for the Cu/H_2O system in contrast to the Pt/H_2O system [22]. The interaction between the H_2O molecule and Pt is stronger than for Cu, which is supported by the binding energy of H_2O to Cu(111) and Pt(111) surfaces [56]. When the interaction between a molecule and metal contact is strong, various kinds of contacts with different atomic configurations can be formed. Since the conductance of the contact depends on its atomic structure, the contact would show various conductance values. In contrast, when the interaction between a molecule and metal contact is weak, only the most energetically stable structure could be formed, which leads to the formation of the contact showing a fixed conductance value.

Other meta-stable structures would immediately break. Next, we discuss the stabilization mechanism of the Cu/H_2O junctions. Through our experimental and theoretical studies, it is revealed that the hydrated Cu junctions showing a conductance value of 0.1 G_0 were

highly stabilized and an atomic chain was formed. This stabilization could be explained by the reduction of the surface energy. The H_2O molecules should adsorb on the chain and the stem part of the Cu electrodes. The adsorbed molecules reduce the surface energy of the metal contacts, leading to the stabilization of the contact [57-58]. The adsorbed H_2O molecules would also act as scattering center of the conduction electrons in the Cu atomic contact. Therefore, the conductance of the 1 G_0 peak was decreased by the adsorbed H_2O molecules, as shown in Fig.3.2b.

3.5 Conclusion

We have studied the effects of mechanical stretching on the conductance of Cu nano-junctions in the presence H_2O molecules both experimentally and theoretically. The conductance of Cu nano-junctions was found to decrease in stages from near 1 G_0 upon elongation, exhibiting a stable conductance plateau near 0.1 G_0 before the junction rupture. Based on *ab initio* density functional theory and semi-empirical methods, we have demonstrated theoretically that the adsorption of a single H_2O molecule on the junction and ultimately to a Cu atomic chain bridging nano-junction can account for the observed behaviour. Our results demonstrate that the conductance values of molecular junctions using Cu electrodes are sensitive to the presence of an aqueous environment. This behavior may be of relevance in the development of Cu based mechanical nano-switches.

References

1. Kirczenow, G., in Oxford Handbook of Nanoscience and Technology, ed. Narlikar, A.; Fu, Y. Y., Oxford University Press, Oxford, **2010**, vol. 1, basic aspects.
2. Kiguchi, M. and Kaneko, S., Single molecule bridging between metal electrodes. *Phys. Chem. Chem. Phys.*, **2013**, *15* (7), 2253–2267.
3. Agraıt, N.; Yeyati, A. L; Van Ruitenbeek, J. M., Quantum properties of atomic-sized conductors. *Phys. Rep.*, **2003**, *377* (2), 81–279.
4. Scheer, E., Molecular electronics: an introduction to theory and experiment, World Scientific, **2010**.
5. Quek, S. Y.; Kamenetska, M.; Steigerwald, M. L.; Choi, H. J.; Louie, S. G. M. S. Hybertsen, S. G.; Neaton, J.; Venkataraman, L., Mechanically controlled binary conductance switching of a single-molecule junction. *Nat. Nanotechnol.*, **2009**, *4* (4), 230–234
6. D éz-P érez, I.; Hihath, J.; Lee, Y. ; Yu, L.; Adamska, L.; Kozhushner, M. A.; Oleynik, I. I.; Tao, N., Rectification and stability of a single molecular diode with controlled orientation. *Nat. Chem.*, **2009**, *1* (8), 635–641.
7. Song, H.; Kim, Y.; Jang, Y. H.; Jeong, H.; Reed M. A.; Lee, T., Observation of molecular orbital gating. *Nature*, **2009**, *462* (7276), 1039–1043.
8. Kiguchi, M.; T. Ohto, Fujii, S.; Sugiyasu, K.; Nakajima, S. ; Takeuchi, M. ; Nakamura, H. , Single molecular resistive switch obtained via sliding multiple anchoring points and varying effective wire length. *J. Am. Chem. Soc*., **2014**, *136* (20), 7327–7332.

9. Fujii, S.; Tada, T.; Komoto, Y.; Osuga, T.; Murase, T.; Fujita M.; Kiguchi, M., Rectifying electron-transport properties through stacks of aromatic molecules inserted into a self-assembled cage. *J. Am. Chem. Soc.*, **2015**, *137* (18), 5939–5947.
10. Demir, F.; Kirczenow, G., Communication: Identification of the molecule–metal bonding geometries of molecular nanowires. *J. Chem. Phys.*, **2011**, 134, 121103.
11. Demir, F.; Kirczenow, G., Identification of the atomic scale structures of the gold-thiol interfaces of molecular nanowires by inelastic tunneling spectroscopy. *J. Chem. Phys*., **2012**, *136* (1), 014703.
12. Djukic, D.; Van Ruitenbeek J.M., Shot noise measurements on a single molecule *Nano Lett*., **2006**, *6* (4), 789–793.
13. Christlieb, N.; Bessell, M. S.; Beers, T. C.; Gustafsson, B.; Korn, A.; Barklem, P. S.; Karlsson, T. ; Mizuno–Wiedner, M.; Rossi, S., A stellar relic from the early Milky Way *Nature*, **2002**, *419* (6910), 904–906.
14. Djukic, D.; Thygesen, K. S.; Untiedt, C.; Smit, R.; Jacobsen, K. W.; Van Ruitenbeek, J. M., Stretching dependence of the vibration modes of a single-molecule Pt- H_2-Pt bridge. *Phys. Rev. B*, **2005**, *71* (16), 161402.
15. Thygesen, K. S.; Jacobsen, K. W., Conduction mechanism in a molecular hydrogen contact. *Phys. Rev. Lett.*, **2005**, *94* (3), 036807.
16. Nakazumi. T.; Kiguchi, M., Formation of Co atomic wire in hydrogen atmosphere. *J. Chem. Phys.*, **2010**, *1* (6), 923–926.
17. Kiguchi, M., Hashimoto, K.; Ono, Y.; Taketsugu, T.; Murakoshi, K., Formation of a Pd atomic chain in a hydrogen atmosphere. *Phys. Rev. B*, **2010**, *81*(19), 195401.
18. Thijssen, W.; Marjenburgh, D.; Bremmer, R.; Van Ruitenbeek, J. M., Oxygen-enhanced atomic chain formation. *Phys. Rev. Lett.*, **2006**, *96* (2), 026806.
19. Nascimento, A.; San-Miguel, M. A.; Da Silva, E., Unveiling the origin of oxygen atomic impurities in Au nanowires. *Phys. Rev. B*, **2014**, *89* (8), 085417.
20. Kiguchi, M., Tatsuya, K.; Kei, M., Hydrogen-assisted stabilization of Ni nanowires in solution. *Appl. Phys. Lett.*, **2005**, *87* (4), 043104.
21. Kiguchi, M.; Kei, M., Fabrication of stable Pd nanowire assisted by hydrogen in solution. *Appl. Phys. Lett*., **2006**, 88 (25), 253112.
22. Tal, O.； Krieger, M.； Leerink，B.；Van Ruitenbeek, J. Electron-vibration interaction in single-molecule junctions: From contact to tunneling regimes. *Phys. Rev. Lett.*, **2008**, *100* (19), 196804.
23. Kaneko, S., Nakazumi, T.; Kiguchi, M., Fabrication of a well-defined single benzene molecule junction using Ag electrodes. *J. Chem. Phys.*, **2010**, *1* (24), 3520–3523.
24. Ren, J; Meng, S., First-principles study of water on copper and noble metal (110) surfaces. *Phys. Rev. B*, **2008**, *77* (5), 054110.
25. Kumagai, T.; Kaizu, M.; Hatta, S.; Okuyama, H.; Aruga, T.; Hamada, I.; Morikawa, Y., Direct observation of hydrogen-bond exchange within a single water dimer. *Phys. Rev. Lett*., **2008**, *100* (16), 166101.
26. Kumagai, T.; Shiotari, A.; Okuyama, H.; Hatta, S.; Aruga, T.; Hamada, I.; Frederikse, T. Ueba, H., H-atom relay reactions in real space. *Nat. Mater*., **2012**, *11* (2), 167–172.
27. Rodriguez, J. A.; Liu, P.; Hrbek, J.; Evans, J.; Perez, M., Water Gas Shift Reaction on Cu and Au Nanoparticles Supported on CeO_2(111) and ZnO(0001): Intrinsic Activity and

Importance ofSupport Interactions. *Angew. Chem., Int. Ed.*, **2007**, *46* (8), 1329–1332.
28. Nakamura, J.; Campbell, J. M.; Campbell, C. T., Kinetics and mechanism of the water-gas shift reaction catalysed by the clean and Cs-promoted Cu (110) surface: a comparison with Cu (111). *J. Chem. Soc., Faraday Trans.*, **1990**, *86* (15), 2725–2734.
29. Rodr ́guez, J. A.; Evans, J.; Graciani, J.; Park, J. B.; Liu, P.; Hrbek, J.; San, J. F., High Water− Gas Shift Activity in TiO_2 (110) Supported Cu and Au Nanoparticles: Role of the Oxide and Metal Particle Size. *J. Phys. Chem. C*, **2009**, *113* (17), 7364–7370.
30. Spitzer, A.; Lu ̈th, H., The adsorption of water on clean and oxygen covered Cu (110) *Surf. Sci*., **1982**, *120* (2), 376–388.
31. Smit, R.; Untiedt, C.; Yanson A.; Van Ruitenbeek, Common origin for surface reconstruction and the formation of chains of metal atoms. *J. Phys. Rev. Lett*., **2001**, *87* (26), 266102.
32. Bahn, S. R.; Jacobsen, K. W., Chain formation of metal atoms. *Phys. Rev. Lett*., **2001**, *87* (26), 266101.
33. Li, Y.; Kaneko, S.; Fujii, S.; Kiguchi, M., Symmetry of single hydrogen molecular junction with Au, Ag, and Cu electrodes. *J. Phys. Chem. C*, **2015**, *119* (33), 19143–19148.
34. Frisch, M. J.; Trucks, G. W.; Schlegel, H. B.; Scuseria, G. E.; Robb, M. A.; Cheeseman, J. R.; Scalmani, G.; Barone, V.; Mennucci, B.; Petersson, G. A.; Nakatsuji, H.; Caricato, M.; Li, X.; Hratchian, H. P.; Izmaylov, A. F.; Bloino, J.; Zheng, G.; Sonnenberg, J. L.; Hada, M.; Ehara, M.; Toyota, K. ; Fukuda, R.; Hasegawa, J.; Ishida, M.; Nakajima, T.; Honda, Y.; Kitao, O.; Nakai, H.; Vreven, T.; Montgomery, J. A.; Peralta, Jr., J. E.; Ogliaro, F.; Bearpark, M.; Heyd, J. J.; Brothers, E.; Kudin, K. N.; Staroverov, V. N.; Kobayashi, R.; Normand, J.; Raghavachari, K.; Rendell, A.; Burant, J. C.; Iyengar, S. S.; Tomasi, J.; Cossi, M.; Rega, N.; Millam, J. M.; Klene, M.; Knox, J. E.; Cross, J. B.; Bakken, V.; Adamo, C.; Jaramillo, J.; Gomperts, R.; Stratmann, R. E.; Yazyev, O.; Austin, A. J.; Cammi, R.; Pomelli, C.; Ochterski, J. W.; Martin, R. L.; Morokuma, K.; Zakrzewski, V. G.; Voth, G. A.; Salvador, P.; Dannenberg, J. J.; Dapprich, S.; Daniels, A. D.; Farkas, O ̈.; Foresman, J. B.; Ortiz, J. V.; Cioslowski, J.; Fox, D. J., Gaussian 09, revision A.02,
Gaussian, Inc., Wallingford, CT, **2009**.
35. The version of extended Hu ̈ckel theory used was that of Ammeter, J. H.; Bu ̈rgi, H.-B.; Thibeault, J. C.; Hoffman, R, Counterintuitive orbital mixing in semiempirical and ab initio molecular orbital calculations. *J. Am. Chem. Soc.*, **1978**, *100* (12), 3686–3692, as implemented in the YAEHMOP numerical package by G. A. Landrum and W. V. Glassey (Source-Forge, Fremont, California, **2001**).
36. Xu, B.; Xiao, X.; Tao, N. J., Measurements of single-molecule electromechanical properties. *J. Am. Chem. Soc.*, **2003**, *125*(52), 16164–16165.
37. Huang, Z.; Chen, F.; Bennett, P. A.; Tao, N., Single molecule junctions formed via au− thiol contact: stability and breakdown mechanism. *J. Am. Chem. Soc.*, **2007**, *129* (42) 13225–13231.
38. Saffarzadeh, A.; Demir, F.; Kirczenow, G., Mechanism of the enhanced conductance of a molecular junction under tensile stress. *Phys. Rev. B*, 2**014**, *89* (4), 045431.
39. Perdew, J. P.; Burke, K.; Ernzerhof, M., Generalized gradient approximation made simple. *Phys. Rev. Lett.*, **1996**, *77* (18), 3865–3868.
40. Demir, F. and Kirczenow, G. , Inelastic tunneling spectroscopy of gold-thiol and

gold-thiolate interfaces in molecular junctions: The role of hydrogen. *J. Chem. Phys.*, **2012**, *137* (9), 094703.

41. Cardamone D. M.; Kirczenow, G., Single-molecule device prototypes for protein-based nanoelectronics: Negative differential resistance and current rectification in oligopeptides. *Phys. Rev. B*, **2008**, *77* (16), 165403.

42. Cardamone D. M.; Kirczenow, G., Electrochemically gated oligopeptide nanowires bridging gold electrodes: novel bio-nanoelectronic switches operating in aqueous electrolytic environments. *Nano Lett.*, **2010**, *10* (4), 1158–1162.

43. Kirczenow, G.; Piva, P. G.; Wolkow, R. A., Linear chains of styrene and methylstyrene Modulation of electrical conduction through individual molecules on silicon by the electrostatic fields of nearby polar molecules: Theory and experimentmolecules and their heterojunctions on silicon: Theory and experiment. *Phys. Rev. B*, **2005**, *72* (24), 245306.

44. Kirczenow, G.; Piva, P. G.; Wolkow, R. A., Modulation of electrical conduction through individual molecules on silicon by the electrostatic fields of nearby polar molecules: Theory and experiment. *Phys. Rev. B*, **2009**, *80* (3), 035309.

45. Piva, P. G. Wolkow, R. A.; Kirczenow, G., Nonlocal conductance modulation by molecules: scanning tunneling microscopy of substituted styrene heterostructures on H-terminated Si (100). *Phys. Rev. Lett.*, **2008**, *101* (10), 106801.

46. Dalgleish, H.; Kirczenow, G., Theoretical study of spin-dependent electron transport in atomic Fe nanocontacts. *Phys. Rev. B.*, **2005**, *72* (12), 155429.

47. Dalgleish, H.; Kirczenow, G., A New Approach to the Realization and Control of Negative Differential Resistance in Single-Molecule Nanoelectronic Devices: Designer Transition Metal− Thiol Interface States. *Nano Lett.*, **2006**, *6* (6), 1274.

48. Kirczenow, G., Ballistic electron spectroscopy of individual buried molecules. *Phys. Rev. B*, **2007**, *75* (4), 045428.

49. Renani, F. R.; Kirczenow, G., Ligand-based transport resonances of single-molecule-magnet spin filters: Suppression of coulomb blockade and determination of easy-axis orientation. *Phys. Rev. B*, **2011**, *84* (18), 180408.

50. Renani, F. R.; Kirczenow, G. Tight-binding model of Mn 12 single-molecule magnets: Electronic and magnetic structure and transport properties. *Phys. Rev. B*, **2012**, 85 (24), 245415.

51. Renani, F. R.; Kirczenow, G., Switching of a quantum dot spin valve by single molecule magnets. *Phys. Rev. B*, **2013**, *87* (12), 121403.

52. Kushmerick, J.; Holt, D.; Yang, J.; Naciri, J; Moore, M.; Shashidhar, R., Metal-molecule contacts and charge transport across monomolecular layers: Measurement and theory. *Phys. Rev. Lett.*, **2002**, *89* (8), 086802.

53. Datta, S.; Tian, W.; Hong, S.; Reifenberger, R.; Henderson, J. I.; Kubiak, C. P., Current-voltage characteristics of self-assembled monolayers by scanning tunneling microscopy. *Phys. Rev. Lett.*, **1997**, *79* (13), 2530.

54. Emberly, E. G.; Kirczenow, G., Comment on "First-principles calculation of transport properties of a molecular device". *Phys. Rev. Lett.*, **2001**, 87 (26), 269701.

55. Emberly, E. G.; Kirczenow, G., Models of electron transport through organic molecular monolayers self-assembled on nanoscale metallic contacts. *Phys. Rev. B*, **2001**, *64* (23), 235412.

56. Michaelides, A.; Ranea, V. A.; De Andres, P. L.; King, D. A., General model for water monomer adsorption on close-packed transition and noble metal surfaces. *Phys. Rev. Lett.*, **2003**, *90* (21), 216102.
57. French, W. R.; Iacovella, C. R.; Cummings, P. T., The influence of molecular adsorption on elongating gold nanowires. *J. Phys. Chem. C*, **2011**, *115* (38), 18422–18433.
58. Kaneko, S., Nakamura, Y.; Zhang, J.; Yang, X.; Zhao J.; Kiguchi, M., Formation of single Cu atomic chain in nitrogen atmosphere. *J. Phys. Chem. C*, **2014**, *119* (1), 862–866.

Chapter 4

Atomic structure of water/Au, Ag, Cu and Pt atomic junction

4.1 Introduction

It is becoming apparent that silicon semiconductors cannot satisfy the increasing demands of miniaturization in modern electronic technologies. Low dimensional atomic and molecular devices have been studied since the 1970s as a result of their unique electrical, optical and reactive properties, which are different from those of macroscopic materials [1-2]. Single atomic and molecular junctions have been used as active components in nanoelectronics based on mechanically controllable break junctions (MCBJs) and scanning tunnelling microscopy (STM) break junction techniques [2-4]. Molecular diodes, switches, transistors and sensors have now been realized with single atomic and molecular junctions [5-10]. Fujii *et al.* reported the properties of a single molecular junction consisting of p-stacked donor and acceptor molecules [10]. Bui *et al.* reported the high sensitivity to DNA of single molecular junctions based on conductance measurements [11]. Most current research focuses on electron transport properties without a detailed understanding of the atomic and electronic structures of the target single molecular junctions. As a result of the lack of structural information, the reproducibility of the experimental results for single molecular junctions is low. This is the main difficulty in the practical application of devices based on molecular junctions.

The characterization of single molecular junctions is possible for small, simple molecules [12-15]. Smit *et al.* investigated Pt/H_2 junctions using point contact spectroscopy, conductance fluctuation and conductance measurements [14]. A single hydrogen molecule was shown to bridge the Pt electrodes with its molecular axis parallel to the junction axis. Asymmetrical single hydrogen molecular junctions were formed for Cu electrodes and symmetrical single hydrogen and oxygen molecular junctions were formed for Au and Ag electrodes based on the current– voltage characteristics of the single molecular junctions [15].

Single molecular junctions with diatomic molecules have been investigated in detail and the next target is simple heteronuclear molecules. In this chapter we focused on water (H_2O) molecules. Water–metal systems have attracted widespread attention as a result of their applications in catalysis, corrosion, electrolysis, photosynthesis and hydrogen fuel cells. Rodriguez *et al.* showed that the effectiveness of the water gas shift reaction improved on Cu and Au nanoparticles supported on CeO_2(111) and ZnO(0001) at 625 K [16]. Bedu ̈rftig *et al.* showed that water molecules decomposed on Pt(111) at 600 K and the resultant the OH species could be detected by vibrational spectroscopy [17]. Tal *et al.* investigated single water molecule junctions with Pt electrodes and found that they did

not have a fixed conductance value [18]. The structure of single water molecule junctions is not yet clear. Geometrical information about single molecular junctions can be revealed by a detailed analysis of the change in conductance during stretching of the junction. Length analysis of the conductance plateau has shown the chain structure of Au, Pt, Ir and Pt/H_2 junctions [19-20].

We investigated water–Au, Ag, Cu and Pt junction systems using MCBJs at 10 K. We focused on the coinage metals Au, Ag, Cu and Pt as the metal electrodes because surface-localized plasmons are formed for the nanostructures of these metals and photochemical reactions using an enhanced field can be studied with water–coinage metal junction systems. The coinage metals are non-reactive and we therefore investigated the water–Pt junction system for comparison. Conductance measurements and length analysis of the conductance traces showed that the strength of the water–metal interaction decreased in the order Pt > Cu > Au > Ag. Au is inert in bulk materials. The change in the order of chemical reactivity can be explained by the chain structure of the water–Au junction system.

4.2 Experimental

The experiments were performed with an MCBJ setup at about 10 K [19]. The metal wires (ca. 0.1 mm) were notched in the center and then glued onto phosphor bronze substrates and covered with polyimide tape. A three-point bending configuration in a custom-made vacuum pot was used for the break junction process. A metal wire was broken by bending the substrate and a metal atomic contact could be formed just before breaking the wires. Deionized H_2O was placed in a quartz tube and was degassed by three cycles of freezing, pumping and thawing. While the metal junctions were repeatedly broken and formed, water molecules were introduced to the junction through a heated capillary. DC two-point voltage-biased conductance measurements were made during the breaking process under an applied bias voltage of 100 mV.

4.3 Results and discussion

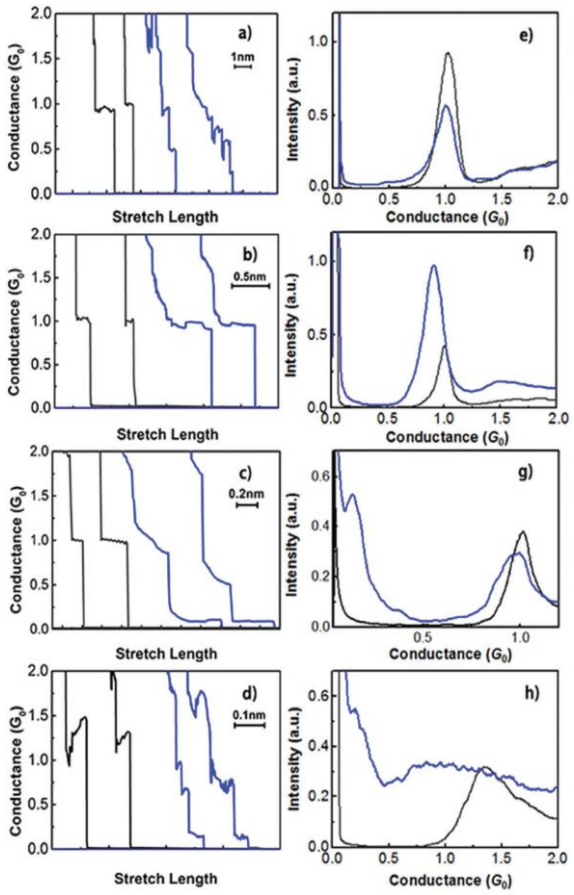

Figure 4.1 Conductance histograms of (a and e) Au, (b and f) Ag, (c and g) Cu and (d and h) Pt contacts before (grey) and after (blue) the introduction of water. The bin size was 0.004 G_0.

Figure 4.1 shows the conductance traces and histograms of the Au, Ag, Cu and Pt contacts before and after the introduction of water. The conductance histograms were constructed without data selection from more than 1000 conductance traces recorded during breaking of the metal contacts. The intensity of the conductance histograms was normalized by the number of conductance traces. For pure metal contacts, 1 G_0 ($G_0 = 2e^2/h$) peaks were observed for Au, Ag and Cu, whereas a 1.4 G_0 peak was observed for the Pt contacts, in agreement with previously reported results [20-21]. No feature was observed in the conductance regime below 1 G_0 for any of the pure metal contacts, indicating the absence of adsorbates and impurities on the metal atomic junctions. The introduction of water to the metal contacts induced changes in the conductance (blue line). In the low conductance regions (<1.0 G_0 for Cu, <1.4 G_0 for Pt), new, clear conductance features appeared for the Cu and Pt contacts, indicating the formation of single water molecule junctions. A clear 0.1 G_0 peak was observed for the Cu contacts, whereas the clear 1.4 G_0 peak was suppressed and a continuous broad feature was observed for the Pt contact. The change in the conductance histogram in the low conductance regime was less obvious for the Au and Ag contacts. Small, continuous features were observed for the Au contact, but there were few features for the Ag junctions. These results indicate that single

water molecule junctions were sometimes formed for the Au contacts, but not for the Ag contacts. The intensity of the 1 G_0 peak increased for the Ag junctions, but this change was less clear for the Au and Cu junctions. Analysis of the conductance histograms indicated that the water–metal interactions decreased in the order Pt > Cu > Au, Ag.

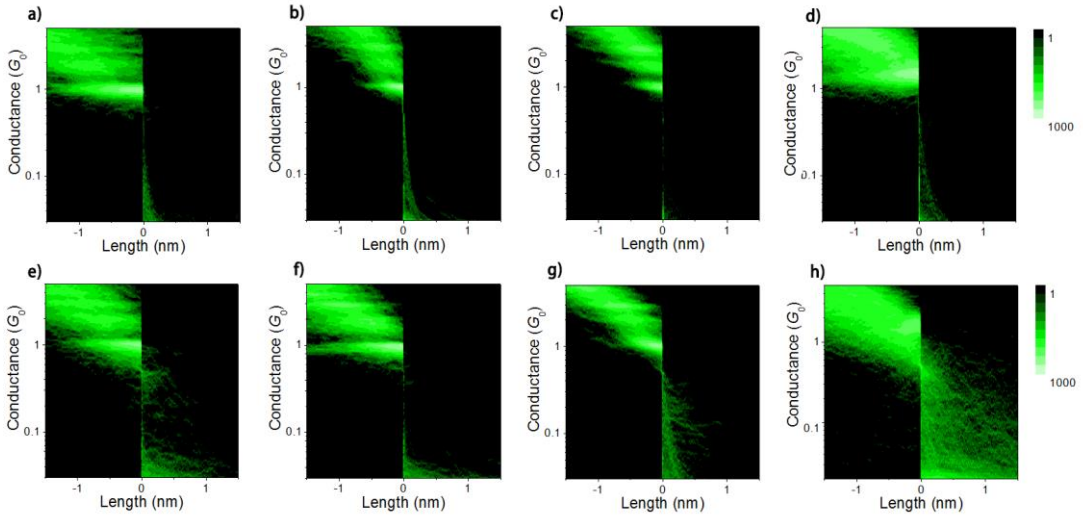

Figure 4.2 2D conductance histograms for (a and e) Au, (b and f) Ag, (c and g) Cu and (d and h) Pt contacts before and after the introduction of water.

Figure 4.2 shows the 2D conductance histograms of the Au, Ag, Cu and Pt contacts before and after the introduction of water. These histograms were generated by identifying the first data point that had a conductance value <1.2 G_0 for the Au, Ag and Cu contacts and 0.5 G_0 for the Pt contacts, and assigning this as a relative zero distance (z = 0) for each trace, then overlapping all the individual traces in 2D space. Large counts were observed in the region >1 G_0 for all contacts. The effect of the introduction of water was clear in the 2D histograms of the Pt and Cu contacts. After the introduction of water, intense counts appeared in the conductance regime at <0.5 G_0 for the water–Pt junction system and some weak counts were observed around 0.3 G_0 for the water–Cu junction system. In contrast with the Pt and Cu contacts, the counts were not clear in the conductance regime 1–0.03 G_0 for the water–Au and water–Ag junction systems.

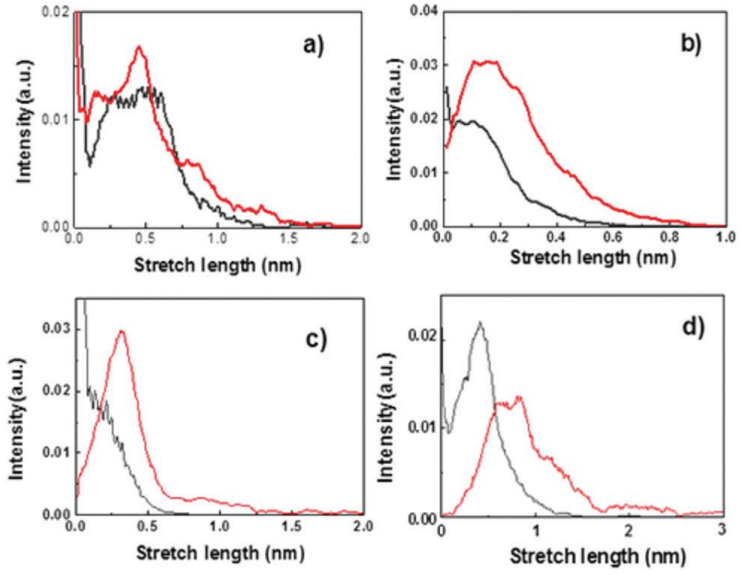

Figure 4.3 Length histograms of the a) Au, b) Ag, c) Cu and d) Pt contacts before (grey) and after (red) the introduction of water.

To obtain structural information about the water–metal junction system, the length of the conductance plateau was analysed for >1000 breaking processes. The plateau length was defined as the distance between the points at which the conductance dropped below 1.20 G_0 and 0.04 G_0 for the Au, Ag and Cu junctions and 1.80 G_0 and 0.04 G_0 for Pt junctions. Fig. 4. 3 shows the length histograms of the Au, Ag, Cu and Pt junctions before and after the introduction of water. For the pure Au and Pt junctions, the junctions can be extended more than 1 nm, indicating the formation of metal atomic wires. The average plateau lengths were 0.47 and 0.49 nm for the Au and Pt junctions, respectively. For the Ag and Cu junctions, most of atomic junctions broke within 0.30 nm and the average plateau length was 0.14 nm for both metal atomic junctions. The short plateau length meant that metal atomic wires were not formed for the Ag and Cu contacts, in agreement with previously reported results [21]. The formation of metal atomic wires is only observed for 5d metals, including Au, Pt and Ir, and the formation of wires can be explained by relativistic effects [22].

After the introduction of water, the plateau length of the Au and Ag junctions did not change dramatically. The average plateau length increased by 36% for the Au junctions (average 0.64 nm) and 50% for the Ag junctions (average 0.21 nm). The Cu and Pt junctions were obviously stretched after the introduction of water. The average plateau length increased by 270% for the Cu junctions (average 0.52 nm) and 220% for the Pt junctions (average 1.55 nm). Metal atomic wires or single molecular wires were formed after the introduction of water for the Cu junctions, although the wires were very short. The introduction of water caused an increase in the plateau length for all metals, although the degree of change varied with the metal. The elongation of the plateau length can be explained by the decrease in the surface energy of the metal atomic junctions caused by the adsorption of water molecules [23]. A similar elongation of the plateau length has been observed for other systems, including H_2–Pd, Co junctions and benzenedithiol–Au junctions [24]. Analysis of the plateau length indicated that the water–metal interactions decreased in the order Pt, Cu>Au, Ag.

Conductance measurements and analyses of the plateau length indicated that the strength of the adsorption of water molecules to the metal electrodes decreased in the order Pt, Cu, Au and Ag and can be discussed on the basis of the chemical reactivity of metals and the structure of the junction. A previously reported theoretical study showed that the adsorption energies of water molecules on the metal surface were 0.35, 0.24, 0.18 and 0.13 eV for Pt, Cu, Ag and Au, respectively [23]. The strength of the interaction between the water molecule and the metal decreased in the order Pt >Cu >Ag >Au. This order is different from our results for Au and Ag. One possible reason for this is the formation of long atomic wires for the Au junctions, whereas Ag did not form stable atomic wires. The plateau length analysis showed the formation of atomic wires for the water–Au junction system. The chemical reactivity of metal atoms increases with decreases in the coordination number of atoms [25]. For example, the isomerization and hydrocracking reactions of hydrocarbon molecules selectively proceed at the step or kink sites on the metal surface (Ni, Pt, Ir, Au) [23, 26-27]. The coordination number of atoms in the step and

kink is smaller than that on the flat surface. The decomposition of hydrogen molecules proceeded on the Au atomic wires, whereas the hydrogen molecules only weakly interacted with the flat Au surface [28-29]. When the metal atoms formed wire configurations, the coordination number reduced to two, so the interaction between the water molecule and the metal atomic wire was larger than the metal atomic contact (not a wire). In the current results, the metal atomic wire was less stable in the water–Ag junction system, thus the interaction between the water molecule and the Ag atomic contact was smaller than that for the Au atomic wire. This explains why the change in the conductance histogram was larger for the water–Au contact than for the water–Ag contact.

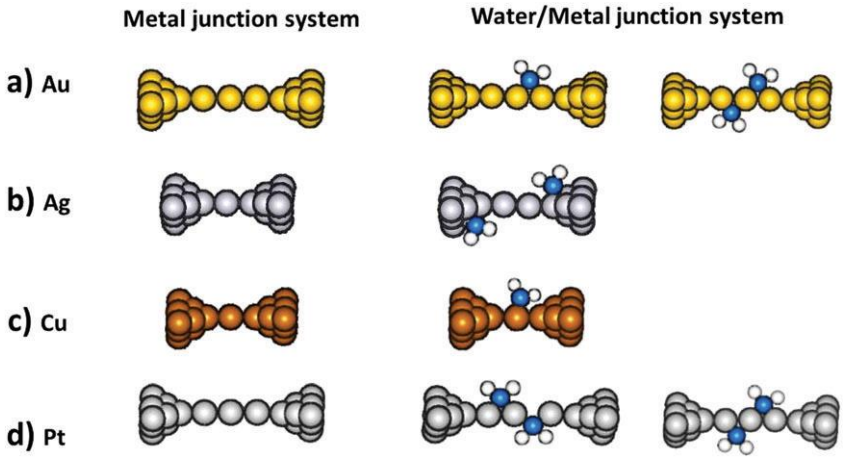

Figure 4.4 Structural model of pure metal and water–metal junction systems. a) Au, b) Ag, c) Cu and (d) Pt.

The conductance behavior and structure of the water–Au, Ag, Cu and Pt junction systems was investigated. An atomic wire was formed for the water–Pt junction system. The atomic Pt wire provided a variety of adsorption sites for water molecules. The adsorbed molecules acted as a scattering center for the conduction electrons in the metal junction. The conductance of the metal contact or wire decreased with the number of adsorbed molecules [30]. The water–Pt junction system therefore showed different conductance values depending on the number of water molecules adsorbed and a continuous broad feature was observed in the conductance histogram. The strong water–Pt interaction interfered with the formation of a pure Pt atomic junction, leading to suppression of the clear 1.4 G_0 peak observed for pure Pt junctions. We did not make vibrational spectroscopy measurements and thus it is difficult to determine whether a single water molecule bridged the Pt electrodes or whether a single water molecule was adsorbed on a Cu atom of a Cu atomic junction. Thus two possible model structures are shown in Fig. 4. 4d. For the coinage metal (Au, Ag and Cu) contacts, the interaction between the water molecule and the metal junction was much weaker tha the Pt junctions and the 1 G_0 peak corresponding to the pure metal atomic junction was still observed after the introduction of water. Among the coinage metals, the water–metal interaction was largest for Cu. The change in the 1 G_0 peak width in the conductance histogram was largest for the water–Cu junction system. In this system, only a short atomic wire was formed and thus the adsorption sites for the water molecule were limited. The atomic configuration of the water single molecular junction was fixed, leading to a clear 0.1 G_0 peak in the conductance histogram. A previously reported theoretical study for the water–

Cu junction system showed that the conductance of the junction when a single water molecule bridges the Cu electrodes was 0.001 G_0, which is much smaller than 0.1 G_0 observed in the present study [21]. Therefore we concluded that the observed 0.1 G_0 peak corresponded to the formation of a junction where a single water molecule was adsorbed on a Cu atom at the Cu atomic junction (Fig.4.4c). For the water–Au junction system, a long atomic wire was formed. The Au atomic wire offered plenty of adsorption sites for the water molecules and increased the strength of the water molecule–metal interaction. The adsorption of the water molecule on the surface of the Au atomic wire led to a weak but continuous feature in the low conductance region of the conductance histogram. The interaction between the water molecule and Au was close to that of Cu [23].The atomic structure of the water–Au junction system was close to that of the water–Cu junction system (Fig.4.4a). Metal atomic wires were not formed in the water–Ag junction system. The absence of formation of a metal atomic wire and the weak water–metal interaction resulted in only a small change in the conductance histogram (Fig. 4. 4b)

4.4 Conclusion

We investigated the structure and electrical conductance of water–Au, Ag, Cu and Pt junction systems using MCBJs at 10 K. The conductance measurements indicated the formation of single water molecule junctions for the water–Au, Cu and Pt junction systems. The conductance histogram for the Pt contacts changed dramatically after the introduction of water, reflecting the high reactivity of the Pt metal. For the water–Cu contacts, a clear sharp peak appeared in the conductance histogram, which was caused by the significant interaction between the water molecule and the Cu metal and the fact that the water–Cu junction system did not form an atomic wire. As the possible adsorption sites were limited for the short atomic contact, the atomic configuration was fixed for the water–Cu junction, leading to a well-defined peak in the conductance histogram. This weak but continuous feature also appeared for the water–Au contacts. Although the interactions between the water molecules and Au are weak in bulk materials, the atomic wire offered plenty of adsorption sites for water molecules and increased the strength of the molecule–metal interaction. The atomic wire was less stable for the water–Ag junction system than for the water–Au junction system and the strength of the molecule–metal interaction did not increase as much for the water–Ag junction system. Therefore a single water molecule junction was not formed for the water–Ag junction system.

References

1. Aviram, A.; Ratner, M.A., Molecular rectifiers. *Chem. Phys. Lett.*, **1974**, *29* (2), 277–283.
2. Agraıt, N.; Yeyati, A. L.; Van Ruitenbeek, J. M., Quantum properties of atomic-sized conductors. *Phys. Rep*., **2003**, *377* (2), 81–279.
3. Scheer, E., Molecular electronics: an introduction to theory and experiment, World Scientific, **2010**.

4. Scheer, E. , Agra ït, N.; Cuevas, J. C.; Yeyati, A. L.; Ludoph, B.; Mart ín-Rodero, A.; Bollinger, G. R.; Van Ruitenbeek, J. M.; Urbina, C., The signature of chemical valence in the electrical conduction through a single-atom contact. *Nature*, **1998**, *394* (6689), 154–157.
5. Kiguchi, M., Ohto, T.; Fujii, S., Sugiyasu, K.; Nakajima, S.; Takeuchi, M.; Nakamura, H., Single molecular resistive switch obtained via sliding multiple anchoring points and varying effective wire length. *J. Am. Chem. Soc.*, **2014**, *136* (20), 7327–7332.
6. Tao, N., Electron transport in molecular junctions. *Nat. Nanotechnol.*, **2006**, *1* (3), 173–181.
7. Chen, F.; Tao, N., Electron transport in single molecules: from benzene to graphene. *Acc. Chem. Res.*, **2009**, *42* (3), 429–438.
8. Venkataraman, L.; Klare, J. E.; Nuckolls, C.; Hybertsen, M. S.; Steigerwald, M. L., Dependence of single-molecule junction conductance on molecular conformation. *Nature*, **2006**, *442* (7105), 904–907.
9. Quek, S. Y.; Kamenetska, M.; Steigerwald, M. L.; Choi, H. J.; Louie, S. G.; Hybertsen, M. S.; Neaton, J.; Venkataraman, L., Mechanically controlled binary conductance switching of a single-molecule junction. *Nat. Nanotechnol.*, **2009**, *4* (4), 230–234.
10. Fujii, S., Tada, T.; Komoto, Y.; Osuga, T.; Murase, T.; Fujita, M.; Kiguchi, M., Rectifying electron-transport properties through stacks of aromatic molecules inserted into a self-assembled cage. *J. Am. Chem. Soc*., **2015**, *137* (18), 5939–5947.
11. Bui, P. T.; Nishino, T.; Shiigi, H.; Nagaoka, T., One-by-one single-molecule detection of mutated nucleobases by monitoring tunneling current using a DNA tip. *Chem. Commun*., **2015**, *51* (9), 1666–1669.
12. Konishi, T. ; Kiguchi, M., Takase, M.; Nagasawa, F.; Nabika, H.; Ikeda, K.; Uosaki, K.; Ueno, K.; Misawa, H.; Murakoshi, K., Single molecule dynamics at a mechanically controllable break junction in solution at room temperature. *J. Am. Chem. Soc.*, **2013**, *135* (3), 1009–1014.
13. Kaneko, S., Murai, D.; Marques-Gonzalez, S.; Nakamura, H.; Komoto, Y.; Fujii, S., Nishino, T.; Ikeda, K.; Tsukagoshi, K.; Kiguchi, M., Site-selection in single-molecule junction for highly reproducible molecular electronics. *J. Am. Chem. Soc.*, **2016**, *138*(4), 1294–1300.
14. Smit, R.; Noat, Y.; Untiedt, C.; Lang, N.; Van Hemert M. V.; Van Ruitenbeek, J. Measurement of the conductance of a hydrogen molecule. *Nature*, **2002**, *419* (6910), 906–909.
15. Li, Y; Kaneko, S.; Fujii, S.; Kiguchi, M., Symmetry of single hydrogen molecular junction with Au, Ag, and Cu electrodes. *J. Phys. Chem. C*, **2015**, *119* (33), 19143–19148.
16. Rodriguez, J. A.; Liu, P.; Hrbek, J.; Evans, J.; Perez, M., Water Gas Shift Reaction on Cu and Au Nanoparticles Supported on CeO_2(111) and ZnO(0001): Intrinsic Activity and Importance ofSupport Interactions. *Angew. Chem., Int. Ed.*, **2007**, *46* (8), 1329–1332.
17. Bedu ïrftig, K.; Vo ïlkening, S.; Wang, Y.; Wintterlin, J.; Jacobi, K.; Ertl, G., Vibrational and structural properties of OH adsorbed on Pt (111). *J. Chem. Phys.*, **1999**, *111* (24), 11147–11154.
18. Tal, O.； Krieger, M.； Leerink，B.；Van Ruitenbeek, J. Electron-vibration interaction

in single-molecule junctions: From contact to tunneling regimes. *Phys. Rev. Lett.*, **2008**, *100* (19), 196804.

19. Smit, R. H. M.; Untiedt, C.; Yanson, A. I.; van Ruitenbeek, J. M. Common Origin for Surface Reconstruction and the Formation of Chains of Metal Atoms. Phys. Rev. Lett. 2001, 87, 266102.
20. Kiguchi, M., Stadler, R.; Kristensen, I. S.; Djukic, D.;Van Ruitenbeek, J. M., Evidence for a single hydrogen molecule connected by an atomic chain. *Phys. Rev. Lett*., **2007**, *98* (14), 146802.
21. Li, Y.; Demir, F.; Kaneko, S., Fujii, S., Nishino, T.; Saffarzadeh, A.; Kirczenow, G.; Kiguchi, M., Electrical conductance and structure of copper atomic junctions in the presence of water molecules. *Phys. Chem. Chem. Phys.*, **2015**, *17* (48), 32436–32442.
22. Pyykko, P., Relativistic effects in structural chemistry. *Chem. Rev.*, **1988**, *88* (3), 563–594.
23. Michaelides, A.; Ranea, V.; De Andres, P.; King, D., General model for water monomer adsorption on close-packed transition and noble metal surfaces. *Phys. Rev. Lett.*, **2003**, *90* (21), 216102.
24. Murai, D.; Nakazumi, T.; Fujii, S., Komoto, Y.; Tsukagoshi, K.; Motta. C.; Kiguchi, M., Highly stable Au atomic contacts covered with benzenedithiol under ambient conditions. *Phys. Chem. Chem. Phys.*, **2014**, *16* (29), 15662–15666.
25. Falicov, L.; Somorjai, G., Correlation between catalytic activity and bonding and coordination number of atoms and molecules on transition metal surfaces: Theory and experimental evidence. *Proc. Natl. Acad. Sci. U. S. A.*, **1985**, *82* (8), 2207–2211.
26. Smith, C.; Biberian, J.; Somorjai, G., The effect of strongly bound oxygen on the dehydrogenation and hydrogenation activity and selectivity of platinum single crystal surfaces. *J. Catal.*, **1979**, *57* (3), 426–443.
27. Yeates, R.; Somorjai, G., Surface structure sensitivity of alloy catalysis: Catalytic conversion of n-hexane over Au-Pt (111) and Au-Pt (100) alloy crystal surfaces. *J. Catal.*, **1987**, *103* (1), 208–212.
28. Kiguchi, M., Konishi, T.; Murakoshi, K., Conductance bistability of gold nanowires at room temperature. *Phys. Rev. B*, **2006**, *73* (12), 125406.
29. Kiguchi, M., Konishi, T.; Hasegawa, K.; Shidara, S.; Murakoshi, K., Three reversible states controlled on a gold monoatomic contact by the electrochemical potential. *Phys. Rev. B*, **2008**, *77* (24), 245421.
30. Kiguchi, M.; Konishi, T.; Murakoshi, K., Conductance bistability of gold nanowires at room temperature. *Phys. Rev. B*, **2006**, *73* (12), 125406.

Chapter 5

Symmetry of Single Hydrogen Molecular Junction with Au, Ag, and Cu Electrodes

5.1 Introduction

The theoretical proposal of a molecular device by Aviram and Ratner [1]. and the subsequent realization of single-molecule junctions [2,3] have opened a new frontier in nanoscience research [4–10]. Among various single-molecule junctions, single hydrogen molecular junctions have been studied as a model system of single-molecule junctions. Single hydrogen molecular junctions have been studied with Pt, Pd, Fe, Co, Ni, Au, Ag, and Cu electrodes [11–18]. The Pt/H_2 junction has been most extensively studied, by conductance, point-contact spectroscopy, inelastic electron tunneling spectroscopy (IETS), conductance fluctuation, and shot-noise measurements, as well as theoretical calculations [11-12, 19]. Detailed studies revealed that a single hydrogen molecule bridges between Pt electrodes with its molecular axis parallel to the junction axis and that electrons transport through a single channel with a transmission probability close to one. In the case of Pd and Co electrodes, the formation of single hydrogen molecular wires was revealed by conductance measurements [14-15]. Here, it is noted that clean Pd and Co do not form atomic wires. The introduction of hydrogen onto the metal atomic contact stabilizes the single molecule wires.

Interest has been growing in single hydrogen molecular junctions with coinage metals (Au, Ag, and Cu), because their application to molecular electronics is easier than that of more reactive transition metals [16–18]. However, few systematic studies have been reported on single hydrogen molecular junctions with coinage metals, in contrast with transition-metal electrodes. Two-dimensional (2D) conductance histograms have not been reported for coinage metals, and IETS results have not been reported for Ag/H_2 junctions. Recent conductance and IETS measurements of Cu/H_2 junctions suggested the formation of asymmetric single hydrogen molecular junctions [18]. The structural symmetry of the single-molecule junction is an interesting topic. The appearance of diode properties is predicted theoretically for asymmetric molecular junctions [20]. However, few experimental investigations have been conducted on the symmetry of single-molecule junctions, including Cu/H_2 junctions. Here, we consider the current- voltage ($I-V$) characteristics as a tool for studying the symmetry of single-molecule junctions. Because the symmetry of a single-molecule junction affects its electron-transport properties, the current−voltage characteristics should provide information about the symmetry of the single-molecule junction. We systematically investigated Au/H_2, Ag/H_2 and Cu/H_2 junctions using the

mechanically controllable break junction (MCBJ) technique at low temperature. Conductance, IETS, $I-V$ curve and length analyses of single-molecule junctions were performed. The formation of single hydrogen molecular junctions was confirmed by conductance and IETS measurements. The $I-V$ characteristics revealed that Au/H_2 and Ag/H_2 junctions have symmetric metal−molecule contacts, whereas Cu/H_2 junctions exhibit asymmetric metal−molecule contacts. The structural symmetry of single hydrogen molecular junctions are discussed on the basis of the chain-length analysis of single hydrogen molecular junctions.

5.2 Experimental

Experiments were performed under ultrahigh vacuum (UHV) using an MCBJ setup at about 10 K, following previous research [18]. Briefly, a notched Au, Ag, or Cu wire (0.10 mm in diameter) was fixed on top of an electrically insulated phosphor bronze substrate with polyimide tape. The substrate was mounted in a three-point bending configuration in a custom-made vacuum pot. The metal wire was broken at the notch by bending of the substrate. A single atomic contact could be formed just prior to the breaking of the wire. Hydrogen gas was introduced onto the metal contacts through a capillary. Then, dc two-point voltage-biased conductance measurements were performed during the breaking process under an applied bias voltage of 100 mV. The differential conductance was measured using a standard lock-in technique with ac modulation at 1 mV and 7.777 kHz. The conductance was monitored for a fixed contact configuration during the dc bias between −100 to +100 mV. The $I-V$ characteristics were measured by sweeping the bias voltage. The bias voltage started from 50 or 100 mV, increased to +1.0 V, decreased to −1.0 V, and returned to the initial bias voltage. The sweep rate of $I-V$ characteristic measurements was 100 kHz. Experiments were performed for seven, six, and five independent samples for Au, Ag, and Cu electrodes, respectively.

5.3 Results and discussion

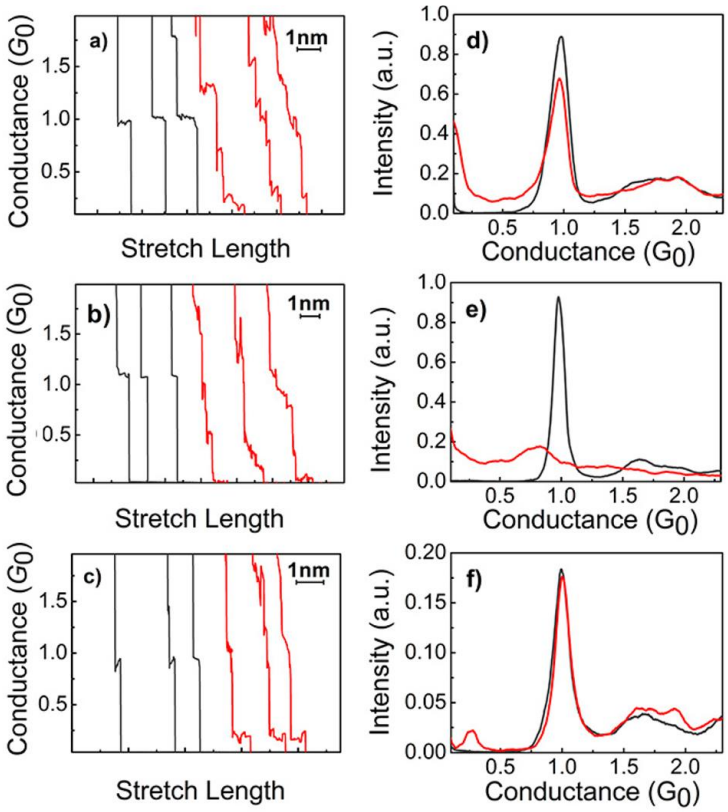

Figure 5.1. Typical (a−c) conductance traces and (d−f) conductance histograms of (a,d) Au, (b, e) Ag, and (c, f) Cu before (black lines) and after (red lines) the introduction of hydrogen. The conductance histograms were constructed without data selection from more than 1000 conductance traces during a breaking process of the metal contacts. The intensity of the conductance histograms was normalized to the number of the conductance traces used for constructing the histogram. The bin size was 0.004 G_0.

Figure 5.1 shows typical conductance traces and conductance histograms for Au, Ag, and Cu contacts before and after the introduction of hydrogen. The stretch length was defined as the displacement between the stem parts of the metal electrodes, which were fixed with an epoxy adhesive. Conductance histograms were constructed from over 1000 conductance traces obtained during the breaking process. For clean metal contacts, steps appeared at $1G_0$ ($G_0 = 2e^2/h$) in the conductance traces, and the conductance histograms showed prominent peaks at 1 G_0, corresponding to clean metal atomic contacts [17]. After the introduction of H_2, additional steps appeared below 1 G_0. The conductance values of the steps fluctuated with the conductance traces for the Au and Ag electrodes, leading to a broad feature in the conductance histograms. For the Cu electrodes, clear steps appeared at 0.3 G_0 in the conductance traces, and a sharp 0.3 G_0 peak appeared in the conductance histogram. The appearance of a broad feature for the Au electrode and a sharp 0.3 G_0 peak for the Cu electrode agreed with previously reported results [18, 21]. In addition to the appearance of

features below 1 G_0, the 1 G_0 peak in the conductance histogram changed after the introduction of hydrogen for Au and Ag electrodes. The intensity of the 1 G_0 peak decreased for the Au and Cu electrodes, and the conductance value of the 1 G_0 peak decreased for the Ag electrodes. We discuss these conductance behaviors later in this section.

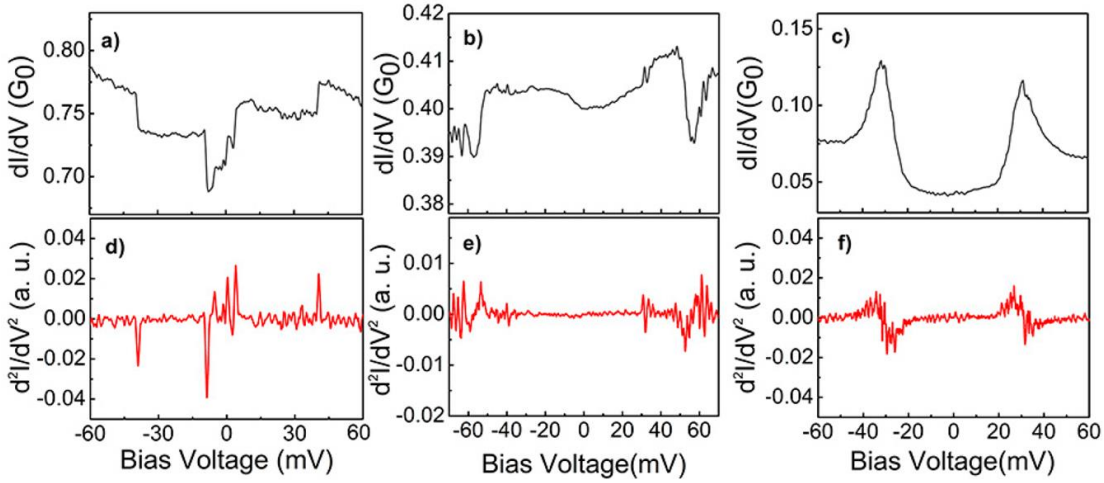

Figure 5.3. Examples of (a−c) *dI/dV* spectra and (d−f) corresponding differential spectra for (a, d) Au/H_2, (b,e) Ag/H_2, and (c,f) Cu/H_2 junctions.

The differential conductance (*dI/dV*) curves were investigated for Au/H_2, Ag/H_2 and Cu/H_2 junctions, showing conductance values of 0.01−1 G_0 for a fixed electrode separation. Figure 5.3 displays the *dI/dV* curves and their derivatives for Au/H_2, Ag/H_2 and Cu/H_2 junctions. Symmetric peaks in the derivatives were found around ±33 and ±42 meV for the Au and Ag/H_2 junctions, respectively. The conductance enhancement and reduction in the *dI/dV* curves can be explained by the excitation of a vibrational mode [5]. For Cu/H_2 junctions, symmetrical peaks were observed in the *dI/dV* curves at around ±35 meV, which can be explained by the abrupt switching between two slightly different local geometric configurations induced by phonon excitation. The energies of the peaks in the *dI/dV* curves provide the vibrational energies of the single-molecule junctions and have been utilized for the vibrational spectroscopy of single-molecule junctions [22]. More than 15 *dI/dV* spectra were collected for each metal. Vibrational modes were observed for all systems around 30-40 meV. Because the phonon modes of the clean metals are below 20 meV [23], the observed features correspond to vibrational modes between a hydrogen molecule and metal electrodes, which confirmed that a hydrogen molecule bridged the gaps between the Au, Ag, and Cu electrodes.

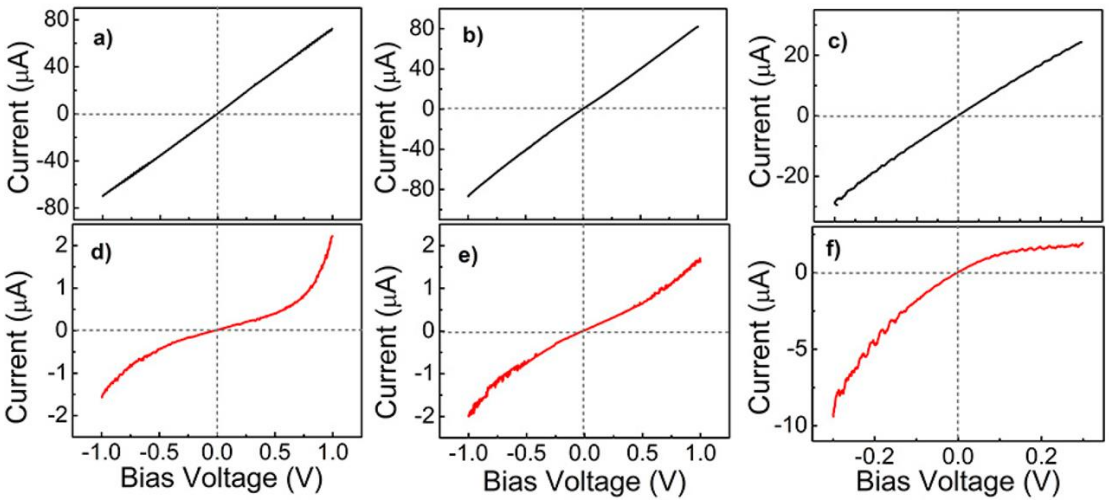

Figure 5.3 Typical $I-V$ characteristics for clean (a) Au, (b) Ag, and (c) Cu atomic contacts and (d) Au/H_2, (e) Ag/H_2 and (f) Cu/H_2 junctions.

To discuss the symmetry of the single hydrogen molecular junction, we measured the $I-V$ characteristics for Au/H_2, Ag/H_2 and Cu/H_2 junctions. Figure 5.3 shows typical $I-V$ characteristics for clean Au, Ag, and Cu atomic contacts, as well as for Au/H_2, Ag/H_2, and Cu/H_2 junctions. Linear symmetric $I-V$ characteristics were obtained for clean metal atomic contacts. The single hydrogen molecular junctions provided nonlinear and asymmetric $I-V$ characteristics [24-25]. An increase in the applied bias voltage brings the chemical potential of the electrode closer to the level of the molecular orbital leading to the steep increase in the charge flow across the junction. Now, we focus on the symmetry of the $I-V$ characteristics. Symmetric $I-V$ characteristics were observed for Au/H_2 and Ag/H_2 junctions, while asymmetric $I-V$ characteristics were observed for Cu/H_2 junctions. Similar $I-V$ characteristics were observed for more than three samples for each junction. In the case of a single-molecule junction with a symmetric molecule, the electric field is uniform in the molecule when the molecule symmetrically binds to the metal electrodes and the metal−molecule couplings are the same at both ends of the molecule. Symmetric $I-V$ characteristics are obtained for symmetric single-molecule junctions. Meanwhile, asymmetric $I-V$ characteristics are obtained when the molecule asymmetrically binds to the metal electrodes. The previously reported theoretical studies revealed that the difference in the potential drops and/or metal−molecule couplings cause the asymmetry of the $I-V$ characteristics of a single-molecule junction [20, 26]. When the molecule asymmetrically binds to metal electrodes, the potential drop at the molecule−metal interface is larger and the metal−molecule coupling is weaker for the electrode where the interaction between that molecule and the metal is weaker. Therefore, the asymmetric $I-V$ characteristics of Cu/H_2 junctions suggest that the interaction between the metal and the molecule should be asymmetric, which implies the formation of an asymmetric single-molecule junction.

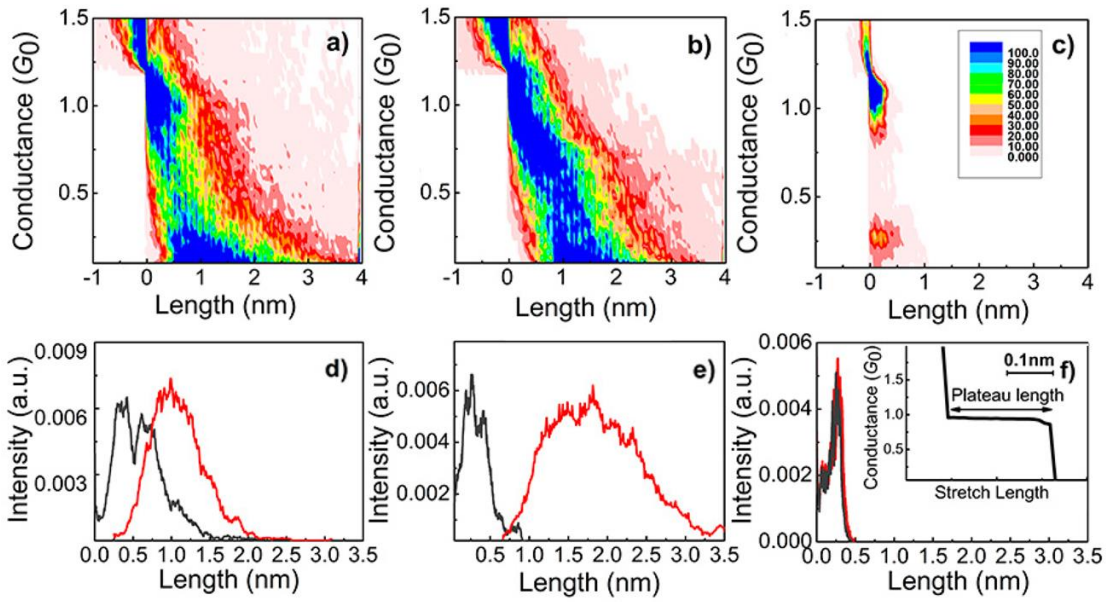

Figure 5.4 (a−c) Two-dimensional conductance histograms for (a) Au, (b) Ag, and (c) Cu contacts after the introduction of hydrogen and (d−f) length histograms for (d) Au, (e) Ag, and (f) Cu contacts before (black lines) and after (red lines) the introduction of hydrogen. The inset in panel f shows a typical conductance trace for Cu contacts after the introduction of hydrogen

The length of the single hydrogen molecular junctions was evaluated by statistical analysis of the conductance traces. Panels a−c of Figure 5.4 show the 2D conductance histograms of Au, Ag, and Cu contacts, respectively, after the introduction of hydrogen. These histograms were generated by identifying the first data point that had a conductance value lower than 1.2 G_0 and assigning it as a relative distance of $z = 0$ for each trace and then overlapping all of the individual traces in 2D space. Large counts were observed in the region of $1G_0$ for all cases. For the Au and Ag contacts, the features extended more than 1 nm, together with the decrease in the conductance values. For Cu contacts, the 1 G_0 feature extended within 0.3 nm, and small counts appeared around 0.3 G_0, corresponding to single molecule junctions. Panels d−f of Figure 5.4 show the length histograms of the single-atom or -molecule junctions for Au, Ag, and Cu contacts, respectively, before and after the introduction of hydrogen. The length of the single-atom or -molecule junctions was defined as the distance between the points at which the conductance dropped to the range of 0.04−1.1 G_0. Before the introduction of hydrogen, the Au atomic wire extended to 1.5 nm, and a sequence of peaks was observed in the length histogram. The interval of the peaks was 0.255 nm, which corresponds to the Au−Au distance of a clean Au atomic wire [10]. In contrast, the Ag and Cu atomic contacts broke within 0.5 nm, indicating that metal atomic wires were not formed for the Ag and Cu contacts. These results agree with previously reported results [27-28]. After the introduction of hydrogen, the lengths of the single-atom or -molecule junctions extended further compared to those for the clean Au and Ag contacts. On the other hand, the length of the single-atom or –molecule junction did not change before and after the introduction of hydrogen for the Cu contacts. An atomic wire was not formed for Cu contacts after the introduction of hydrogen. The average lengths were 0.58, 0.45, and 0.13 nm for clean Au, Ag, and Cu contacts, respectively, and 0.82, 1.60, and 0.24

nm for Au/H_2, Ag/H_2 and Cu/H_2 junctions, respectively.

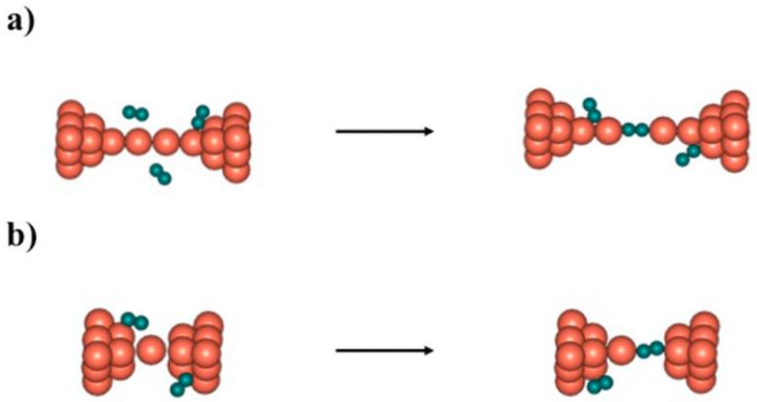

Figure 5.5 Formation processes of single hydrogen molecular junctions a) symmetric Au/H_2 and Ag/H_2 junctions are formed after the metal atomic wire is broken and b) an asymmetric Cu/H_2 junction is formed after the metal atomic contact is broken.

Here, we discuss the origin of the formation of the symmetric Au/H_2 and Ag/H_2 junctions and asymmetric Cu/H_2 junctions based on the experimental results in the length histograms (Figure 5.4). A single hydrogen molecular junction is formed by the following process: (1) A metal atomic wire or contact breaks; (2) hydrogen molecules diffuse onto the surface of the metal electrodes; and (3) a single hydrogen molecule is trapped between the metal electrodes, forming the single hydrogen molecular junction. In the case of Au/H_2 and Ag/H_2 junctions, metal atomic wires formed (Figure 5.5a, left). After the metal atomic wires broke, protruding single metal atoms remained on the surface of both metal electrodes. Then, a single hydrogen molecule bound to the protruding Au (Ag) atoms on the metal electrodes, leading to locally symmetric metal−molecule contacts (i.e., symmetric single hydrogen molecular junctions), as shown in Figure 5.5a (right). In the case of Cu/H_2 junctions, no metal atomic wire formed. After the metal contact (not a wire) broke, one Cu atom remained on the surface at either side of the metal electrodes, whereas the surface of the other side of the metal electrode was rather smooth without any protruding single metal atom, as shown in Figure 5.5b. The hydrogen adsorbed on an atop site on the protruding surface and on various adsorption sites (atop, bridge, hollow) on the rather flat surface. Therefore, locally asymmetric single hydrogen molecular junctions formed for the Cu/H_2 system.

Finally, we briefly comment on the conductance behaviors of the single hydrogen molecular junctions. The Au/H_2 junctions provided a broad feature below 1 G_0 in the conductance histogram. The Ag/H_2 junctions also provided a broad feature below 1 G_0, together with a decrease in the conductance value of the 1 G_0 peak. For Cu/H_2 junctions, a sharp peak of the H_2 molecular junction appeared at 0.3 G_0 in the conductance histogram, but the intensity of the 1 G_0 peak did not change, in contrast with the behavior of the Au/H_2 and Ag/H_2 junctions. When the interaction between the metal contacts and the molecule is strong, the single-molecule junction can take various atomic configurations, whereas only most energetically favorable structure can be formed when the metal−molecule interaction is moderate [29]. Because the conductance of a single molecule junction depends on its

atomic configuration, a strong interaction provides a broad feature in the conductance histogram. The appearance of broad features below 1 G_0 for Au/H_2 and Ag/H_2 junctions and a sharp peak at 0.3 G_0 for Cu/H_2 junctions indicates that the interactions between the hydrogen molecule and the metal contacts were large for Au and Ag contacts and moderate for Cu contacts. Comparison of the $1G_0$ features in the conductance histograms of Au/H_2, H_2/ Ag, and Cu/H_2 junctions suggests that the interactions between the hydrogen molecule and the Ag, Au, and Cu contacts decrease in this order. The large interaction of the Ag contacts can be explained by the decrease in the coordination number of the atoms of the contacts. Ag contacts formed atomic wires, as verified by the length analysis (Figure 5.4e), and the coordination number of the atoms in the metal wire was small. Because the reactivity of a metal increases with decreasing coordination number, the reactivity increased for the Ag atomic wires. The strongly interacting hydrogen molecules acted as scattering centers for conduction electrons. The conductance of the Ag atomic contact (1 G_0 peak) decreased because of this scattering process. A similar decrease in the conductance value was observed for Au atomic contacts decorated with hydrogen atoms.

5.4 Conclusion

We have investigated single hydrogen molecular junction with Au, Ag, and Cu electrodes using the mechanically controllable break junction technique at 10 K. Conductance measurements and differential conductance spectroscopy showed the bridging of hydrogen molecules between the metal electrodes. The current−voltage characteristics of the single hydrogen molecular junctions showed the formation of asymmetric Cu/H_2 junctions and symmetric Au/H_2 and Ag junctions. The symmetry of the single hydrogen molecular junction was discussed based on the length of the single-molecule junction. Statistical analysis of the lengths of the single-molecule junctions showed the formation of single atomic or molecular wire for Au/H_2 and Ag/H_2 junctions and the lack of formation of wires for Cu/H_2 junctions. By breaking Au and Ag atomic wires, protruding single metal atoms were prepared on the surface of both metal electrodes. A single hydrogen molecule bound to the protruding Au (Ag) atoms to form single molecule junctions with symmetric metal−molecule contacts at both ends. The Cu contact broke without metal wire formation, which caused the formation of structurally asymmetric electrodes with protruding and flat surfaces. Hydrogen adsorbed on an atop site on the protruding electrode and on various sites (atop, bridge, hollow) on the flat electrode to form single-molecule junctions with asymmetric metal−molecule contacts.

Reference

1. Aviram, A.; Ratner, M. A. Molecular Rectifiers. *Chem. Phys. Lett.* **1974**, 29, 277−283.
2. Reed, M. A.; Zhou, C.; Muller, C.; Burgin, T.; Tour, J. Conductance of a Molecular Junction. *Science*, **1997**, 278, 252−254.
3. Xu, B.; Tao, N. J. Measurement of Single-Molecule Resistance by Repeated Formation of Molecular Junctions. *Science*, **2003**, 301, 1221− 1223.

4. Venkataraman, L.; Klare, J. E.; Nuckolls, C.; Hybertsen, M. S.; Steigerwald, M. L. Dependence of Single-Molecule Junction Conductance on Molecular Conformation. *Nature* **2006**, 442, 904− 907.
5. Song, H.; Kim, Y.; Jang, Y. H.; Jeong, H.; Reed, M. A.; Lee, T. Observation of Molecular Orbital Gating. *Nature* **2009**, 462, 1039− 1043.
6. Hong, W.; Manrique, D. Z.; Moreno-Garcia, P.; Gulcur, M.; Mishchenko, A.; Lambert, C. J.; Bryce, M. R.; Wandlowski, T. Single Molecular Conductance of Tolanes: Experimental and Theoretical Study on the Junction Evolution Dependent on the Anchoring Group. *J. Am. Chem. Soc.*, **2012**, 134, 2292−2304.
7. Perrin, M. L.; Frisenda, R.; Koole, M.; Seldenthuis, J. S.; Gil, J. A. C.; Valkenier, H.; Hummelen, J. C.; Renaud, N.; Grozema, F. C.; Thijssen, J. M.; *et al*. Large Negative Differential Conductance in Single-Molecule Break Junctions. *Nat. Nanotechnol.* **2014**, 9, 830−834.
8. Haiss, W.; Wang, C. S.; Grace, I.; Batsanov, A. S.; Schiffrin, D. J.; Higgins, S. J.; Bryce, M. R.; Lambert, C. J.; Nichols, R. J. Precision Control of Single-Molecule Electrical Junctions. *Nat. Mater.* **2006**, 5, 995−1002.
9. Kiguchi, M.; Kaneko, S. Single Molecule Bridging between Metal Electrodes. *Phys. Chem. Chem. Phys.* **2013**, 15, 2253−2267.
10. Cuevas, J. C.; Scheer, E. Molecular Electronics: An Introduction to Theory and Experiment; World Scientific Publishing Co. Pte. Ltd.: Singapore, **2010**.
11. Smit, R.; Noat, Y.; Untiedt, C.; Lang, N.; Van Hemert, M.; Van Ruitenbeek, J. Measurement of the Conductance of a Hydrogen Molecule. *Nature* **2002**, 419, 906−909.
12. Kiguchi, M.; Stadler, R.; Kristensen, I.; Djukic, D.; Van Ruitenbeek, J. Evidence for a Single Hydrogen Molecule Connected by an Atomic Chain. *Phys. Rev. Lett.* **2007**, 98, 146802.
13. Csonka, S.; Halbritter, A.; Mihály, G.; Shklyarevskii, O.; Speller, S.; Van Kempen, H. Conductance of Pd-H Nanojunctions. *Phys. Rev. Lett.* **2004**, 93, 016802.
14. Kiguchi, M.; Hashimoto, K.; Ono, Y.; Taketsugu, T.; Murakoshi, K. Formation of a Pd Atomic Chain in a Hydrogen Atmosphere. *Phys. Rev. B* **2010**, 81, 195401.
15. Nakazumi, T.; Kiguchi, M. Formation of Co Atomic Wire in Hydrogen Atmosphere. J. *Phys. Chem. Lett.* **2010**, 1, 923−926.
16. Shu, C.; Li, C.; He, H.; Bogozi, A.; Bunch, J.; Tao, N. Fractional Conductance Quantization in Metallic Nanoconstrictions under Electrochemical Potential Control. *Phys. Rev. Lett.* **2000**, 84, 5196− 5199.
17. Kiguchi, M.; Konishi, T.; Murakoshi, K. Conductance Bistability of Gold Nanowires at Room Temperature. *Phys. Rev. B* **2006**, 73, 125406.
18. Matsushita, R.; Kaneko, S.; Nakazumi, T.; Kiguchi, M. Effect of Metal-Molecule Contact on Electron-Vibration Interaction in Single Hydrogen Molecule Junction. *Phys. Rev. B* **2011**, 84, 245412.
19. Djukic, D.; Van Ruitenbeek, J. Shot Noise Measurements on a Single Molecule. *Nano Lett.* **2006**, 6, 789−793.
20. Hirose, K.; Kobayashi, N. Effects of Atomic-Scale Contacts on Transport Properties through Single Molecules − *Ab Initio* Study. *Surf. Sci.* **2007**, 601, 4113−4116.
21. Nakazumi, T.; Kaneko, S.; Kiguchi, M. Electron Transport Properties of Au, Ag, and Cu Atomic Contacts in a Hydrogen Environment. *J. Phys. Chem. C* **2014**, 118, 7489−7493.

22. Kiguchi, M.; Nakazumi, T.; Hashimoto, K.; Murakoshi, K. Atomic Motion in H2 and D2 Single-Molecule Junctions Induced by Phonon Excitation. *Phys. Rev. B* **2010**, 81, 045420.
23. Naidyuk, Yu. G.; Yanson, I. K. Point-Contact Spectroscopy; Springer-Verlag: New York, **2005**.
24. Ho Choi, S.; Kim, B.; Frisbie, C. D. Electrical Resistance of Long Conjugated Molecular Wires. *Science* **2008**, 320, 1482−1486.
25. Matsuhita, R.; Horikawa, M.; Naitoh, Y.; Nakamura, H.; Kiguchi, M. Conductance and Sers Measurement of Benzenedithiol Molecules Bridging between Au Electrodes. *J. Phys. Chem. C* **2013**, 117, 1791−1795.
26. Zhang, G.; Ratner, M. A.; Reuter, M. G. Is Molecular Rectification Caused by Asymmetric Electrode Couplings or by a Molecular Bias Drop? *J. Phys. Chem. C* **2015**, 119, 6254−6260.
27. Smit, R. H. M.; Untiedt, C.; Yanson, A. I.; van Ruitenbeek, J. M. Common Origin for Surface Reconstruction and the Formation of Chains of Metal Atoms. *Phys. Rev. Lett.* **2001**, 87, 266102.
28. Bahn, S. R.; Jacobsen, K. W. Chain Formation of Metal Atoms. *Phys. Rev. Lett.* **2001**, 87, 266101.
29. Kaneko, S.; Nakazumi, T.; Kiguchi, M. Fabrication of a Well- Defined Single Benzene Molecule Junction Using Ag Electrodes. *J. Phys. Chem. Lett.* **2010**, 1, 3520−3523.

Chapter 6

Atomic and Electronic Structures of a Single Oxygen Molecular Junction with Au, Ag, and Cu Electrodes

6.1 Introduction

Since the physical limitation of silicon-based semiconductors has been anticipated [1–3], researchers started to look for the alternative solutions. Utilization of single atoms or molecules as active components in electronic devices is one of the promising ways. In 1974, the first theoretical consideration of the single molecular diode was reported by Aviram and Ratner, where donor and acceptor units are connected with the insulating unit [4]. Thanks to the development of the measurement techniques, including mechanically controllable break junctions (MCBJ) and scanning tunneling microscopy (STM)-BJ techniques, the electrical conductance of the single atom or molecule can be measured experimentally [5–11]. Currently, various functionalities have been reported for single atomic and molecular junctions, where a single atom or molecule is bridged between metal electrodes.[10, 12–15].

While there have been enormous studies of the single molecular junctions with a variety of molecules, the atomic and electronic structures of the single molecular junction were not fully characterized with experimental techniques. The atomic structure of the single molecular junctions has been discussed by comparing the experimentally obtained conductance values with the theoretical values obtained using possible model structures in most of the studies. To overcome the difficulty in identifying the atomic structures in the molecular junctions, some experimental methods have been applied to the simplest molecular junctions of atomic and molecular hydrogen. The atomic structure of the Pt/H_2 junction was fully characterized by point contact spectroscopy, inelastic electron tunneling spectroscopy (IETS), shot noise, and conductance fluctuation measurements, together with the theoretical calculations. These measurements revealed that the single hydrogen molecule bridges between Pt electrodes with its molecular long axis parallel to the junction axis. The single hydrogen molecular junctions with other metals have been also well characterized with these techniques [16]. The next candidate system is the single oxygen molecular junction. The oxygen molecule is a simple and small molecule, which makes measurements easy to compare with more complex molecular systems. In addition, the interaction between the oxygen molecule and metal atomic contacts provides the basic understanding of the oxidation process of the metal surface. Despite these interests, atomic structure and electronic properties of the single oxygen molecular junction have not been fully characterized. The conductance measurements suggested the formation of the atomic wire containing the oxygen molecules for the Au, Ag and Cu/O_2 junctions [17]. However,

oxygen incorporation into the atomic wires has not been directly detected with some spectroscopic techniques. The atomic and electronic structures of the single oxygen junction have not been clear up to now. In the present study, we investigated atomic and electronic structures of the Au/O_2, Ag/O_2, and Cu/O_2 junctions using conductance, IETS, and current−voltage ($I-V$) response measurements. The length analysis of the junction in the conductance measurement revealed the formation of the atomic wire. The IETS and $I-V$ response measurements confirmed the bridging of the oxygen molecule between metal electrodes. The $I-V$ response provided the information about the electronic structure of the Au/O_2, Ag/O_2 and Cu/O_2 junctions. The symmetric $I-V$ responses together with other experimental results confirmed the formation of the atomic wire containing the oxygen molecules.

6.2 Experimental

Experiment was performed in the ultrahigh vacuum (UHV) at low temperature (10 K) using the MCBJ setup [16, 18-19]. The notched Au, Ag, and Cu wires (0.10 mm in diameter) were fixed with epoxy adhesive (Stycast, 2850FT) on the top of the electrically insulated phosphor bronze substrate with polyimide tape. By bending the substrate using a three-point bending configuration in a custom-made vacuum pot, the metal wire was broken at the notched part. During the whole measurement, the metal wire was repeatedly broken and made contact using the piezo element. Oxygen was introduced into the metal contacts through a heated capillary. All DC two-point voltage-biased conductance measurements were performed under a bias voltage of 100 mV. The differential conductance was measured using a standard lock-in technique with AC modulation at 1 mV and 7.777 kHz. The conductance was monitored at a fixed contact configuration during the DC bias between −100 and +100 mV. The $I-V$ responses were measured by sweeping the bias voltage, which started from 100 mV, increased to +1.0 V, decreased to −1.0 V, and returned to the initial value. The sweep rate of the $I-V$ response measurements was 100 kHz. The electrodes' separation was fixed during the $I-V$ response measurement.

6.3 Results and discussion

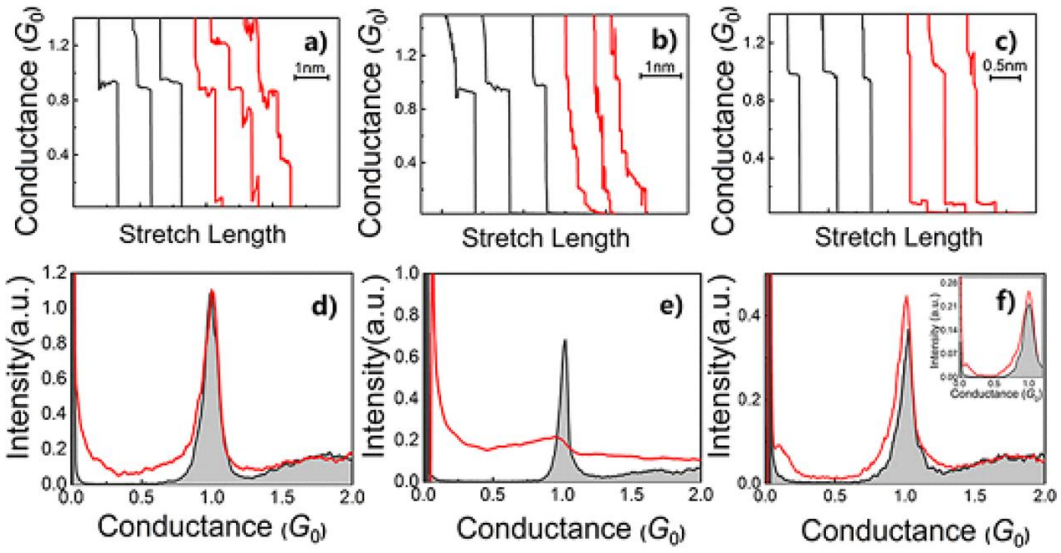

Figure 6.1. Examples of conductance traces for (a) Au, (b) Ag, (c) and Cu junctions and conductance histograms of (d) Au, (e) Ag, and (f) Cu junctions before (black line and gray filling) and after (red line) introduction of oxygen under the bias voltage at 100 mV. The inset figure is the magnification of the conductance histogram at low conductance regime in (f). All the conductance histograms were constructed without data selection from more than 1000 traces during a breaking process of the metal contacts. The intensity of the conductance histograms was normalized by the number of traces. The bin size is 0.004 G_0.

Figure 6.1 shows the typical conductance traces and conductance histograms of Au, Ag and Cu junctions before and after introduction of oxygen. The intensity of the conductance histograms was normalized with the number of the conductance traces. For the pure metal contact, conductance plateaus appeared at 1 G_0 ($G_0 = 2e^2/h$) in the conductance traces, and clear 1 G_0 peaks appeared in the conductance histograms, which indicated the formation of metal atomic junctions [17,20]. After the introduction of oxygen, conductance plateaus appeared below 1 G_0 in the conductance traces, and features appeared below 1 G_0 in the corresponding conductance histograms. Among Au, Ag, and Cu junctions, the change in the shape of the conductance histograms before and after the introduction of oxygen was the largest for the Ag junction. The 1 G_0 peak was suppressed, a continuous broad feature appeared below 1 G_0 for the Ag/O_2 junction; while the 1 G_0 peaks were still clear for the Au/O_2 and Cu/O_2 junctions. The suppression of the 1 G_0 peak for the Ag/O_2 junction and little change in the shape of the conductance histogram for the Au/O_2 junction agreed with the previously reported study [17]. In the case of the Cu/O_2 junctions, a weak but broad peak (conductance distribution) appeared around 0.1 G_0 in the conductance histogram, indicating the formation of the preferential atomic configurations with the conductance around 0.1 G_0. While the conductance behavior due to the introduction of oxygen varied with the choice of the metals, a similar tendency of conductance steps below 1 G_0 in the conductance traces and similar distribution below 1 G_0 in the conductance histograms appeared for all Au/O_2, Ag/O_2 and Cu/O_2 junctions. These experimental results indicated

the formation of the single oxygen molecular junctions.

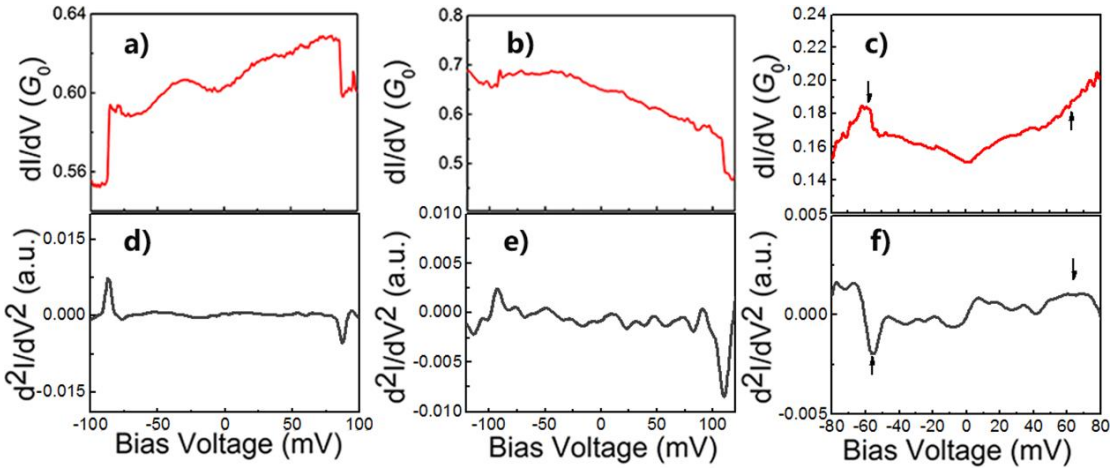

Figure 6.2. Examples of differential conductance and its derivative for (a, d) Au/O_2, (b, e) Ag/O_2, and (c, f) Cu/O_2 junctions.

The formation of the single oxygen molecular junctions was verified by IETS. Figure 6.2 displays examples of differential conductance and its derivative for Au/O_2, Ag/O_2 and Cu/O_2 junctions. Symmetric peaks are found in d^2I/dV^2 curves around ±90 meV, ±100 meV, and ±60 meV for Au/O_2, Ag/O_2 and Cu/O_2 junctions, respectively. The conductance enhancement and reduction in *dI/dV* curves are explained by the excitation of a vibration mode. Around 20 curves were collected for each junction with zero-bias conductance of 0.01−1.2 G_0, in order to determine the average vibrational energy. The average vibrational energy was 85, 106, and 69 meV for Au/O_2, Ag/O_2 and Cu/O_2 junctions, respectively. Since the energy of the phonon modes for clean metal contact is below 20 meV [21-22], the observed modes correspond to vibrational modes between oxygen atom/molecule and metal electrodes, which indicated the interaction between oxygen atom/molecule and Au, Ag and Cu electrodes.

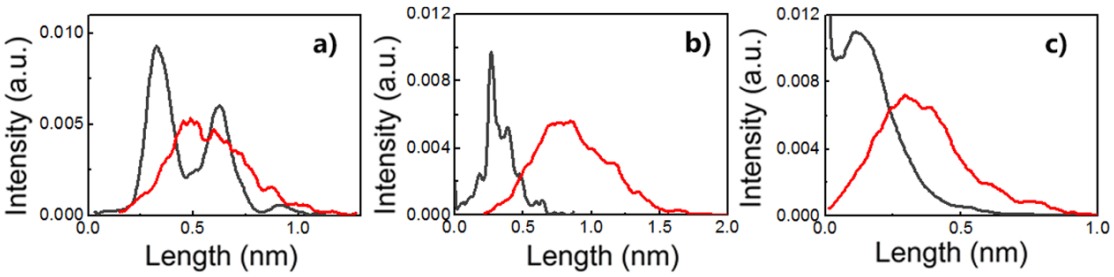

Figure 6.3. Length histograms of the last plateaus for (a) Au, (b) Ag, and (c) Cu junctions before (black) and after (red) introduction of oxygen.

In order to obtain information on the structure of the Au/O_2, Ag/O_2 and Cu/O_2 junctions, the plateau length was analyzed for the conductance traces during the junction breaking process (Figure 6.3) [16]. The plateau length was defined as the distance between the points at which the conductance dropped below 1.2 G_0 and 0.04 G_0. Here, we defined the threshold conductance values in order to evaluate the length of the junction including the metal

atomic wire and oxygen. For the clean Au junction, the plateau extended to 1.5 nm, and a sequence of peaks were observed in a length histogram of the Au contact, which indicated the formation of the Au atomic wire [20]. In contrast, the clean Ag and Cu junctions broke within 0.5 nm, indicating the formation of the short atomic contact (not a wire). The average plateau length was 0.55 ± 0.07 nm for Au, 0.34 ± 0.14 nm for Ag, and 0.19 ± 0.05 nm for Cu junctions. The obtained results for the clean Au, Ag and Cu junctions agreed with the previously reported results [22-23]. After introduction of oxygen, the Au junctions showed no obvious change in the length, while Ag and Cu junctions showed a drastic change. The atomic junction could be extended to 0.8 nm even for the Ag and Cu junctions. The average plateau length was 0.75, 0.86, and 0.44 nm for the Au/O_2, Ag/O_2 and Cu/O_2 junctions, respectively. Considering the interatomic distance of Au, Ag and Cu (~0.25 nm) [20], the present results showed the formation of the atomic wires for all Au/O_2, Ag/O_2 and Cu/O_2 junctions.

Here, we briefly comment on the reason why the Au/O_2, Ag/O_2 and Cu/O_2 junctions formed atomic wires. The formation of the atomic wire requires relatively strong metal−metal bonds in the wire compared to metal bonds in the base part of the electrodes (bulk) [22-23]. In general, the metal−metal bond becomes stronger with the decrease in the coordination number of neighboring atoms. Since all atoms in the metal atomic wire are at surface, the metal−metal bond within the wire is stronger than that in the bulk. It is known that the ratio of bond strength between atomic wire and bulk increases in the order 3d < 4d < 5d metals [22-23]. In the case of 5d metals (Au, Pt, and Ir), the metal−metal bond within the wire is much stronger than that in bulk, thus, pure Au and also the Au/O_2 junctions form atomic wires. The atomic or molecular adsorption could further stabilize the atomic wire by the decrease in the surface energy of the atomic wire [20,24]. Therefore, the atomic wire formed for the Ag/O_2 and Cu/O_2 junctions. The wire formation could affect the conductance behavior during the elongation process of the junctions. As shown in the previous section, a clear 0.1 G_0 peak was observed in the conductance histogram only for the Cu/O_2 junction (Figure 6.1). This can be explained by the formation of a shorter metal wire for the Cu/O_2 junction. The electric conductance is suppressed by the atomic or molecular adsorption on the metal atomic wire [25-27]. The decrease in conductance value of the wire depends on the amount of atom or molecule adsorbed on the wire [28-29]. The Au/O_2 and Ag/O_2 junctions were much longer than the Cu/O_2 junctions. For the longer Au and Ag wires, there are many available adsorption sites (area) for the oxygen adsorption. Thus, the Au/O_2 and Ag/O_2 junctions could show various conductance values depending on the number of atoms or molecules adsorbed, which caused a broad feature in the conductance histogram. In contrast, the Cu/O_2 junction formed only a short wire, and there are less available adsorption sites on the wire surface. The effect of the atomic and molecular adsorption would not be so large for the Cu/O_2 junction, which leads to a sharp peak in the conductance histogram.

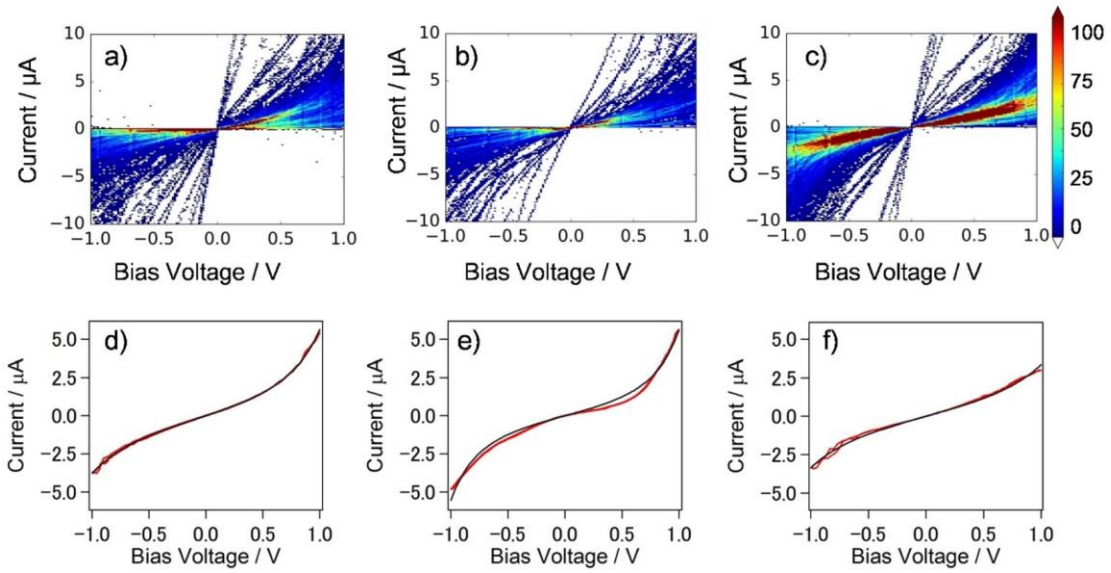

Figure 6.4. (a−c) Distribution and (d−f) examples of *I−V* responses of (a,d) Au/O_2, (b,e) Ag/O_2 and (c,f) Cu/O_2 junctions. The total number of I− V responses was 130, 71, and 293 for a) Au/O_2, b) Ag/O_2 and c) Cu/O_2 junctions, respectively, and the bin size is 16 mV ×100 nA. The red lines are experimental I−V responses, and black ones are fitting results.

We then investigated the electronic structures of the single oxygen molecular junction by analysis in the *I-V* responses of the Au/O_2, Ag/O_2 and Cu/O_2 junctions. Figure 6.4 a-c shows histograms and examples of the *I-V* responses for the Au/O_2, Ag/O_2 and Cu/O_2 junctions. Within the single channel transport model, the transmission probability of a single molecular junction is represented by

$$\tau(E) = \frac{4\Gamma_L\Gamma_R}{(\Gamma_L+\Gamma_R)^2+(\mathrm{E}-\varepsilon_0)^2} \qquad \text{Eq.6.1}$$

where ε_0 and $\Gamma_{L(R)}$ are the energy of the conduction orbital and the electronic coupling between the molecule and the metal electrode, respectively. At 0 K, the current through the molecular junction is written by

$$I(V) = \frac{2e}{h}\int_{-\infty}^{\infty} dE\ \tau(E,V)[\,f_L(E) - f_R(E)] \qquad \text{Eq.6.2}$$

where *f* is the Fermi distribution function. When electronic temperature, *T*, is set to 0 K, **Eq. 6.2** can be analytically described as

$$I(V) = \frac{8e}{h}\alpha(1-\alpha)\Gamma\left\{\arctan\left(\frac{\alpha eV-\varepsilon_0}{\Gamma}\right) + \arctan\left(\frac{(1-\alpha)eV+\varepsilon_0}{\Gamma}\right)\right\} \qquad \text{Eq.6.3}$$

where $\Gamma = \Gamma_L + \Gamma_R$ and $\alpha = \Gamma_L / \Gamma$. By fitting the experimental results with Eq.6.3, asymmetric factor α, energy of the conduction orbital ε_0, and the electronic coupling ($\Gamma_L + \Gamma_R$) could be obtained [30]. The fitting results are shown by black curves in Figure 4 and are listed in Table 6.1. The ε_0 was around 0.5 eV, and the Γ was around 130 meV for the Cu/O_2 junction. Since the number of the *I-V* responses were not so large, it is hard to discuss the difference of these values among the Au/O_2, Ag/O_2 and Cu/O_2junctions. It is clear that the electronic coupling for the Au/O_2, Ag/O_2 and Cu/O_2 junctions are larger compared with other typical single molecular junctions [30-31]. The electronic coupling was 60 meV for the single molecular junction with both benzenedithiol (BDT) and bipyridine (BPY). The energy of the conduction orbital was 0.59 eV and 1.2 eV for single BDT and

BPY molecular junctions, respectively [30-31]. The conductance of the single BDT and BPY molecular junction was 0.01 G_0 and 6 $\times 10^{-4}$ G_0, which were smaller than the conductance of the Au/O_2, Ag/O_2 and Cu/O_2 junctions (~0.1 G_0). The larger electronic couplings lead to the higher conductance values for the Au/O_2, Ag/O_2 and Cu/O_2 junctions. The asymmetric factor was around 0.5 (i.e., symmetric coupling) for the Au/O_2, Ag/O_2 and Cu/O_2 junctions, suggesting formation of symmetric molecular junctions.

Table 6.1. Energy of the Conduction Orbital (ε_0), the Electronic Coupling between the Molecule and the Metal Electrode ($\Gamma_L + \Gamma_R$), and $\alpha=\Gamma_L/\Gamma$ for Au/O_2, Ag/O_2 and Cu/O_2 junctions

	ε_0 (eV)	$\Gamma_L + \Gamma_R$ (meV)	α
Au/O_2	0.70	130	0.54
Ag/O_2	0.59	100	0.50
Cu/O_2	0.51	130	0.51

It is noted that the asymmetric factor α was close to 0.50, indicating the symmetric coupling of the junction with respect to left and right metal electrodes. In our previous study for Au/H_2, Ag/H_2, Cu/H_2 junctions [16], symmetric *I-V* responses were observed when longer single atomic or molecular wires were formed, while asymmetric *I-V* responses were observed when the longer wire was not formed. In this study, the plateau length analysis revealed that longer atomic wires were formed for all Au/O_2, Ag/O_2 and Cu/O_2 junctions, and symmetric *I-V* responses were observed, which agreed with the previously reported results. When a metal atomic wire is broken, protruded single metal atoms are remained on the surface of the both metal electrodes. The single oxygen molecule binds to the protruded metal atoms on metal electrodes, leading to the locally symmetric metal-molecule contacts, and symmetric *I-V* response.

6.4 Conclusion

We have investigated the atomic and electronic structures of the single oxygen molecular junctions with the Au, Ag and Cu electrodes. The single molecular junction was fabricated with the MCBJ technique at low temperature (10 K). The conductance profiles obtained during break-junction measurements showed the formation of the atomic wire. The bridging of the oxygen molecule between metal electrodes was confirmed by the inelastic electron tunneling spectroscopy and $I-V$ responses. The $I-V$ responses also provided the information about the energy difference between conduction orbital and Fermi level of the metal electrodes, the strength of the metal−molecule coupling, and symmetry of the junctions. The large strength of the metal−molecule coupling explained the higher conductivity of the single oxygen molecular junction. The obtained symmetric $I-V$ responses could be explained by the formation of the atomic wire. These systematic experimental investigations confirmed the formation of metal atomic wire containing the oxygen molecules for the Au/O_2, Ag/O_2 and Cu/O_2 junctions.

Reference

1. Packan, P. A. Pushing the Limits. *Science* **1999**, 285, 2079−2081.
2. Taur, Y.; Buchanan, D. A.; Chen, W.; Frank, D. J.; Ismail, K. E.; Lo, S.-H.; Sai-Halasz, G. A.; Viswanathan, R. G.; Wann, H.-J. C.; Wind, S. J. Cmos Scaling into the Nanometer Regime. *Proc. IEEE* **1997**, 85, 486−504.
3. Keyes, R. W. Fundamental Limits of Silicon Technology. *Proc. IEEE* **2001**, 89, 227−239.
4. Aviram, A.; Ratner, M. A. Molecular Rectifiers. *Chem. Phys. Lett.* **1974**, 29, 277−283.
5. Konishi, T.; Kiguchi, M.; Takase, M.; Nagasawa, F.; Nabika, H.; Ikeda, K.; Uosaki, K.; Ueno, K.; Misawa, H.; Murakoshi, K. Single Molecule Dynamics at a Mechanically Controllable Break Junction in Solution at Room Temperature. *J. Am. Chem. Soc.* **2012**, 135, 1009−1014.
6. Kaneko, S.; Murai, D.; Marqués-González, S.; Nakamura, H.; Komoto, Y.; Fujii, S.; Nishino, T.; Ikeda, K.; Tsukagoshi, K.; Kiguchi, M. Site Selection in Single-Molecule Junction for Highly Reproducible Molecular Electronics. *J. Am. Chem. Soc.* **2016**, 138, 1294−1300.
7. Kiguchi, M.; Konishi, T.; Murakoshi, K. Hydrogen-Assisted Stabilization of Ni Nanowires in Solution. *Appl. Phys. Lett.* **2005**, 87, 043104.
8. Xu, B.; Tao, N. J. Measurement of Single-Molecule Resistance by Repeated Formation of Molecular Junctions. *Science* **2003**, 301, 1221− 1223.
9. Venkataraman, L.; Klare, J. E.; Nuckolls, C.; Hybertsen, M. S.; Steigerwald, M. L. Dependence of Single-Molecule Junction Conductance on Molecular Conformation. *Nature* **2006,** 442, 904−907.
10. Moreno-García, P.; La Rosa, A.; Kolivoška, V.; Bermejo, D.; Hong, W.; Yoshida, K.; Baghernejad, M.; Filippone, S.; Broekmann, P.; Wandlowski, T. Charge Transport in C60-Based Dumbbell-Type Molecules: Mechanically Induced Switching between Two Distinct Conductance States. *J. Am. Chem. Soc.* **2015**, 137, 2318−2327.
11. Smit, R.; Noat, Y.; Untiedt, C.; Lang, N.; van Hemert, M. v.; Van Ruitenbeek, J. Measurement of the Conductance of a Hydrogen Molecule. *Nature* **2002**, 419, 906−909.
12. Song, H.; Kim, Y.; Jang, Y. H.; Jeong, H.; Reed, M. A.; Lee, T. Observation of Molecular Orbital Gating. *Nature* **2009**, 462, 1039− 1043.
13. Kiguchi, M.; Ohto, T.; Fujii, S.; Sugiyasu, K.; Nakajima, S.; Takeuchi, M.; Nakamura, H. Single Molecular Resistive Switch Obtained Via Sliding Multiple Anchoring Points and Varying Effective Wire Length. *J. Am. Chem. Soc.* **2014**, 136, 7327−7332.
14. Fujii, S.; Tada, T.; Komoto, Y.; Osuga, T.; Murase, T.; Fujita, M.; Kiguchi, M. Rectifying Electron-Transport Properties through Stacks of Aromatic Molecules Inserted into a Self-Assembled Cage. *J. Am. Chem. Soc.* **2015**, 137, 5939−5947.
15. Díez-Pérez, I.; Hihath, J.; Lee, Y.; Yu, L.; Adamska, L.; Kozhushner, M. A.; Oleynik, I. I.; Tao, N. Rectification and Stability of a Single Molecular Diode with Controlled Orientation. *Nat. Chem.* **2009**, 1, 635−641.
16. Li, Y.; Kaneko, S.; Fujii, S.; Kiguchi, M. Symmetry of Single Hydrogen Molecular Junction with Au, Ag, and Cu Electrodes. *J. Phys. Chem. C* **2015**, 119, 19143−19148.
17. Thijssen, W.; Strange, M.; aan de Brugh, J.; van Ruitenbeek, J. Formation and Properties of

Metal−Oxygen Atomic Chains. *New J. Phys.* **2008**, 10, 033005.
18. Li, Y.; Demir, F.; Kaneko, S.; Fujii, S.; Nishino, T.; Saffarzadeh, A.; Kirczenow, G.; Kiguchi, M. Electrical Conductance and Structure of Copper Atomic Junctions in the Presence of Water Molecules. *Phys. Chem. Chem. Phys.* **2015**, 17, 32436−32442.
19. Kiguchi, M.; Murakoshi, K. Conductance of Single C60 Molecule Bridging Metal Electrodes. *J. Phys. Chem. C* **2008**, 112, 8140−8143.
20. Kiguchi, M.; Konishi, T.; Murakoshi, K. Conductance Bistability of Gold Nanowires at Room Temperature. *Phys. Rev. B* **2006**, 73, 125406.
21. Cuevas, J. C.; Scheer, E. Molecular Electronics: An Introduction to Theory and Experiment; World Scientific Publishing Co. Pte. Ltd.: Singapore, **2010**.
22. Bahn, S. R.; Jacobsen, K. W. Chain Formation of Metal Atoms. *Phys. Rev. Lett.* **2001**, 87, 266101.
23. Smit, R.; Untiedt, C.; Yanson, A.; Van Ruitenbeek, J. Common Origin for Surface Reconstruction and the Formation of Chains of Metal Atoms. *Phys. Rev. Lett.* **2001**, 87, 266102.
24. Kiguchi, M.; Murakoshi, K. Fabrication of Stable Pd Nanowire Assisted by Hydrogen in Solution. *Appl. Phys. Lett.* **2006**, 88, 253112.
25. Barnett, R. N.; Häkkinen, H.; Scherbakov, A. G.; Landman, U. Hydrogen Welding and Hydrogen Switches in a Monatomic Gold Nanowire. *Nano Lett.* **2004,** 4, 1845−1852.
26. Novaes, F. D.; da Silva, A. J.; da Silva, E. Z.; Fazzio, A. Effect of impurities in the large Au-Au distances in gold nanowires. *Phys. Rev. Lett.* **2003**, 90, 036101.
27. Jelínek, P.; Pérez, R.; Ortega, J.; Flores, F. Hydrogen Dissociation over Au Nanowires and the Fractional Conductance Quantum. *Phys. Rev. Lett.* **2006**, 96, 046803.
28. Kiguchi, M.; Konishi, T.; Hasegawa, K.; Shidara, S.; Murakoshi, K. Three Reversible States Controlled on a Gold Monoatomic Contact by the Electrochemical Potential. *Phys. Rev. B* **2008**, 77, 245421.
29. Kiguchi, M.; Stadler, R.; Kristensen, I.; Djukic, D.; Van Ruitenbeek, J. Evidence for a Single Hydrogen Molecule Connected by an Atomic Chain. *Phys. Rev. Lett.* **2007**, 98, 146802.
30. Matsuhita, R.; Horikawa, M.; Naitoh, Y.; Nakamura, H.; Kiguchi, M. Conductance and Sers Measurement of Benzenedithiol Molecules Bridging between Au Electrodes. *J. Phys. Chem. C* **2013**, 117, 1791−1795.
31. Adak, O.; Korytár, R.; Joe, A. Y.; Evers, F.; Venkataraman, L. Impact of Electrode Density of States on Transport through Pyridine- Linked Single Molecule Junctions. *Nano Lett.* **2015**, 15, 3716−3722

Chapter 7

Photo-driven reactions excited in Cu/H_2O contacts

7.1 Introduction

As mentioned in former sections, our final goal is to achieve photo-driven chemical reaction in the nano junction with MCBJ technique. In present work, we focus on the water splitting reaction, $2H_2O \rightarrow 2H_2+O_2$. The water dissociation reaction is important in our daily, as an essential reaction with offering the hydrogen with energy from clean and cheap reactant, water. Besides, this reaction is relevant to three simple modeling molecules, which were evident that posses different electron transport properties as we discussed in the former chapters. The target reaction has been reported conventionally excited by electrification, photoexcitation, thermal methods with metallic complexes catalysts systems [1]. However, the widely investigated catalysts system, mainly concentrated on TiO_2 and its derivatives are useful but not effective and economical. For better performance, the Au, Ag nano structure were added to improve the efficiency of the water hydrolysis with their unique plasmonic characteristics [2-3]. From then, the plasmon resonance generated in the nano structures has been discussed. Years of effort, the experimental evidenceof plasmon induced reaction were observed. Mubeen *et al*. reported an autonomous photocatalyst device working rely on the surface plasmons only [4]. Their device based on an Au nanorod capping with TiO_2 layer obtained a good stability and efficiency in the water splitting reaction. Their study performed a plasmonic nano metallic structure, which inspired the present work with the similar conditions, in specifically, metallic nano structure, where is potential for plasmon resonance.

Based on the fundamental studies in previous chapters, the Cu nano electrodes has been considered as the promising photocatalyst for water molecule. Actually, the Cu plays important role in water dissociation reaction for a long time inverstigation [5]. However, in the most cases, the Cu could not work rely on itself only, due to the instability of the plasmonic properties than the Au, Ag and absence of the proper band gap like TiO_2 [3-6]. On the other hands, the external stimulations required in the previous catalysts system to offer enough energies for the reaction, such as heat, electrical power [6-7]. Neither the expensive materials mixed nor the consumption of the power are not fit for the commercial application in the further developing of the Cu participate catalyst system. In this chapter, we will settle with these issue for exploiting Cu nano junction as photocatalysts system. Copper nanoelectrode, which takes advantages of the localized surface plasmon resonance (LSPR), convenience to fabricate and low cost, is an ideal photocatalyst for water photo-driven reaction.

In the current work, we investigate the photo-driven reaction of water molecule in the

Cu nano junctions in a UHV at 10K. Under the *UV-vis* irradiation, the conductance and IETS measurements revealed that the water splitting in the Cu nano junctions. The mechanism of the reaction will be discussed on the wavelength dependence of the reaction in the Cu-H_2O system by conductance behavior.

7.2 Experimental

The experiments were investigated in the ultra-high vacuum (UHV) condition with mechanically controllable break junction (MCBJs) technique at 10K. The substrate was prepared with a series of electron beam lithography (EBL) technique [8]. Briefly, the phosphor bronze covered by an insulating polyimide layer, the Cu electrodes fabricated by physical evaporate deposition (PVD) method. The whole substrate (shown as Fig.7.1) was fixed by a three-point bending configuration in a custom-made vacuum pot. The Cu nanoelectrodes were broken at the notch by bending of the substrate with piezoelement. Water was introduced onto the metal contacts through a capillary with heating. The conductance was monitored for a fixed contact configuration during the dc bias between −100 to +100 mV. The differential conductance was measured using a standard lock-in technique with ac modulation at 1 mV and 7.777 kHz.

7.3 Results and discussion

7.3.1 Chemical reaction in the Cu/H_2O junctions

The break process of the contact operates dependent on the behavior of the piezoelement. When the piezoelement goes up to stretch the Cu electrodes, the junction break. Then goes down and the electrodes reconnect, the break and reconnection process defined as one cycle. Every cycle, only one conductance trace can be recorded. Every conductance histogram contains over 1000 conductance traces without any selection in the current work. Due to the advantage of the UHV conditions with MCBJ, we would achieve a stable and long lifetime junction during the break processes. The conductance histogram of Cu, Cu-water and Cu-water contact shown in Fig. 7.1. For the bare Cu electrodes (Fig.7.1a), a 1 G_0 ($G_0=2e^2/h$) peak was observed, which derived from a Cu atomic contact [9]. Figure 7.2b displays the Cu contact with water present. The water molecule was introduced via the capillary connected to molecule container with pre-heating for 30 minutes. In the conductance histogram, a fraction peak that located around 0.1 G_0 was observed. This result has a good agreement with our previous work [10]. Figure 7.1c displayed the Cu/H_2O contacts with *UV-vis* (>200 nm) illumination. The Cu/H_2O contact has been exposed to the irradiation in wavelength larger than 200 nm for 60 mins. As the Fig. 7.3c performs, an additional peak around 0.2 G_0 was obtained and the 0.1 G_0 peak increased. As conference, the conductance histograms of Cu/H_2 and Cu/O_2 junctions are also illustrated in fig. 7.1d, e.

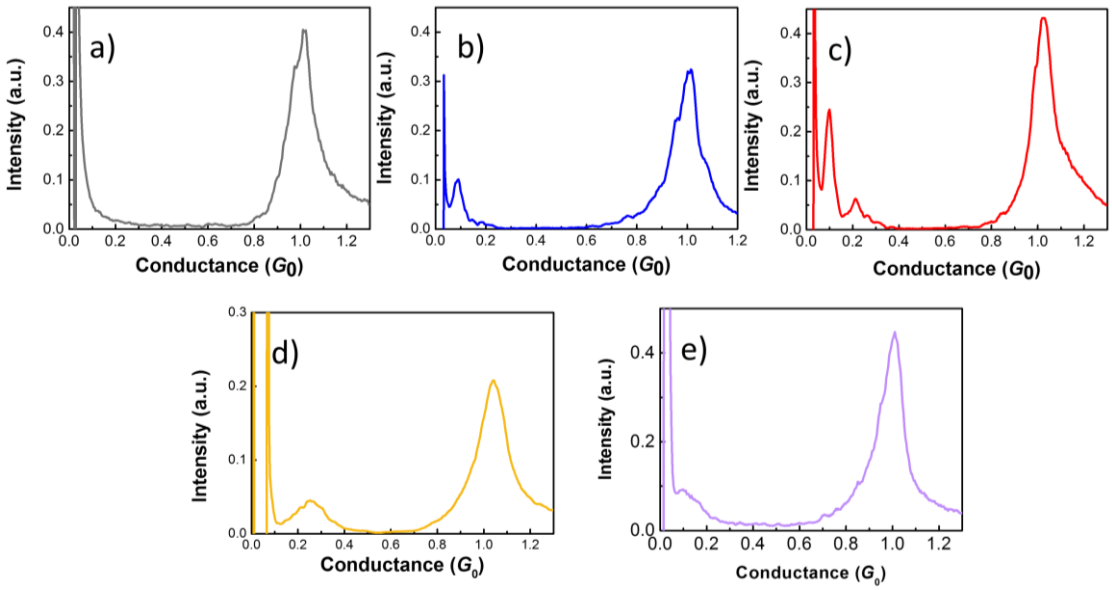

Figure 7.1 Examples of conductance traces for (a) Cu (b) Cu-H_2O and (c) Cu-H_2O junctions irradiated by *UV-vis* light and as reference (d) Cu-H_2 (e) Cu-O_2 junctions under the bias voltage at 100 mV. All the conductance histograms were constructed without data selection from more than 1000 traces during a breaking process of the metal contacts. The intensity of the conductance histograms is counts normalized by the number of traces. The bin size is 0.004 G_0.

Varieties of effects have impact on the electron tunneling through the nano junction, leading the conductance behavior change, like molecular species, structure, orientation etc. Thus, in order to understand the change caused by the irradiation, the vibration modes were investigated *via* inelastic electron tunneling spectroscopy (IETS), the results shows in Fig. 7.2. The *dI/dV* spectra for Cu/H_2O contact without illumination (Fig.7.2a, b, colored in blue) exhibit symmetric peaks located around ±55 meV and ± 150 meV, more clear peak can be seen in its derivative spectra (Fig.7.3 d, e, blue). The *dI/dV* curve displayed the conductance under 0.5 G_0 with an "step-up" shape above the zero bias, which is conventional shape in *dI/dV* curves interpreted as a one-level mode [11]. In contrast, as the Figure 7.2 c, f shows the typical *dI/dV* curves represent photoexcitated Cu/H_2O system. In a higher conductance regime, smaller symmetric peaks were observed around ±40 meV with step-down shape. The IETS gave the information of the changes in the nano contact. Generally, two aspects were considered, one is the value of the vibration energy. The vibration energies are quite separated before and after the *UV-vis* light excitation. The typical higher vibration mode were observed before illumination, ±55 meV and ± 150 meV, which corresponding to "free OH" and Cu-H mode of H_2O-Cu system, respectively [12-13]. With exposure of the *UV-vis* illumination, the vibration energy that observed around ±40 meV, derived from Cu/H_2 contact, this result has high consistency with the results reported in former work [14]. Besides, the other side has been considered is the shape of the *dI/dV* spectra with irradiation. With one molecule mode, the "step-up" and "step-down" shape divided by the 0.5 G_0 or minimal cross [15]. In specific, smaller than 0.5 G_0 shows "step-up", otherwise, "step-down". However, it is a special feature has been obtained only in H_2/metal contacts, which has been proved experimentally "step-up" shape were observed below 0.5 G_0 [15-16].

Thus, we speculated the hydrogen molecule has generated possibly.

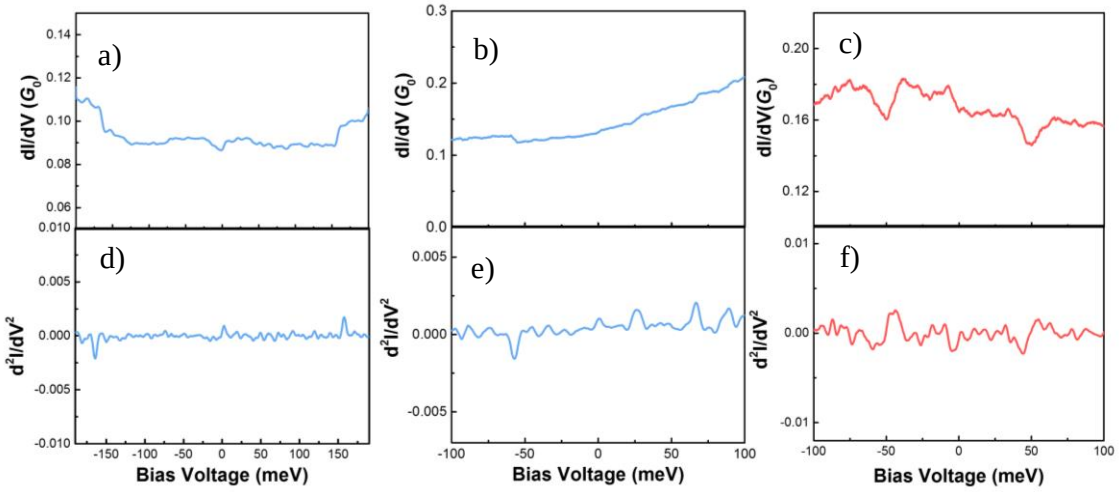

Figure 7.2 Typical *dI/dV* spectra and its derivative measured via inelastic electron tunneling spectroscopy (IETS) method of H_2O/Cu junctions, before (a, b, d, e, shown in blue) and after (c, f, shown in red) the *UV- vis* irradiation (>200 nm).

Real-time IETS has been investigated for clarify the dynamics process *in-situ* in the junction with *UV-vis* irradiation. The real-time IETS was obtained by fixed the electrodes and kept measuring continuously. Figure 7.3a performs one time real-time IETS, which expressed as conductance varies as the function of time, short for *C-t* plot here. The black dots are the conductance at zero bias of the *dI/dV* spectra. One cycle start defined as the 0.1 G_0 contact was fabricated in IETS spectra controlled by the piezoelement to the junction break. The cycle has been recorded lasts from 1 mins to about 2h, depended on the inner situation of the contacts under evaluation. The conductance variation versus time, shows the dynamic of the reaction in the Cu/H_2O nano contacts with irradiation. At the beginning, the conductance stuck around 0.1 G_0 regime with altering slightly. After exposure about 1h, the conductance changed suddenly to a higher conductance (the yellow arrow marked), furthermore, this value kept stable over 40 minutes. Besides, the vibration energy has been considered, shown in Fig.7.3b, c, also, marked in the Fig.7.3a. The conductance possesses continuity, while the vibrational energy did not. As the principle described in section 1.4.2.3, the electron tunnels the junction via elastic and inelastic channels. Only the electron through the inelastic channel can be observed in IETS. However, the conductance at zero bias will not be influenced. The vibration energy at beginning was seen around ±100 meV, which had been calculated as the libration mode of water reacted with Cu surface [13]. Along the conductance increase, the vibration mode differed, as the Fig.7.3c shows, the peaks were observed around ±40 meV, which might be the Cu/H_2 vibration mode, as we reported before [5].

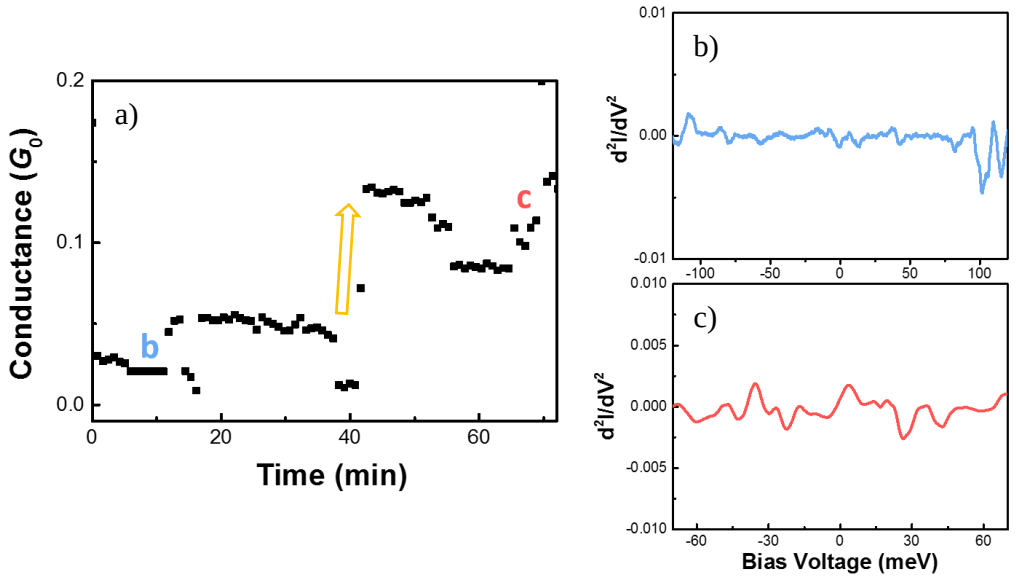

Figure 7.3 a) The vibration energy vary as the function of time with electrified at 100 mV, b) IETS at b point in figure a, c) IETS at c point in figure a.

7.3.2 Mechanism of the water decomposition reaction utilizing Cu contacts

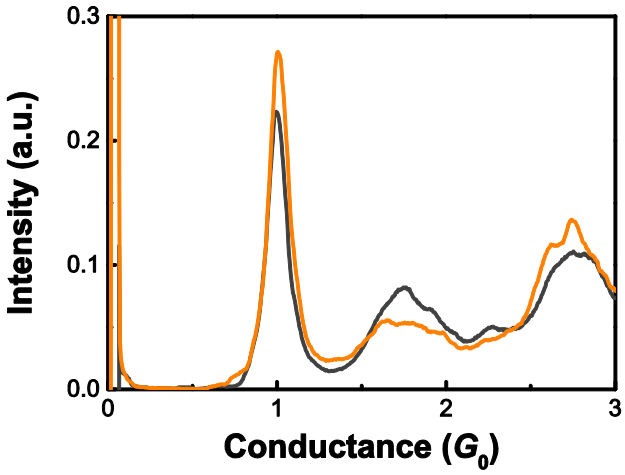

Figure 7.4 Examples of conductance traces for Cu junctions irradiated by *UV-vis* irradiation at 100 mV. The intensity of the conductance histograms is counts normalized by the number of traces. The bin size is 0.004 G_0.

Next, the mechanism of the experimental realities observed in conductance behavior and vibration mode variation in the previous section will be discussed. Firstly, as a control experiment, the bare Cu contact has been irradiated under the *UV-vis* illumination (> 200 nm) over 60 mins, the result shown in figure 7.4. Without the water molecules present, after the irradiation, there is no noticeable changes observed in conductance histogram for Cu contact. According to this reality, the illumination did not affect the Cu atomic contact conductance behavior. Similarly, electrify and subsequent thermal effects can be excluded by the previous work in chapter 3 and 4. All the measurements for Cu contact operate

under the same UHV at 10K condition, with H_2O molecules introduced into the chamber but without illumination. The minor peak located around 0.2 G_0 did not obtain.

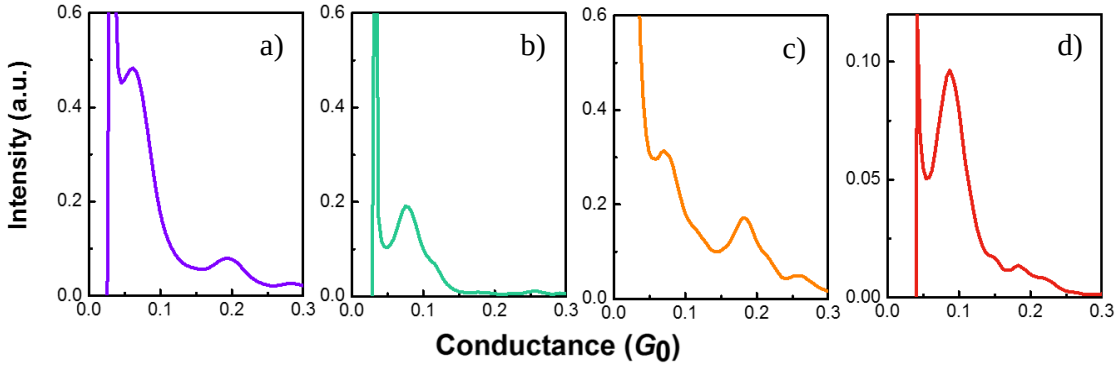

Figure 7.5 Illustrations of conductance histograms for (a) Cu-H_2O-400 nm (b) Cu-H_2O-500 nm, (c) Cu-H_2O-600nm and (d) Cu-H_2O-700nm irradiation at 100 mV. All the conductance histograms were constructed without data selection from more than 1000 traces during a breaking process of the metal contacts. The intensity of the conductance histograms is counts normalized by the number of traces. The bin size is 0.004 G_0.

Main concern in the present system is the photoexcitation process in the Cu/H_2O contact. Numerous previous theoretical and practical evidences of the optical response related to the Cu nanoparticles has been investigated [17-18]. As well known, the photoelectric properties of the noble metal are dependent on the wavelength of the incident illumination [19]. However, the light source used in former section has a wide range of wavelength, which providing too much information. Therefore, we estimate the conductance behavior of Cu/H_2O contact with the irradiation in separated rang of wavelength, the conductance histograms showed in Fig. 7.5. The color correspond to the wavelength of the incident irradiation, which shown in purple, green, orange and red for 400, 500, 600 and 700 nm, respectively, only colored for distinguish. With the illumination, the similar conductance properties were observed with 400 nm, 600 nm and 700 nm. In specific, the minor 0.2 G_0 peak obtained after exposure to the light. In contrast, with exposure under 500 nm over 1 hour, the conductance histogram did show much difference. These results were confirmed for repeating the experiments. The evaluation time is the same as the previous work. The mechanism based on the wavelength dependence will be discuss in the later section.

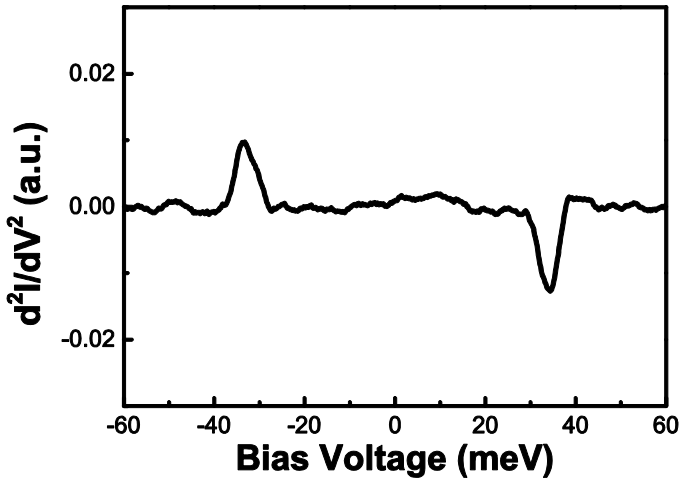

Figure 7.6 Typical differential *dI/dV* spectra of H_2O/Cu junctions with irradiation (700 nm).

The differential of typical *dI/dV* curve with 700 nm irradiation was shown in Figure 7.6. Symmetrical peak were observed around ±35 meV. The vibration mode is corresponding to the Cu/H_2 like we discussed in the last section. With conductance properties and vibration behavior revealed the excitation of the reaction in the Cu/H_2O contact.

Here, we briefly comment on the reaction processes of the present work. The procedure for the light irradiated reaction in the Cu/H_2O system was illustrated in figure 7.7. In specific, the Cu-H_2O photocatalysis system working principles can be concluded as following:

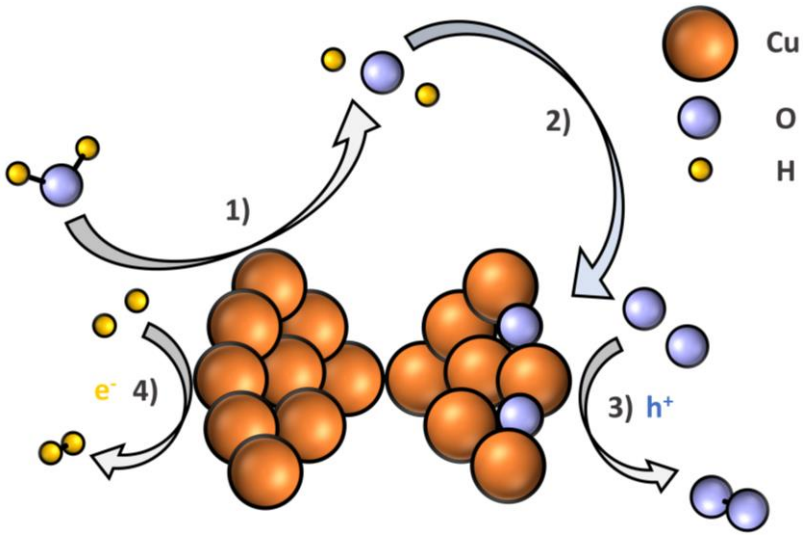

Figure 7.7 Schematic of the mechanism of the water dissociation reaction in the Cu/H_2O irradiation system.

1) The adsorption of the water molecule onto the Cu surface or into the nano junction, with few decomposed into O* and H*;

2) The O* reconstructed with the Cu electrodes surface to form Cu/$Cu_\chi O$ structure;

3, 4) More H* and O* generate subsequently, the H* obtained electron to form H_2 on the Cu surface while the O* transfer electron to hole on the $Cu_\chi O$ side into O_2.

The formation of Cu/$Cu_\chi O$ structure is unexpected but reasonable and essential in the reaction processes. Here, the origin of the Cu/$Cu_\chi O$ structure will be discussed. Obviously, the water provided the O atom. In specific, the H_2O decomposed, the O atom generated

and reconstructed the Cu surface. Therefore, let us consider the dissociation of the intact water molecule on the bare Cu surface. Firstly, water was introduced into the chamber in UHV condition through the capillary. Then, the intact water molecule adsorbed on the Cu surface and dissociated into OH and H at low temperature because the forward reaction is exothermic on the Cu surface, with reaction energies ΔE about -0.12 eV [20]. The similar result has been observed by STM image directly at 6K [21]. Also, the IETS measurement shown in fig.7.2b, e confirmed the "free OH" existed experimentally. But then the next, the dissociation subsequent, in specifically, the OH* decomposed into O* and H* reaction is endothermic, it calls for energy to satisfy the reaction energy ΔE about 0.55 eV [20]. This step hinder the water to decompose completely. Hence, we did not obtain any experimental evidence to show the water splat completely before irradiation. In contrast, with the illumination, any of the light sources we exploit can offer sufficient energy to excite the water to decompose, leading to evolution of O*. The O* binds strongly on Cu, since this reaction is also exothermic [20]. Hereto, the Cu/$Cu_\chi O$ structure has been constructed.

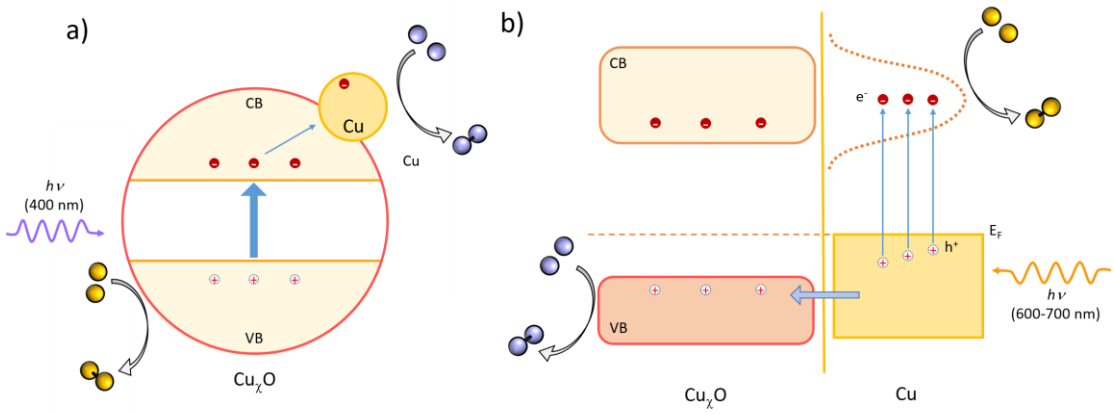

Figure 7.8 Schematic of the mechanism of the water dissociation reaction in the Cu/H_2O photocatalysis system a) $Cu_\chi O$ photoexcitation mechanism with Cu nanoparticles acting as co-catalysts to provide additional surface sites via the trapping of electrons, b) Cu_n plasmon working principle with $Cu_\chi O$ structure, CB, conduction band; VB, valence band; E_F, Fermi level.

In the subsequent H_2 and O_2 generation, the Cu/$Cu_\chi O$ conformation plays important roles. Here, the mechanism of this structure will be commented briefly, the main working principles were illustrated in figure 7.9. Considered the dependence of the wavelength, two separated mechanisms attribute to the Cu-H_2O photocatalysis reactions. The photoexcited produce at 400 nm drove by the $Cu_\chi O$ with Cu acting as co-catalysts (fig.7.8a), and the reaction excited under 600-700 nm illumination rely on Cu_n (fig. 7.8b). First, the $Cu_\chi O$ is p-type semiconductor, which can be excited under 500 nm under exposure [22-23]. Besides, the $Cu_\chi O$ regarding as photocatalyst for water decomposition reaction due to its separation by a band gap energy of 2.0-2.2 eV reported before [24-25]. Specifically, the electron in the valence band was excited to the conduction band around 400 nm, the electrons go subsequently to Cu side and denoting to H_2 generation. The Cu existence is essential here, for improving charge separation, reported as "inter-particle

electron transfer" [26]. On the other hand, the Cu_n structure has plasmon resonance in a range of 670-760 nm with $Cu_\chi O$ present [27-28]. As shown in figure 7.8b, the hot electron (e^-) generated by the Cu_n plasmon resonance excited to the plasmon level along with left a positive hole (h^+) on the surface. The hot electron-hole pair works separately in Cu and $Cu_\chi O$ surface respectively. Subsequently, more H* and O* were generated by water decomposition, then H* obtained electron on the Cu side to form H_2 while the O* got hole on the $Cu_\chi O$ side to form.

Generally, the incident light in current investigation contribute significantly to the reaction in 3 aspects. To drive the H_2O decompose completely, to excite the $Cu_\chi O$ at 400 nm and drive the Cu_n plasmon at 600-700 nm. Cushing *et al*. reported the similar structure as photocatalyts [23]. In the present work, not only the $Cu_\chi O$ photo-induce but also the Cu_n plasmon mechanisms can generate the electron-hole pair and transferred to the $Cu/Cu_\chi O$ surface to drive the photocatalysis.

7.4 Conclusion

In this chapter, we explored the photochemical reaction, particularly, water photo-driven reaction in the Cu contacts excited by *UV-vis* light. The conductance histogram gave the evidence to show that electron transport properties of the Cu/H_2O contact changed with the irradiation. An additional peak was observed around 0.2 G_0 after excited by the *UV-vis* light. Vibration energies were investigated by IETS. The *dI/dV* curves and its differential spectra revealed that the ±40 meV with conductance located around 0.2 G_0 at zero bias corresponding to Cu-H_2-Cu configuration. Moreover, the conductance and vibration energy vary continuously as the function of excitation time has been considered simulate. The results demonstrate the H_2 derived from the reaction with the *in-situ* measurements. With the wavelength dependence investigation of the Cu/H_2O photocatalyst system, the results demonstrated the photoexcited produce at 400 nm drove by the $Cu_\chi O$ with Cu acting as co-catalysts, and the reaction excited under 600-700 nm illumination rely on Cu_n plasmon resonance.

Reference

1. Zoulias, E.; Varkaraki, E.; Lymberopoulos, N.; Christodoulou, C. N.; Karagiorgis, G. N., A review on water electrolysis. *TCJST* **2004,** *4* (2), 41-71.
2. Gomes Silva, C. u.; Juárez, R.; Marino, T.; Molinari, R.; García, H., Influence of excitation wavelength (UV or visible light) on the photocatalytic activity of titania containing gold nanoparticles for the generation of hydrogen or oxygen from water. *J. Am. Chem. Soc.* **2010,** *133* (3), 595-602.
3. Ingram, D. B.; Linic, S., Water splitting on composite plasmonic-metal/semiconductor

photoelectrodes: evidence for selective plasmon-induced formation of charge carriers near the semiconductor surface. *J. Am. Chem. Soc.* **2011,** *133* (14), 5202-5205.
4. Mubeen, S.; Lee, J.; Singh, N.; Krämer, S.; Stucky, G. D.; Moskovits, M., An autonomous photosynthetic device in which all charge carriers derive from surface plasmons. *Nat. Nanotechol.* **2013,** *8* (4), 247-251.
5. Henderson, M. A., The interaction of water with solid surfaces: fundamental aspects revisited. *Surf. Sci. Rep.* **2002,** *46* (1), 1-308.
6. Nishijima, Y.; Ueno, K.; Kotake, Y.; Murakoshi, K.; Inoue, H.; Misawa, H., Near-infrared plasmon-assisted water oxidation. *J. Phys. Chem. Lett.* **2012,** *3* (10), 1248-1252.
7. Rodríguez, J. A.; Evans, J.; Graciani, J.; Park, J.-B.; Liu, P.; Hrbek, J.; Sanz, J. F., High Water− Gas Shift Activity in TiO2 (110) Supported Cu and Au Nanoparticles: Role of the Oxide and Metal Particle Size. *J. Phys. Chem. C* **2009,** *113* (17), 7364-7370.
8. Konishi, T.; Kiguchi, M.; Takase, M.; Nagasawa, F.; Nabika, H.; Ikeda, K.; Uosaki, K.; Ueno, K.; Misawa, H.; Murakoshi, K., Single molecule dynamics at a mechanically controllable break junction in solution at room temperature. *J. Am. Chem. Soc.* **2012,** *135* (3), 1009-1014.
9. Agraıt, N.; Yeyati, A. L.; Van Ruitenbeek, J. M., Quantum properties of atomic-sized conductors. *Phys. Rep.* **2003,** *377* (2), 81-279.
10. Li, Y.; Kaneko, S.; Fujii, S.; Nishino, T.; Kiguchi, M., Atomic structure of water/Au, Ag, Cu and Pt atomic junctions. *Phys. Chem. Chem. Phys.* **2017,** *19* (6), 4673-4677.
11. Paulsson, M.; Frederiksen, T.; Ueba, H.; Lorente, N.; Brandbyge, M., Unified description of inelastic propensity rules for electron transport through nanoscale junctions. *Phys. Rev. Lett.* **2008,** *100* (22), 226604.
12. Schiros, T.; Haq, S.; Ogasawara, H.; Takahashi, O.; Öström, H.; Andersson, K.; Pettersson, L. G.; Hodgson, A.; Nilsson, A., Structure of water adsorbed on the open Cu (110) surface: H-up, H-down, or both? *Chem. Phys. Lett.* **2006,** *429* (4), 415-419.
13. Ren, J.; Meng, S., First-principles study of water on copper and noble metal (110) surfaces. *Phys. Rev. B* **2008,** *77* (5), 054110.
14. Li, Y.; Kaneko, S.; Fujii, S.; Kiguchi, M., Symmetry of Single Hydrogen Molecular Junction with Au, Ag, and Cu Electrodes. *J. Phys. Chem. C* **2015,** *119* (33), 19143-19148.
15. Matsushita, R.; Kaneko, S.; Nakazumi, T.; Kiguchi, M., Effect of metal-molecule contact on electron-vibration interaction in single hydrogen molecule junction. *Phys. Rev. B* **2011,** *84* (24), 245412.
16. Kiguchi, M.; Nakazumi, T.; Hashimoto, K.; Murakoshi, K., Atomic motion in H_2 and D_2 single-molecule junctions induced by phonon excitation. *Phys. Rev. B* **2010,** *81* (4), 045420.
17. Guo, X.; Hao, C.; Jin, G.; Zhu, H. Y.; Guo, X. Y., Copper nanoparticles on graphene support: an efficient photocatalyst for coupling of nitroaromatics in visible light. *Angew. Chem. Int. Ed.* **2014,** *53* (7), 1973-1977.
18. Gartland, P.; Berge, S.; Slagsvold, B., Photoelectric work function of a copper single crystal for the (100),(110),(111), and (112) faces. *Phys. Rev. Lett.* **1972,** *28* (12), 738.
19. Kriegel, I.; Jiang, C.; Rodríguez-Fernández, J.; Schaller, R. D.; Talapin, D. V.; Da Como, E.; Feldmann, J., Tuning the excitonic and plasmonic properties of copper chalcogenide nanocrystals. *J. Am. Chem. Soc.* **2012,** *134* (3), 1583-1590.
20. Phatak, A. A.; Delgass, W. N.; Ribeiro, F. H.; Schneider, W. F., Density functional theory

comparison of water dissociation steps on Cu, Au, Ni, Pd, and Pt. *J. Phys. Chem. C* **2009,** *113* (17), 7269-7276.
21. Kumagai, T.; Kaizu, M.; Okuyama, H.; Hatta, S.; Aruga, T.; Hamada, I.; Morikawa, Y., Tunneling dynamics of a hydroxyl group adsorbed on Cu (110). *Phys. Rev. B* **2009,** *79* (3), 035423.
22. Pestryakov, A. N.; Petranovskii, V. P.; Kryazhov, A.; Ozhereliev, O.; Pfänder, N.; Knop-Gericke, A., Study of copper nanoparticles formation on supports of different nature by UV–Vis diffuse reflectance spectroscopy. *Chem. Phys. Lett.* **2004,** *385* (3), 173-176.
23. Cushing, S. K.; Li, J.; Meng, F.; Senty, T. R.; Suri, S.; Zhi, M.; Li, M.; Bristow, A. D.; Wu, N., Photocatalytic activity enhanced by plasmonic resonant energy transfer from metal to semiconductor. *J. Am. Chem. Soc.* **2012,** *134* (36), 15033-15041.
24. de Jongh, P. E.; Vanmaekelbergh, D.; Kelly, J. J., Cu 2 O: a catalyst for the photochemical decomposition of water? *Chem. Commun.* **1999,** (12), 1069-1070.
25. Kondo, J., Cu_2O as a photocatalyst for overall water splitting under visible light irradiation. *Chem. Commun.* **1998,** (3), 357-358.
26. Hu, C.-C.; Nian, J.-N.; Teng, H., Electrodeposited p-type Cu_2O as photocatalyst for H_2 evolution from water reduction in the presence of WO 3. *Sol. Energ. Mat. Sol.* **2008,** *92* (9), 1071-1076.
27. Chan, G. H.; Zhao, J.; Hicks, E. M.; Schatz, G. C.; Van Duyne, R. P., Plasmonic properties of copper nanoparticles fabricated by nanosphere lithography. *Nano Lett.* **2007,** *7* (7), 1947-1952.
28. Wu, L.; Zhou, X.; Bai, P., Plasmonic metals for nanohole-array surface plasmon field-enhanced fluorescence spectroscopy biosensing. *Plasmonics* **2014,** *9* (4), 825-833.

Chapter 8

General Conclusions

Since the molecular device has been proposed as a fancy dream in 50s last century in Feynman's speech. The low dimensional world kept attracting many attentions for decades due to the unique properties, like quantization, it possesses. With development of sophisticated technology in the nano scale investigation, today, we, human beings made the dream come true. More and more theoretical and experimental realities support that the molecular electronics will has its day in the near future. However, even great efforts has been made over 50 years, so many riddles are still waiting for us to uncover.

In this thesis, we explored chemical reaction in the nano junctions with mechanically controllable break junction (MCBJ) technique. All the experiments measured under the ultra-high vacuum (UHV) condition at 10K. UHV-MCBJ technique enables to offer the researches in this work a precise and reproducible condition.

Generally, the photo-driven reactions in metal/H_2O contacts has been focused on. Water and relevant reactions is essential in our daily life. The metal materials are regarded as conventional catalysts participated in the related reaction as many mechanism. However, in terms of the water splitting reaction, the prior catalysts system calling for high energy input and high cost needed to be alternated. Besides, photocatalyst has been developed due to its potential usage of the solar energy. Photo-induced metallic water splitting system was even proposed half century ago. The main photo water hydrolysis catalysts take advantage of the expensive and structure-complicated semiconductor-base system. With the nano technology developed, the nano metal structural plasmon resonance has been observed and applied to the solar energy water decomposition process. This idea provided a brand new mind to the photon-drive reaction.

On the other hands, take advantages of the localized surface plasmon resonance (LSPR), convenience to fabricate and investigation in nano scale, the metallic nano contacts has been considered as promising water photoncatalysis system. In this thesis, metallic nanoelectrodes has been fabricated as potential photocatalysts. With evaluation the electron transport and structure behavior in molecular level, the H_2O photo-driven reaction generated in the suitable nano junction.

For the photocatalsis the water dissociation reaction utilizing the nano junction structure, we endeavored in the fabrication, selection, optimization of the photo-driven catalyst system for water first. Furthermore, employing the system to run the water photoexcitation reaction. In specific, I studied as following:

At the beginning, we constructed available condition with MCBJ technique to investigate the electron transport properties and the structural information of the molecules relevant to the water splitting. First, we evaluated the electron transport properties of H_2O molecule with Au, Ag, Cu and Pt, totally for 4 metallic electrodes. All the metals we chose are able to

work in a principle of surface plasmon.

The conductance behavior indicated the formation of single water molecule junctions for the water–Au, Cu and Pt junction systems. The reaction strength were evaluated relied on the conductance histograms and plateau length histogram, in order of Pt>Cu>Au>Ag. With strong interplay of Pt, Cu with water attributed to obvious changes in the conductance behavior, on the other hand, the atomic chain offer more adsorption site of Pt enhanced the interaction strength. In contrast, absences of the atomic wire conformation lead Cu a well-defined peak in the conductance histogram. Oppositely, for the weak interactions between Au, Ag and water cases, the atomic chain leads the electrical transport properties in the nano junctions. Au atomic wire provides plenty of adsorption sites, achieve a slight change in the conductance behavior while without wire formation, Ag did not vary at all.

Next, we investigated the Cu/H_2O contacts in experimentally and theoretically. The 0.1 G_0 peak was simulated by the calculation demonstrate the water presence could enhance the Cu atomic configuration with a wire. This special structure exhibited as a specific conductance peaks in the conductance histogram.

Also, the products, H_2, O_2/metal contacts should be considered. Here, we choose the Au, Ag and Cu for concern about further application. With comprehensively investigate the conductance histogram, length histogram, inelastic electron tunneling spectrum (IETS), we confirmed the H_2 and O_2 bridge in the metallic contacts. Additionally, *I-V* characteristics reveal Cu/H_2 with ratification behavior. For the hydrogen, oxygen/ metal contacts, the Cu electrodes performed discernable. The Cu/H_2 possesses a around 0.3 G_0 peak, besides, Cu/O_2 peak was observed at 0.1 G_0. Additionally, the vibration modes in the junction measured by the IETS also show potential for reveal the reality happened in the nano junction. Until here, we established of the identifications system of the water decomposition reaction via conductance histogram and IETS. The further experiments would concentrate on the Cu/H_2O contacts.

Finally, rely on all the efforts we have done before, we explored the photochemical reaction, particularly, water photo-driven reaction in the Cu contacts excited by *UV-vis* light. The conductance histogram gave the evidence confirmed that electron transport properties of the Cu/H_2O contact changed with the irradiation. An additional peak was observed around 0.2 G_0 after excited by the *UV-vis* light. Vibration energies were investigated by IETS. The *dI/dV* curves and its differential spectra revealed that the ±40 meV with conductance located around 0.2 G_0 at zero bias corresponding to Cu-H_2-Cu configuration. Moreover, the conductance and vibration energy vary continuously as the function of excitation time has been considered simulate. The results demonstrate the H_2 derived from the reaction with the *in-situ* measurements. With the wavelength dependence investigation of the Cu/H_2O photocatalyst system, the results demonstrated the photoexcited produce at 400 nm drove by the $Cu_\chi O$ with Cu acting as co-catalysts, and the reaction excited under 600-700 nm illumination rely on Cu_n plasmon resonance.

As a summary, in this thesis, water decomposition reaction has been generated employed Cu nano electrodes. This finding demonstrated a high possibility of the single molecular junction becoming a powerful alternative solution of the current photocatalyst for water decomposition reaction. Additionally, the economical and easy-to-fabrication plasmonic

materials, like Cu we used in this thesis can be considered.

Besides, *in-situ* reaction monitoring method relied on the conductance and vibration energies has been put forward. With this method, the experimental evidences for the reactions dynamics in the nano contacts can be evaluated at molecular junction. The molecular level understanding is foundation of precise-manufacture for the nano-sized devices, is the first step for application. Therefore, this method would make contributions to the molecular devices in the near future.

Acknowledgements

Here, I want to express my deeply gratitude and respect to everyone I met during PhD course in Tokyo Institute of Technology. Without their direct or indirect help and care I could not finish this thesis.

I am so appreciate for my supervisor, Prof. Manabu Kiguchi (Tokyo Institute of Technology), who gave me a chance to be involved into the fascinating nano scale world. His profound understanding, forward-looking and great passion in this field encouraged me a lot. As well as the kindness and care for the daily life, therefore, I want to express deep appreciation to Pro Kiguchi. The same for Associated Prof. Tomoaki Nishino with his profession and amiability.

Also I would like to express many thanks to all of the collaborators in my investigation. They are Dr. Firuz Demir (Simon Fraser University), Dr. George Kirczenow (Simon Fraser University) and Dr. Alireza Saffarzadeh (Payame Noor University, Simon Fraser University) supported with the calculation of the Cu/H_2O system. Dr. Kazuhito Tsukagoshi (National Institute for Materials Science, Japan) gave technical support for the lithographic Cu nano electrodes fabrication. Dr. Shintaro Fujii and Dr. Satoshi Kaneko for the discussion in many work. Mr. Yuki Komoto supporting with the *I-V* fitting program for the metal/O_2 system.

Many thanks to members in the Kiguchi-Nishino Laboratory at Tokyo Institute of Technology. I had a great life here with Prof. Toshiaki Enoki, Ms. Tomoko Kuroiwa, Dr. Elena Bedogni, Dr. Santiago Marques-Gonzalez (Santi), Dr. Rjuji Matsushita (Matsushita Sensei), Mr. Daigo Murai, Mr. Ryoji Takahashi (Takashi), Ms. Madoka Iwane, Mr. Suzuki Sho (Shobi), Mr. Akira Aiba, Mr. Masato Koike, Mr. Takafumi Kosakai (Kozabi), Mr. Yuya Matsuzawa, Mr. Yuji Isshiki (Leader), Mr. Takanori Harashima (Pima), Mr. Ryo Murakami, Mr. Shuhei Watanabe, Ms. Yuechan Zhang, Ms. Risa Fukuzumi, Ms. Haruna Cho (Pocky), Mr. Syuji Kobayashi, Mr. Yusuke Hasekawa, and Mr. Toshihide Matsunaka. Lots of gratitude for everyone in Kiguchi-Nishino Lab. with everyday work, laugh together. Best wishes to everyone for wonderful days in the future.

As well, I would like to thanks for my family, friends with endless support always. My mother, father, twin sister and boyfriend. Thanks for them make me could decide what to do as I really want to without any hesitation. For all the friends sharing the misery and happiness with my PhD life in Japan.

My PhD course was supported financially by China Scholarship Council (CSC No.201406350072).

To all the endeavor I have done and everyone go into my life.

Yu Li
Tokyo, June 2017

List of Publications

Paper

1. **Li, Y**., Kaneko, S., Fujii, S. and Kiguchi, M., Symmetry of Single Hydrogen Molecular Junction with Au, Ag, and Cu Electrodes. *J. Phys. Chem. C* , *119*, 33, (2015).19143-19148.
2. **Li, Y.**, Demir, F., Kaneko, S., Fujii, S., Nishino, T., Saffarzadeh, A., Kirczenow, G. and Kiguchi, M., 2015. Electrical conductance and structure of copper atomic junctions in the presence of water molecules. *Phys. Chem. Chem. Phys.*, *17*(48), pp.32436-32442.
3. **Li, Y**., Kaneko, S., Komoto, Y., Fujii, S., Nishino, T. and Kiguchi, M., 2016. Atomic and Electronic Structures of a Single Oxygen Molecular Junction with Au, Ag, and Cu Electrodes. *J. Phys. Chem. C* , *120*(29), pp.16254-16258.
4. **Li, Y.**, Kaneko, S., Fujii, S., Nishino, T. and Kiguchi, M., 2017. Atomic structure of water/Au, Ag, Cu and Pt atomic junctions. *Phys. Chem. Chem. Phys.*, *19*(6), pp.4673-4677.

Conference

1. **Li, Y.** , Kaneko, S., Kiguchi, M. " Atomic and Electronic Structures of Single Oxygen Molecular Junction with Au, Ag and Cu Electrodes "*日本物理学会* 金沢 2016/9/16
2. **Li, Y.** , Kaneko, S., Kiguchi, M." Electrical conductance and structure of copper atomic junctions in the presence of water molecules "*ECOSS32*, Grenoble (France) 2016/8/29
3. **Yu Li** " Electron transport of hydrogen and water / metal junction "*日本化学会新領域ナノスケール分子デバイス「第５回若手セミナー」* 大阪 2016/3/23
4. **Li, Y.** , F. Demir, Kaneko, S., A. Saffarzadeh, Kirczenow, G. , Kiguchi, M." Atomic structure and electron transport property of copper atomic junctions in the presence of water molecules "*日本物理学会* 仙台 2016/3/20
5. **Li, Y.** , Kaneko, S., Kiguchi, M. “Electron transport of single hydrogen molecule bridging between Au, Ag and Cu electrodes” *ECOSS31*, Barcelona (Spain) 2015/9/2
6. **李渝**，金子哲，木口学 " 金、銀、銅電極を用いた水素単分子接合の電子輸送特性の解明 "*日本物理学会* 東京 2015/3/21